Maximising Achievable Rates of Experimental Nonlinear Optical Fibre Transmission Systems

Daniel John Trevor ELSON

A thesis submitted to University College London (UCL) for the degree of Doctor of Philosophy

Optical Networks Group
Department of Electronic and Electrical Engineering
University College London (UCL)

December 2018

I, Daniel John Trevor Elson confirm that the work presented in this thesis is my own. Where information has been derived from other sources, I confirm that this has been indicated.

Abstract

It is generally expected that the demand for digital data services will continue to grow, placing ever greater requirements on optical fibre networks which carry the bulk of digital data. Research to maximise achievable information rates (AIR) over fibre has led to increasing spectral efficiency, symbol rate and bandwidth use. All of these contribute to transmission impairments due to the nonlinear nature of the optical fibre. This thesis describes research performed to investigate the effects of nonlinear impairments on the AIRs of experimental optical fibre transmission.

To maximise throughput, the entire available optical bandwidth should be filled with transmission channels. An investigation into large bandwidth transmission through the use of spectrally shaped amplified spontaneous emission noise (SS-ASE) was conducted. The enhanced Gaussian noise model is used to analytically describe this technique, and SS-ASE was experimentally shown to provide a lower bound on the AIR.

Nonlinear interference (NLI) was modelled from an inter-symbol interference (ISI) model to characterise the noise and was experimentally verified. This new understanding helps quantify potential gain available from nonlinearity mitigation.

Multicore fibres offer an alternative route to improve AIR, and are susceptible to another noise source known as crosstalk. This inter-core crosstalk can be controlled by suitable design of the fibre, hence in the limiting case, NLI rather than crosstalk will limit AIR. Nonlinearity compensation was, for the first time, experimentally demonstrated in the presence of crosstalk in a homogeneous 7-core fibre and shown to provide an increase in AIR.

The results of this thesis can be used to evaluate future transmission systems for maximising information rates. It was shown that experimentally, SS-ASE is a viable transmission tool to evaluate system performance, NLI can be characterised using an ISI model and nonlinearity mitigation is possible in MCF systems limited by crosstalk.

Impact Statement

A COMMON misunderstanding is that most of the data that is provided on the internet is transmitted by satellites. But this is not the case, in reality 99% of data is transmitted over optical fibre [34]. Wireless standards such as 3G, 4G LTE and 5G give the public access to the internet straight in to their pockets, whilst on the move. These use microwaves to get the data to and from the mobile phone and a base station. But as soon as it arrives at the base station the signals are aggregated and converted into the optical domain to be sent over fibre to the rest of the network and the internet. The bandwidth requirements for each of these standards increases, putting strain not only on the microwave technology but also on the backbone fibre network.

One issue with optical fibres is that due to the Kerr nonlinearity (where the refractive index of the fibre changes with the amount of power inside it) the type and number of signals in the fibre affect the achievable transmission rates. The work in this thesis attempts to address the methods of investigating and understanding the nonlinear nature of the fibre, as the nonlinearity does indeed set a limit on the achievable transmission rates. Higher information rates would meet the demand for faster and cheaper internet access. The internet which has itself changed the world, some say for the worse, is now a ubiquitous part of modern life.

In this thesis, theoretical and experimental sides of optical fibre transmission are investigated. A theoretical model was evaluated experimentally that allows characterisation of nonlinear noise. It indicates there is correlation in the noise and so it can be mitigated, which would improve performance. Critically, this works without knowledge of the interfering channels, so has great potential to be useful in network applications.

Investigations of total achievable information rates necessitates filling the conventionally amplified bandwidth (4 THz) of the optical fibre. This requires large banks of lasers, independent modulation schemes and lots of setup time. As part of this thesis a novel bandwidth loading scheme of using spectrally shaped amplified spontaneous emission noise was proposed and investigated. A theoretical understanding of this technique is shown and is verified experimentally. This technique will allow smal-

ler research institutions and companies to test their systems for broadband scenarios without the need for expensive loading schemes.

PEOPLE ARE PEOPLE.

—Douglas Stone, *Difficult Conversations - How to Discuss What Matters Most*

Acknowledgements

"Do as I say, not as I do."

— Prof. Polina , *Bayvel*

I OWE A GREAT debt to my supervisor, PROF. POLINA BAYVEL for her guidance, influence and taking time to deal with someone who spent most of his time being a poor writer but eventually a successful editor. My first second supervisor Dr. Benn Thomsen who presented me with valuable ideas, inspiration and suggested many solutions to any problem I came to ask and to my second second supervisor Dr. Robert Killey who has been a steady source of information regardless of his official title.

I would like to acknowledge support from the Engineering and Physical Sciences Research Council (EPSRC) and an Industrial CASE award from the BBC.

Special acknowledgement is made to NICT, whom awarded an Internship Research Fellowship to the author that made part of this work possible. Thanks to Dr. Ben Puttnam for giving me the opportunity to work in Japan and suggest I submit my work at the IEEE summer topical.

Additionally I would like to thank my colleagues, many a tea break and chat have been shared, over which revelations could occur. Thank you for creating an inviting place to work and friendly environment to discuss ideas. I would particularly like to thank Dr. Lidia Galdino and Dr. Kai Shi for their time in teaching me the quirks of the lab and having the patience to deal with my mistakes.

I have huge thanks for my parents, whom have supported me throughout my academic work. Another thanks is due to my brother James 'lightweight' Elson, for motivating me to improve my fitness levels.

To my housemates; during my stay at the Cally Castle I wish to say thank you to the LAn, for being reliable, M'Brown, for live twitch streams and the long to short shaped Funnell for being perpetually busy. Definitely in my top six Castle stays.

And finally Tim 'mitxela' Jacobs whom has contributed to my personal projects, my masters work at Imperial College but also in my PhD research.

Contents

Abstract **3**

Impact Statement **4**

Acknowledgements **7**

List of Figures **10**

List of Tables **15**

1 Introduction **16**
1.1 Literature review of experimental high throughput transmission 19
1.2 Structure of the rest of this thesis 26
1.2.1 List of original contributions 27
1.3 Publications arising from the work presented in this thesis 29

2 Components of Optical Transmission Systems **31**
2.1 Communication over an optical channel 31
2.1.1 Quadrature amplitude modulation (QAM) 33
2.1.2 Mutual information 34
2.2 Optical fibre channel 36
2.2.1 The nonlinear Schrödinger equation (NLSE) 38
2.2.2 Optical amplification 39
2.3 Coherent receiver 40
2.4 Back-to-back limitations on signal-to-noise ratio 42
2.4.1 Construction of an optical transmitter 43
2.5 Pre-distortion of transmitter components 45
2.5.1 Linear pre-distortion 45
2.5.2 Volterra pre-distortion 46
2.5.3 Comparison of pre-distortion techniques 47

3 Transmission Emulation **51**
3.1 Recirculating loop 52
3.2 Gain equalisation 55
3.2.1 Experimental broadband transmission 56
3.3 Bandwidth emulation using spectrally shaped noise 61
3.3.1 Statistics of SS-ASE 62
3.3.2 Experimental generation of SS-ASE 64
3.3.3 SS-ASE modeling 66
3.3.4 Experimental evaluation of SS-ASE 68

3.3.5 Launch power investigation . . . 70
3.3.6 Distance investigation . . . 72
3.3.7 Bandwidth investigation . . . 73
3.4 1 Tb/s superchannel transmission . . . 74
3.4.1 Experimental setup . . . 75
3.4.2 Receiver digital signal processing . . . 77
3.4.3 Experimental demonstration . . . 78
3.5 Summary . . . 79

4 Mitigation of Nonlinear Interactions **81**
4.1 Characterisation of nonlinear interference (NLI) . . . 82
4.2 Experimental setup and results . . . 85
4.3 Nonlinearity mitigation in a recirculating loop . . . 89
4.4 Straight line transmission link . . . 91
4.5 Intercore-crosstalk (IC-XT) on SNR . . . 94
4.5.1 Modelling the impact of IC-XT . . . 95
4.5.2 Experimental investigation of IC-XT . . . 97
4.5.3 Nonlinearity mitigation in the presence of IC-XT . . . 99
4.5.4 Impact of crosstalk on square QAM formats . . . 103
4.6 Summary . . . 105

5 Conclusions and further work **107**
5.1 Summary of Research . . . 107
5.2 Future Work . . . 109
5.2.1 Odd-even channel correlation . . . 109
5.2.2 SS-ASE in multicore fibres . . . 109
5.2.3 DBP in the presence of a dispersion map . . . 110

References **111**

A Acronyms **125**

B Digital Signal Processing **130**
B.1 Deskew and normalisation . . . 131
B.2 Resampling . . . 131
B.3 Electronic dispersion compensation (EDC) . . . 131
B.4 Digital backpropagation (DBP) . . . 132
B.5 Constant modulus algorithm (CMA) and radially directed equaliser (RDE) . . . 134
B.6 Frequency offset removal . . . 135
B.7 Carrier phase estimation . . . 136
B.8 Gram-Schmidt orthogonalisation procedure . . . 136
B.9 Performance measurement . . . 137

List of Figures

1.1 Evolution of transmitted number of bits per two polarisation symbol, for experimental transmission systems using single core single mode fibres [5]. 20
1.2 Evolution of (a) total demonstrated capacity and (b) capacity distance product in long distance optical transmission systems based on single core single mode fibre [5]. 21
1.3 Experimental results from published papers showing spectral efficiency versus distance featuring highlighted reference in table 1.1. Unlabelled points are from [6, 14, 61, 92, 118, 145, 149, 150] 21
1.4 Cross section of a 7 core single-mode fibre with fibre diameter and intercore distance labelled. This fibre was used for transmission in [102] and section 4.5. 25

2.1 Capacity of a channel as a function of SNR for bandwidths of 1 and 2 Hz 32
2.2 Constellation diagrams for different modulation formats, containing 2, 4, 6, 8 and 10 bits of information each. Noise loaded to an SNR of 20 dB modelled as Gaussian noise on real and imaginary components. 33
2.3 Capacity of a channel as a function of SNR and for two polarisation modulation formats, the black theory line is given by Eq. 2.2. 35
2.4 Diagrammatic view of a polarisation diverse coherent receiver with balanced photodiodes. Optical paths are shown in red and electrical paths are shown in blue. 41
2.5 Optical power transmission function for a Mach-Zehnder modulator biased at $1.5V_\pi$. Red lines showing the signal applied and signal transmitted by the MZM. 43
2.6 Layout of a single polarisation Mach-Zehnder modulator and the chain of components for a dual polarisation optical transmitter 45
2.7 Experimentally obtained kernel coefficients for the signal path of the in-phase component of the X-polarization. (a) frequency response of the first order kernel, normalised coefficients for the second (b) and third (c) order kernel, with memories of 256, 8 and 3 long respectively. 48
2.8 OSA plots showing the effect of using a linear filter or Volterra filter for electronic pre-distortion in the optical domain, taken with 0.02 nm resolution 48
2.9 Histograms showing the back-to-back SNR over time for a Volterra pre-distortion and Linear pre-distortion 49

3.1 System setup for analysis of transmission OSNR impairment when using a) straightline and b) recirculating loop. Loop coupler can be 50:50 or 90:10 which changes the insertion loss and loop loss . The loop loss can be emulated with the VOA after fibre span. 53
3.2 OSNR as a function of distance for a straight line system and compared to single span loop with different coupling ratios. Dotted line showing the OSNR when limited by transceiver noise to 24 dB, with a span length 100 km. 54
3.3 Change in SNR for 90:10 loop coupler relative to 50:50 as a function of distance. For one span of 50, 80 and 100 km with total loop loss of 9.4, 15 and 18.8 dB respectively. Dotted lines showing the SNR when limited by transceiver noise to 24 dB 55
3.4 Experimental setup to investigate nonlinear distortions in wide bandwidth transmission. 57
3.5 (a) Optical spectrum taken from an OSA with resolution of 0.05 nm. (b) Filter attenuation profile defined by dynamic range (c) Generated filter uploaded on to the WSS (d) Input and output spectra compared. . 57
3.6 Optical spectrum taken from an OSA with resolution of 0.1 nm after varying the number of recirculations. The WSS being used as a GFF was optimised in every case except 32BPF. This trace shows the spectrum with the WSS set to a band pass filter at 32 recirculations. 59
3.7 Subset of data from Fig 3.6 for clarity, showing the optical spectrum taken from an OSA with resolution of 0.1 nm. 59
3.8 SNR performance of the transmission system utilising SS-ASE for different transmitted bandwidths after 1010 km of propagation, solid lines represent the predictions obtained using Eqn. 4.9 and markers correspond to experimental data. Taken from [115]. 60
3.9 Probability density functions of absolute electric field for SS-ASE, Nyquist pulse shaped PDM-16QAM and PDM-QPSK at (a) transmitter and (b) after 240 km of fibre propagation. 63
3.10 Peak to average ratio (PAR) of absolute electric field as a function of distance for: PDM-QPSK, PDM-16QAM and SS-ASE. 64
3.11 (a) Overall system setup consisting of an external cavity laser (ECL), optical comb generator (OCG), IQ modulators, polarisation multiplexer (Pol Mux). The recirculation loop uses acousto-optic modulators (AOM), variable optical attenuators (VOA). (b) Optical spectra of SS-ASE and 9 sub- channel superchannel with various guardbands. 64
3.12 Back-to-back performance for the central (Ch0) and outermost subchannels (Ch$\pm$4) of the test superchannel with SS-ASE loading. Also shown as squares is the performance of a single channel system. . . . 65

3.13 Experimental Setup, showing the SS-ASE source constructed from an ASE source, high power (HP) EDFA, variable optical attenutator (VOA) and wavelength selective switch (WSS), the digital transmitter using external cavity lasers (ECLs), polarisaton multiplexer (Pol. Mux.) and IQ modulators (IQ Mod.), and a recirculating loop using acousto-optic modulators (AOMs), polarisation scrambler (PS) and WSS for gain flattening and a band pass filter just before the coherent receiver. Inset, optical spectrum showing one channel with 240 GHz of SS-ASE. 66
3.14 Diagrammatic setup showing the optical spectra for two different interfering schemes for the channel under test (CUT). (a) 6 channels carrying modulated data and (b), spectrally shaped ASE with the same occupied bandwidth 67
3.15 a) SNR as a function of launch power for just channel interferers and 1 channel with SS-ASE taken at 2028 km. Crosses are experimental points and solid lines are the model b) Histogram of SNR of the CUT over time for channel interferers and SS-ASE for 4QAM at a fixed launch power of 1 dBm. 70
3.16 a) SNR as a function of launch power for just channel interferers and 1 channel with SS-ASE taken at 2028 km. b) Histogram of SNR of the CUT over time for channel interferers and SS-ASE for 64QAM at a fixed launch power of 1 dBm. 71
3.17 Mutual information (MI) measured as a function of distance for channel interferers and SS-ASE schemes. Markers are experimental points taken at a fixed launch power and lines are from the model. (a) channel interferers (orange) and SS-ASE (purple). (b) shows the difference in MI between channel interferers and SS-ASE as a function of distance 72
3.18 Difference in peak SNR between channel interferers and SS-ASE as a function of bandwidth for different number of channel interferers at optimum launch power. For a transceiver with a maximum SNR of 20.1 dB at 2000 km. The marker is the experimental work conducted. 74
3.19 Difference in peak SNR between channel interferers and the number of 40 GBd SS-ASE channels for different number of channel interferers at optimum launch power. For a transceiver with a maximum SNR of 20.1 dB at 2000 km. The marker is the experimental work conducted. 75
3.20 Experimental setup used in this work. Inset: spectrum for spectrally shaped ASE. 76
3.21 Experimental results: (a) BER averaged over both subchannels in back-to-back configuration before and after LDPC decoding. (b) BER performance after transmission over 400 km of Vascade EX2000 fibre with full C-band ASE loading. Note that measurements exhibiting no bit errors after LDPC decoding over 3×10^6 bits per measurement are rounded up to a BER of 10^{-5} 78

4.1 Experimental setup 85

4.2 Measured auto-correlation functions for various ISI coefficients. (a) Shows the ACFs for the diagonal ISI elements, $R_{l,xx}$, for ISI orders $l = 0, \pm 1, \pm 2, \pm 3$. (b) shows the ACFs of the four elements of the ISI matrices $\mathbf{R}_{\pm 1}$. Coloured curves correspond to experimental results, while black curves to split-step simulations. In all cases, the delta-correlated term Var $\left[V_{l,ij}^{(n)}\right] \delta(\Delta n)$ was artificially removed, as to produce a clear figure. 86
4.3 Correlation time (left column) and variance (right column) as a function of power (a,b), system length (c,d), and number of WDM channels (e,f). In all cases the CUT is at the centre. The figures show $R_{0,xx}$ (blue-dots), $R_{1,xx}$ (red triangles), $R_{2,xx}$ (yellow rectangles), and $R_{3,xx}$ (purple diamonds). Simulations are shown by dashed curves. The number of WDM channels in panels a–d is 7 (3 on each side of the CUT). The power in c–d was 2dBm, and that of e–f was 5.5 dBm. The number of 100 km spans in panels a,b,e, and f, was 20. 88
4.4 Normalised cross-correlation functions of the xx elements of the $l_{1,2} = \pm 1$ ISI matrices (a) and the $l_1 = 0$ and $l_2 = 1$ ISI matrices (b). The functions are plotted separately for combinations of the real and imaginary parts. The coefficients' real and imaginary parts are denoted by $R_{l,xx}^{\mathrm{Re}}$ and $R_{l,xx}^{\mathrm{Im}}$, respectively. 89
4.5 Experimental results showing SNR as a function of launch power for 7 channels after 11 spans 1114 km containing (a) 4QAM or (b) 64QAM. Plus markers showing the performance for all modulated channels, upward pointing triangles showing the performance with DBP, crosses showing the performance when using SS-ASE, downward pointing triangles showing the performance with SS-ASE and DBP. Lines showing the third order polynomial fitted to the data for calculating the peak SNR at optimum launch power 90
4.6 SNR (a) and gain from DBP (b) measured as a function of distance for 7 channels containing 64QAM at a fixed launch power of 1 dBm. Plus markers showing the performance for all modulated channels, upward pointing triangles showing the performance with DBP, crosses showing the performance when using SS-ASE, downward pointing triangles showing the performance with SS-ASE and DBP. 91
4.7 Setup showing straight line transmission system, inset showing received spectrum with resolution of 0.2 nm for different total launch powers. All spools are 50.6 km long leading to 101.2 km spans, where the dispersion for each spool is found in Table 4.1 92
4.8 SNR measured as a function of total launch power for C-band transmission over a straight link with and without DBP. Circular markers show SNR for 16QAM and stars are for 64QAM. 93
4.9 MI measured as a function of total launch power for C-band transmission over a straight link (1100 km) with and without DBP. Circular markers show SNR for 16QAM and stars are for 64QAM. For 64QAM transmission a total throughput of 22.01 and 22.77 Tb/s with and without DBP is achieved 94

4.10 Experimental setup showing transmitter configuration, recirculating loop using multicore fibre and receiver. A tap before the central core is used for applying power to interfering cores so that the cores have recirculated light like the core under test. 97
4.11 SNR shown as a function of launch power for a single 16QAM channel at a distance of 2148 km (40 recirculations) for different IC-XT levels 98
4.12 SNR and MI for 4QAM, 16QAM and 64QAM shown as a function of IC-XT at optimum launch power of -4 dBm for 10, 40 and 110 spans respectively 98
4.13 SNR shown as a function of launch power for a single 16QAM channel at a distance of 1880 km (35 recirculations) for the maximum and minimum IC-XT levels, with and without single channel DBP. 99
4.14 SNR shown as a function of IC-XT at 1880 km with and without DBP at a constant launch power of -2 dBm. Dashed lines showing the analytical SNR for the given IC-XT. Solid line showing the additive noise from IC-XT on a fixed SNR at minimum IC-XT 100
4.15 Measured SNR gain from DBP shown as a function of IC-XT at 1880 km at optimum launch power of -2 dBm 101
4.16 Measured gain in SNR from DBP shown as a function of IC-XT at fixed launch power of -2 dBm, for different distances 102
4.17 Measured MI gain for 16QAM shown as a function of IC-XT at fixed launch power of -2 dBm, for different distances 102
4.18 Plot of BER against distance for (a) 4QAM, (b) 16QAM and (c) 64QAM with 5 different levels of crosstalk and (d) transmission distance for a BER threshold of 0.01 as a function of IC-XT 103
4.19 Achievable transmission distance at a BER threshold of 1.5×10^{-2} as a function of crosstalk power per span for 4QAM, 16QAM and 64QAM with and without DBP 104
4.20 SNR as a function of IC-XT for 4QAM, 16QAM and 64QAM at distance of 10 spans 563 km. (a) showing a launch power of -8 dBm and (b) at -2 dBm and (c) 0 dBm. 105

B.1 Coherent receiver and subsequent DSP chain 130

List of Tables

1.1 Details of the data used in Fig. 1.3. 22

4.1 Table describing the dispersion map of the straight line link, showing each spool number in transmission order and its corresponding dispersion 92

1 Introduction

THE ADVENT of bandwidth-hungry applications — such as high-definition video and audio streaming, online real-time gaming, or peer-to-peer file sharing — in conjunction with the ubiquitous convergence of telecommunications services has steadily pushed the demand for higher transmission rate networks in all their variations. Online services provided by the likes of Amazon, Microsoft, Facebook, YouTube and twitch.tv have put strain on the internet backbone such that these companies have invested in owning part of the network in order to control the distribution of their content and services. This results in the user receiving their requested data in a timely manner [84]. In 2017, 54% of international telecommunications traffic was due to content providers and by 2024 it is projected that it will increase to 75% of a total 9,500 Tb/s [140].

The use of optical fibre as a communication channel was proposed in 1966 [56] and a theoretical limit of attenuation was presented. This set the stage for decades of research in telecommunications utilising optical fibre. The minimum viable limit of attenuation suggested in 1966 was 20 dB/km and at the time due to iron impurities in the source glass used to make the fibres. This was broken in 1970 to 17 dB/km [58] and by 1979 reached 0.2 dB/km [87]. A record for the lowest recorded attenuation was set in 2015 and is 0.1460 dB/km at $\lambda = 1550$ nm [77] but has now reached 0.1419 dB/km at $\lambda = 1560$ nm in 2018 [138]. Transmission over fibre involves electrical signals being modulated on to laser carriers, passing through the optical fibre channel, and conversion back to the electrical signals. Historically, detection was performed incoherently

with square law detection photodiodes. This method of detection results in the phase and polarisation information of the optical signal being discarded. This meant that transmission impairments, such as dispersion, had to be compensated optically [144]. The detection method also meant that only modulation formats that used the amplitude of the light like on-off keying (OOK) and pulse amplitude modulation (PAM) were viable. These formats push the throughput increase requirements on to the symbol rate and then, the associated high bandwidth transceiver components.

With the advent of the erbium doped fibre amplifier (EDFA) [81], it became possible to optically amplify the signals during transmission, rather than using power hungry repeaters. The EDFA also had the ability to amplify large bandwidths around the available laser wavelengths. A technique called wavelength division multiplexed (WDM) then increased possible capacity by using the windows to transmit multiple channels simultaneously. The wavelength windows coincided with the regions of low dispersion and low attenuation; with the improvement of manufacturing technologies and digital signal processing the transmission window of choice moved to the conventional band (1530–1565 nm) where the lowest attenuation in silica glass was found and dispersion was no longer a limiting factor.

As requirements for transmission throughput continued to increase and the limitations of WDM started to show, channels were pushed closer together into dense wavelength division multiplexing (DWDM). Simultaneously research into optical coherent detection was rekindled, enabling the detection of the received state of polarisation of the signal as well as the in-phase and quadrature components. This immediately increases the possible bits per symbol as the additional degrees of freedom allow more complex modulation formats [143]. Polarisation multiplexing took advantage of single-mode fibre's inherent possibility to use two orthogonal states of polarisation and quadrature amplitude multiplexing transmits information on the amplitude and phase of the light simultaneously. By having the information of both in-phase and quadrature components it became possible to compensate dispersion after detection. One of the other benefits, was to remove the requirement to optically mitigate dispersion [124]. The use of a local oscillator meant that there was increased frequency selectivity reducing the requirements on the filters used in detection. All of these helped to steadily increase the transmission rates to keep up with the exponential demand.

One of the advantages of coherent detection is the ability to detect higher order modulation formats like quadrature amplitude modulation (QAM). By encoding more information into each of the components of the optical signal more information can be sent, allowing throughput to increase. Some examples of higher order QAM being experimentally generated and detected in optical fibre follow, 16QAM [79], 64QAM [119], 256QAM [88], 1024QAM [64] and 4096QAM [91] corresponding to a potential 4, 6, 8, 10 and 12 bits/symbol per polarisation respectively. The maximum through-

put of experimental optical transmission systems has doubled every 18 months from 2004 to 2010 [5]. However, as each symbol gets closer together to transmit more information, these higher order modulation formats get more sensitive to noise, so long transmission distances become harder to achieve as the noise progressively builds up.

The current major problem limiting transmission rates is from the Kerr effect. This is where the refractive index of the fibre varies as a function of the instantaneous optical intensity. This is known as fibre nonlinearity [135]. The capacity for an additive white Gaussian noise (AWGN) channel is determined by the bandwidth and signal to noise ratio (SNR) [130]. The fibre nonlinearity increases leads to constructive and destructive interference of different frequencies, and so the signal frequencies can mix. This mixing can not only be within the same frequency band as the signal but outside as well, which means increasing transmission bandwidth also increases the amount of nonlinear interference. The ideal channel would respond linearly, allowing SNR to increase proportionally with signal power.

With a nonlinear channel response not only does the signal become distorted but the accompanying noise does as well. The signal and noise mix together such that the mixing becomes impossible to remove completely. Whatever the source of the noise, it is stochastic by definition and hence, the mixed noise and signal terms are stochastic as well. The nonlinear nature of the fibre means that the noise becomes signal dependent, hence the modulation format, bandwidth and input power all contribute towards noise generation. This nonlinear interference (NLI) sets a 'nonlinear limit' on capacity for the fibre optic channel [32, 83].

Optical and digital solutions to nonlinearity have been have been proposed and researched but this thesis only deals with those in the digital domain. Digital techniques to increase the SNR in the presence of the Kerr effect such as digital back propagation [55], the nonlinear Fourier transform [98] or nonlinearity aware constellation shaping [42], show potential to mitigate nonlinearity. However, the question of how these techniques perform within a practical, fully loaded optical transmission system needs to be answered as extrapolating is not reasonable [125]. The limitations of these techniques have not been fully addressed, especially in the regime where nonlinear distortions from the Kerr effect and the nonlinear interference limits the transmission system performance.

The ability to explore transmission over transoceanic distances as part of a controlled experiment is essential in understanding and maximising the throughput of experimental systems. This can be achieved using straight line systems where each fibre span and amplifier is discrete. The draw back of this system is the inherent cost and number of discrete elements that need to be controlled and maintained. A common alternative is the recirculating loop, which uses the same fibre span and amplifier multiple times to reach the same transmission distance. Extracting the best performance

from each transmission scheme is required to successfully study NLI in the laboratory.

Understanding the characteristics of the NLI being generated is essential in order to maximise potential mitigation [48]. Hence, to treat the Kerr effect as a deterministic effect NLI must not be treated as noise but as a signal dependent perturbation.

An alternative to increasing the transmission bandwidth is spatial division multiplexing (SDM). SDM technologies have been widely proposed as a cost-effective solution to increase the per fibre transmission capacity by utilising multiple cores or spatial modes [107, 121]. Single-mode multicore fibres (MCFs) offer a migration path into SDM technology in the short term. Such fibres have been shown to support high spectral efficiency modulation formats without the complexity of high order multiple input-multiple output (MIMO) based receivers [100] needed by multimode fibres. MCFs have been used in longhaul transmission, access, datacentre and networking demonstrations. The benefits of SDM over single core single-mode fibre (SMF) will be evident with integration, as efficiencies can be improved. For example a multicore EDFA has been demonstrated to be 14% more efficient than the equivalent number of single core EDFAs [136].

There are three key problems which the research presented in this thesis aims to address in the context of increasing transmission throughput: 1) investigation of how transmission systems perform over large bandwidths, in the context of fibre nonlinearity and how large bandwidth experiments can be practically realised to give insight into system design, 2) the investigation of statistics of nonlinear interference to enable effective nonlinearity mitigation and 3) another approach to increase throughput is through the use SDM. However, even with these SDM technologies, nonlinearity still impacts throughput and its impact requires further study.

1.1 Literature review of experimental high throughput transmission

Optical networking and transmission has been a research subject for more than four decades. Work has pushed the boundaries of symbol rates, modulation formats and channel bandwidths to its limits. There are various requirements for an optical transmission system; the desired outcome could be to maximise throughput at a given transmission distance or to minimise cost. Increasing symbol rates puts more emphasis on the transmitter and receiver as they need to be able to deal with the higher frequencies associated with the symbol rate. As transmission distances are increased, more noise is added to the signal, coming from the optical amplifiers compensating for the attenuation of the fibre and the nonlinear interference from the fibre's nonlinear refractive index. Higher order modulation formats require complex digital signal processing

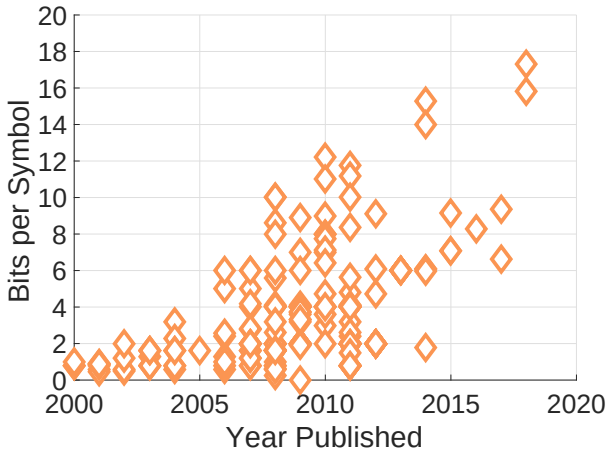

Figure 1.1: Evolution of transmitted number of bits per two polarisation symbol, for experimental transmission systems using single core single mode fibres [5].

in order to recover the denser constellations. Larger optical bandwidths push the requirements of the amplifiers as they must maintain signal powers over broader signal spectrum and this also increases the amount of nonlinear noise generation. There are many factors that need to be balanced in order to make a functional optical fibre communication system.

One method to increase throughput is to send more information during the same time slot. This can be achieved by increasing the alphabet over which information is sent. By taking the logarithm to the base 2 of the size of alphabet, the amount of information contained in each symbol can be determined in bits, see Eq. 2.1. It can be seen in Fig. 1.1, that the number of discrete symbols (size of the alphabet) has been increasing with time. This means that for a given bandwidth the amount of information being sent also increases. One of the challenges with improving throughput using higher order modulations is the increasing required SNR. As the number of symbols increases it becomes harder to distinguish between each symbol since they get closer, relative to each other. This can lead to mistakes and errors, which is not useful in terms of information and so no longer contributes to increasing throughput.

Increasing the number of bits per symbol does not encompass the whole problem. There are many factors which can influence the overall rate of transmission. The symbol rate, number of channels, spacing between the channels, amplification methods, span length, digital signal processing and the transmitter and receiver hardware. All of these will affect the received SNR and, hence, the net total information that can be sent. A useful metric to compare different systems is the total throughput, but because the system is designed to transfer information from one place to another, the transmission distance can also be another useful metric. These two metrics can be combined to make the capacity distance product. This gives a better understanding of what was actually achieved in a given experiment.

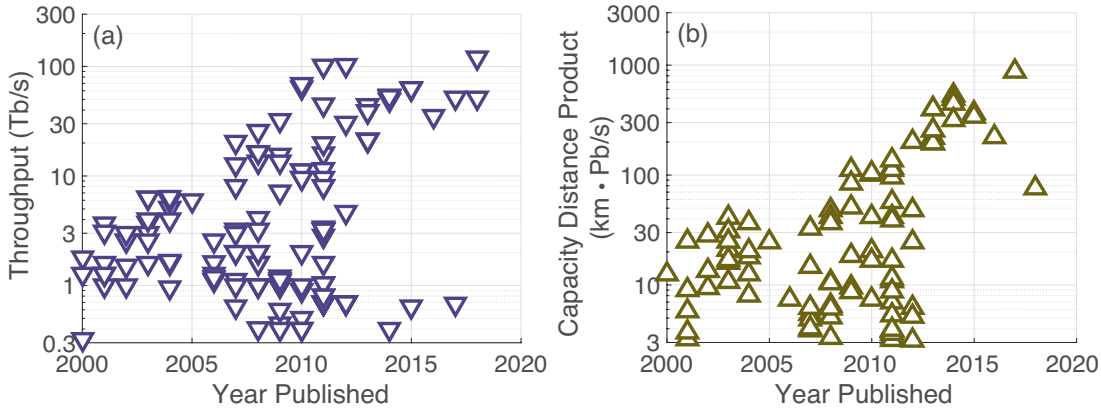

Figure 1.2: Evolution of (a) total demonstrated capacity and (b) capacity distance product in long distance optical transmission systems based on single core single mode fibre [5].

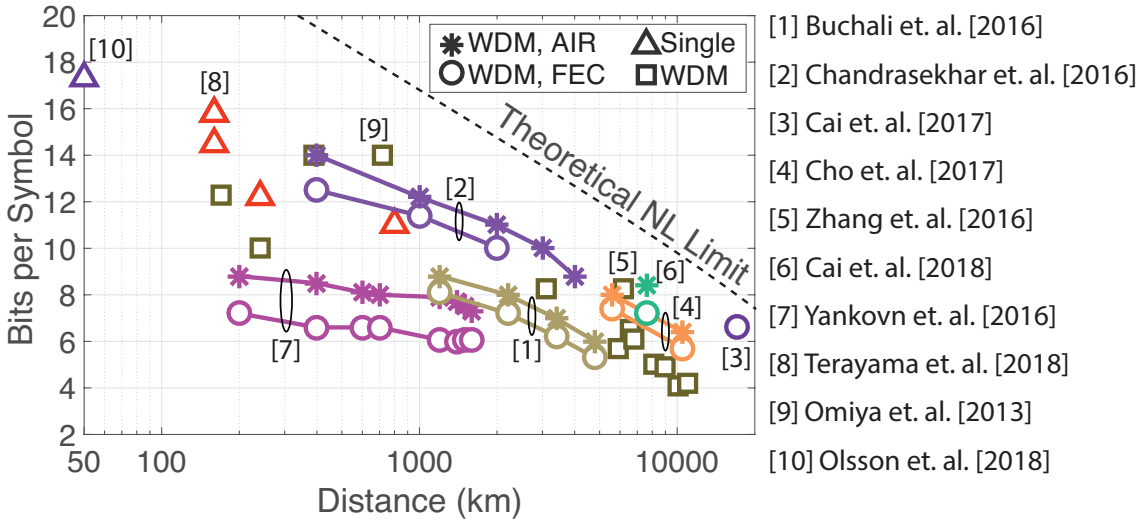

Figure 1.3: Experimental results from published papers showing spectral efficiency versus distance featuring highlighted reference in table 1.1. Unlabelled points are from [6, 14, 61, 92, 118, 145, 149, 150]

In Fig. 1.2 (a) the capacity and (b) capacity distance product is shown as a function of year published. It can be seen there is a general positive trend, that is, as time progresses the capacity increases steadily but after 2011 the rate of increase can be seen to slow down. The same is seen for the throughput distance product but the slow down in growth is not seen until 2015. The effects of fibre nonlinearity, limited bandwidth and back-to-back performance can now be seen to limit what is achievable in single core single mode fibres.

In order to explore how close current research is to reaching its limit, the number of bits per symbol as a function of distance for SMF is shown in Fig. 1.3. It can be seen, the highest spectral efficiencies for optical fibre, have been achieved by using just a single channel. These points are shown as triangles, the spectral efficiency in this case is defined by the order of modulation and the bandwidth occupied by the single chan-

Table 1.1: Details of the data used in Fig. 1.3.

No. on Fig.	Distance (km)	Bits per symbol	Reference	Author	Year
1	1200	8.8	[10]	Buchali	2016
2	400	14	[19]	Chandrasekhar	2016
3	17110	6.6	[11]	Cai	2017
4	5600	8	[20]	Cho	2017
5	6200	8.25	[149]	Zhang	2016
6	7600	8.4	[12]	Cai	2018
7	200	8.8	[147]	Yankovn	2016
8	160	15.8	[141]	Terayama	2018
9	720	14	[92]	Omiya	2013
10	50	17.3	[91]	Olsson	2018

nel. In the case of a square marker, at least 1 THz of bandwidth was occupied and so the transmission is counted as a WDM system. Here, the spectral efficiency is defined by the guardbands between each channel and the bits per symbol in each channel. The stars show WDM systems >1 THz in transmission bandwidth, as in the squares, but the actual experimental received symbols are taken into account. The metric is now the mutual information as defined in section 2.1.2, which is a measure of achievable information rate. Mutual information is used as the metric for achievable information rate throughout this thesis. This is a better metric to compare systems as it factors in experimental imperfections, since it incorporates the net effects on the symbols from all impairments and is the theoretical maximum achievable rate (excluding forward error correction (FEC)). In the case of soft decision FEC coding, the received symbols need to be processed and decoded as they contain soft information from the actual channel. The FEC decoded metric shown as circles, additionally incorporates the imperfections of the code used, and hence, represents the achieved information rate for that given system only.

The theoretical nonlinear (NL) limit is calculated from the Gaussian noise model (see Section 3.3.3) and the Shannon–Hartley theorem (see Eq. 2.2). Here, the theoretical limit is calculated assuming 50 km spans, high (>64QAM) order modulation format, amplifiers with noise figure of 3 dB and the use of single channel DBP for NLI mitigation. It is not strictly correct to compare all of these experiments to the theory as they each have different amplification and span formats. But this theoretical estimate gives an indication on the upper limits of possible achievable information rates.

To give context to the distances quoted in Fig. 1.3, there are installed fibre links that cover access points to the back-bone network less than 100 km long, back-bone fibre links spanning countries around the order of 1000 km long and submarine optical fibres that span the Atlantic ocean joining Europe to the Americas. One example is the AC-2/Yellow submarine cable owned by Level 3, which is 7001 km long [139] and runs as a direct link from Bude, Cornwwall, United Kingdom to Bellport, New York, United States at a reported 1.28 Tb/s [68] and the AEConnect cable from Killala,

Ireland to Shirley, New York is 5522 km at 13 Tb/s (130×100 Gb/s) per fibre pair [21].

Probabilistic shaping [50] reduces the spectral efficiency of a given format but due to fibre nonlinearity it can increase the received SNR and improve the overall throughput. Probabilistic shaping should be tailored to a specific channel and SNR [131] and improves the amount if MI that can be attained. The highest achieved spectral efficiency was shown in [91], where a probabilistically shaped 4096QAM superchannel consisting of 10 subcarriers modulated at 3 GBd was successfully transmitted 50 km. The number of bits per symbol shown is that which was calculated after transmission, shaping and soft decision error correction. The transmitted signals take up only 31.5 GHz of optical bandwidth and hence, do not utilise the 4+ THz bandwidth of the fibre, so this work only shows an optimistic potential capacity. To achieve the full 24 bit potential of PM-4096QAM a received SNR of 36.1 dB is required . If this result could be replicated across the C-band the potential throughput would be a record 130 Tb/s

In comparison, at over 3 times the distance (160 km), a single uniform 4096QAM at 3 GBd channel utilised a digital pilot tone within a bandwidth of 3.8 GHz, a spectral efficiency of 15.8 bits per symbol was claimed [141]. The measured bit error rate was 1.5×10^{-2} so the claimed spectral efficiency cannot be compared to any achievable information rates (AIR). The MI can be estimated from the BER for this experiment, if a hard decision coding scheme and a Gaussian channel is assumed. The MI for this experiment was estimated from the BER to be 14.7 bits/sym as described in section 2.1.2. This estimate may not be reliable as deviation from the assumed Gaussian noise channel model is expected for short transmission links.

In [92], an orthogonal frequency division multiplexing (OFDM) channel of 256QAM was transmitted over 720 km and achieved a BER of 2×10^{-3}. Here the net spectral efficiency is defined by the guard interval, training symbols and an assumed 7% hard decision-forward error correction (HD-FEC) scheme. This number of 14 bits/sym is plotted on the figure but does not take into account the achieved rate due to symbol error. With the MI estimated as described in section 2.1.2, the bits per symbol becomes 12.96 bits/sym, in line with that achieved by Chandrasekhar in [19].

Another example of probabilistic shaping and soft decision coding as a function of distance was reported in [19], where 5 probabilistically shaped 256QAM channels were transmitted. The shaped constellations were compared with uniform 256QAM. It was shown that probabilistic shaping should be tailored for a specific distance and noise profile. In this experiment the 5 channels modulated at 16 GBd were spaced at 16.2 GHz for a total bandwidth of 81 GHz, which again does not utilise the full bandwidth potential of the fibre.

In [10], one channel modulated with 64QAM at 32 GBd was probabilistically

shaped to provide an arbitrary transmission rate with a fixed FEC overhead. By applying arbitrary shaping for a fixed throughput, the achieved distance was extended by 40%. The fibre was loaded with 4 other channels modulated with 4QAM at a spacing of 500 GHz. This means that the maximum potential spectral efficiency for this experiment is very low at 0.38 bits/s/Hz. This is before taking into account the information loss from transmission or shaping, hence the marker is an optimistic estimate on capacity.

Probabilistic shaping has been implemented over multiple WDM channels but only using 125 GHz of bandwidth [147]. In this experiment 5×10 GBd channels carrying 256/1024QAM, were spaced at 25 GHz, so maximum spectral efficiency would be 4 bits/s/Hz. A soft decision-forward error correction (SD-FEC) scheme was implemented and the achieved transmission rate is shown in Fig. 1.3. It can be seen from this example that the difference between MI and AIR is large to the imperfection of the FEC. Imperfect coding is not covered in the work described in this thesis.

Notably, transmission over the full 4 THz C-band has been performed by filling the bandwidth with ASE noise to mimic a fully loaded system [20]. The channel under test was a probabilistically shaped 64QAM superchannel with 5 subcarriers at 16 GBd with transmission over 11,000 km of installed fibre. This experiment demonstrated the feasibility of probabilistic shaping for installed fibre links in the full C-band. This experiment was reported in 2017, after the publication of reference [28, 29], the work which is described in chapter 3 of this thesis and was the first to quantify the use of SS-ASE for channel emulation.

In [12], the C+L band was filled with 295 channels modulated at 32.6 GBd spaced 33 GHz apart, carrying probabilistically and geometrically shaped symbols. The shaping was optimised for maximum nonlinear performance across the 9.74 THz bandwidth. Soft decision FEC was implemented, which reduced the achievable rate from 8.4 bits/sym to a measured 7.23 bits/sym, the highest achieved information rate for this transmission distance. This was due to the dual geometric and probabilistic shaping optimisation, which pushes the AIR towards the theoretical maximum [2].

A record throughput-distance product of 881 Pb/s·km was demonstrated in [11]. The C+L band was occupied with 295 channels modulated at 32.6 GBd, carrying geometric shaped symbols. The received symbols were processed with multi stage nonlinear compensation and low density parity check (LDPC) decoding was implemented resulting in an AIR of 6.6 bits/sym after decoding. Here the rate is very close to what can be expected when most of the current research techniques are combined to make the largest possible capacity transmission.

The theoretical maximum achievable rate is plotted in Fig. 1.3. This makes the assumption that the channel is AWGN in nature, so it is expected that this is to set a theoretical upper bound. With longer distances, nonlinearities build up so the theoret-

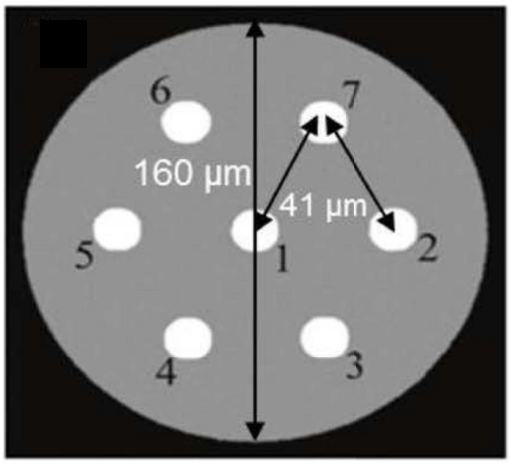

Figure 1.4: Cross section of a 7 core single-mode fibre with fibre diameter and intercore distance labelled. This fibre was used for transmission in [102] and section 4.5.

ical bound becomes less strict. A noise figure of 3 dB and launch power of 0 dBm was assumed. It is not correct to put all of the experimental points on this figure as each has its own unique set of parameters but it allows quick comparison. The total transmission length is consistent but the length of each span, the type of fibre, amplification method and signal processing techniques are different. This figure shows that at long distances the research is getting very close to reaching capacity limits of the channel.

The figures presented in this chapter are for single core single mode fibres. The work presented in chapter 4.5 uses single mode multicore fibres for which this analysis does not strictly apply. Multi core fibres (MCF) contains multiple cores, over which more information can be sent, enabling even higher throughputs. Each core can be independent or since they share the same cladding, coupling can occur, which leads to additional noise if uncompensated.

Intercore-crosstalk (IC-XT), where power from a signal in one or more fibre cores couples into another fibre core, impairs a signal that propagates in that core in a random noise-like fashion. Several theories and experiments have modelled and investigated IC-XT [18, 52, 53, 71], the most prominent being phase matching between cores. When this phase matching condition is met power can transfer between cores. MCFs with different core layout, core pitch, and cladding refractive index profiles and various strategies for reducing the crosstalk interaction and its impact have been investigated [120, 137]. IC-XT has a relatively slow stochastic time dependence (order of hours) that can change by more than 20 dB [71]. The power fluctuations of IC-XT are mainly induced by a correlation between different spectral components that can be relieved by either transmitting through fibres with large inter-core skew or using moderate to high symbol rates. However, signals that contain a strong carrier, like OOK or PAM4, maintain a level of crosstalk power variation, even for large skew and symbol rates [103].

It was observed that an IC-XT of less than -32.2 dB/100km can reduce transmission distances by up to 40% [102]. Since IC-XT can be engineered to any required level, investigating how the level of IC-XT affects the achievable rate of MCF transmission is important to experimentally quantify. The highest number of single mode cores in a single fibre was demonstrated in [122] where 37 homogeneous cores were fit into a fibre with diameter 248 μm whilst maintaining a crosstalk less than -30 dB/100km over the C+L-band. The highest transmission rate for single mode MCF was 2.15 Pb/s [100] utilising a 22 core fibre. With larger core diameters the fibre supports propagation of multiple modes. Although multimode transmission has been not studied in the work described in this thesis, it is worthy to note that 10.16 Pb/s has been achieved over 11.3 km using 6-mode 19-core fibre [132]. For comparison to Fig. 1.3, this has a spectral efficiency of 1099.9 bit/s/Hz but only 9.65 bits/s/Hz per mode per core.

Over long transmission distances in single-mode single core fibre the maximum achievable information rates are limited by nonlinear interference (NLI) noise. Well known NLI mitigation techniques include optical phase conjugation [116] and digital backpropagation (DBP) [75] at the receiver and/or transmitter [66]. DBP acts as a solution that requires changing of the digital signal processing structure inside the transmitter or receiver. This technique has been used in record breaking SMF transmission experiments and research into implementing DBP in field trials on transatlantic longhaul links are underway [20]. For MCF applications, the effects of nonlinearity on crosstalk have been investigated [73] but NLI mitigation has not been explored to date.

Future research should explore some of the methods to improve the achievable information rates within the context of the limitations stemming from the Kerr effect. The nonlinearity causes, signal dependent noise and so the capacity is affected. As has been demonstrated in the literature review as throughputs are pushed higher, by bandwidth or higher order modulation formats, the NLI starts to limit what throughputs are achievable. As the nature of the signal transmitted into the fibre affects the NLI, it is important to quantify the performance with a signal that represents the inherent characteristics of high throughput, in terms of modulation format and spectral occupancy. This scheme should enable investigations into nonlinear compensation techniques regardless of the fibre parameters. Without appropriate loading, the evaluation of NLI and throughput is not possible.

1.2 Structure of the rest of this thesis

Chapter 2 — starts with the theory of electromagnetic wave propagation in optical fibres. The nonlinear Schrödinger equation is introduced and is used as the basis for the nonlinearity mitigation technique, digital back propagation (DBP). Then in section 2.3 the use and theory of coherent receivers is explained, which are used exclusively as

the receiver of choice throughout this thesis. In the following section 2.4.1 the optical transmitter is covered in detail, from the theory of biasing Mach-Zehnder modulators and the signal processing techniques used to generate waveforms from an initial bit stream. Pre-distortion techniques used to improve SNR are studied in the case of zero transmission distance by compensating the transfer function of the transmitter.

Chapter 3 — experimental transmission emulation is studied and described. Calculations on the noise accumulation of recirculating loops are presented and the impact on performance is quantified. A broadband transmission experiment, using a straight line that utilised individual reels of fibre and separate amplifiers, is presented with the use of the nonlinear mitigation technique digital backpropagation (DBP) evaluated. Broadband transmission emulation using spectrally shaped amplified spontaneous emission noise (SS-ASE) was then thoroughly investigated. An analysis of the statistics of propagated signals was conducted, a theoretical model for the use of SS-ASE compared to modulated channels is developed and finally experimentally verified. SS-ASE was then used to demonstrate the feasibility of achieving 1 Tb/s per transceiver in a fully loaded C-band.

Chapter 4 — nonlinear interference (NLI) was subsequently studied. This was achieved by using an inter-symbol interference model and then the correlations in the NLI are experimentally confirmed. Nonlinearity mitigation is then performed in a recirculating loop and improvement in SNR and mutual information (MI) is achieved. Spatial division multiplexing (SDM) was then investigated with the use of a homogenous 7-core fibre. The intrinsic property of multicore fibres (intercore-crosstalk) was then investigated with its effects on achievable rate and nonlinearity mitigation quantified. The research presented in chapter 4.5 shows the effect of intercore-crosstalk (IC-XT) on the signal to noise ratio (SNR) in a 7 core MCF. Receiver side DBP is experimentally evaluated, together with IC-XT, launch power and transmission distance. The impact of IC-XT on NLI mitigation is investigated using a single dual polarisation 16QAM channel. To the author's knowledge, this is the first time DBP has been investigated in the presence of IC-XT. It is found that there is an SNR gain for all considered levels of IC-XT and that it acts in a similar way to additional ASE noise from transmission.

1.2.1 List of original contributions

The following is a summary of the original contributions generated in the research described in thesis.

- Implementation and characterisation of using a Volterra series transfer function to predistort for the nonlinear response of the transceiver, resulting in an increase in back-to-back SNR. This is described in section 2.5.2.

- Experimental and theoretical use of amplified spontaneous emission noise to enable experimental characterisation of broadband transmission experiments. This is described in chapter 3 and was published in [28, 29]. This technique was subsequently used for further research in [41, 62, 63, 86, 113, 115].

- Characterisation of nonlinear interference by assuming a time domain inter symbol interference model in collaboration with Tel-Aviv University. This was validated by specifically tailoring around experimental limitations to investigate the model. This is described in chapter 4 and was published in [47, 49].

The following work was conducted on secondment to the National Institute of Information and Communications Technology (NICT), a Japanese government funded research organisation.

- Nonlinearity compensation performed on a single core optical fibre link with a dispersion map. This is described in section 4.4.

- Achievable information rates were calculated for a multicore fibre as a function of intercore-crosstalk. This is described in section 4.5.2 and published at the IEEE Summer Topical Conference [30].

- For the first time, nonlinearity compensation in multicore fibres was performed in the presence of intercore-crosstalk. The benefit from compensation is quantified as a function of IC-XT; this is detailed in section 4.5.3 and was published in the proceedings at the European Conference on Optical Communications [31].

In the process of producing this thesis, Matlab code was written and utilised to automate systems and aid in the processing of data. A function was written to take received symbols and sent symbols to calculate the NLI ISI correlation coefficients as shown in Section 4.1. This returned the auto-correlation function (ACF) of the desired correlation order ready for further analysis. Two iterative SS-ASE generating scripts were written for use in experiments. The first script was used to generate up to 4 THz worth of C-band SS-ASE used in [86] and [115]. The second updates a WSS used inside the recirculating loop in order to maintain spectral flatness. Both of these SS-ASE scripts used an optical spectrum analyser (OSA) to determine the amount of power at each wavelength and design an appropriate filter. The filter update script is aware of the previously applied filter and the number of times the signal passes through the optical filter, and so the filter can be updated accordingly.

1.3 Publications arising from the work presented in this thesis

The following publications originating from the work described in this document are as follows, sorted by year.

1. Koike-Akino, Cao, Wang, Draper, Millar, Kojima, Parsons, Galdino, **Elson**, Lavery, and Bayvel, "Irregular Polar Coding for Multi-Level Modulation in Complexity-Constrained Lightwave Systems," *IEEE Journal of Lightwave Technology*, vol. 36, no. 11, (2018) [63]

2. Golani, **Elson**, Lavery, Galdino, Killey, Bayvel, and Shtaif, "Experimental characterization of the time correlation properties of nonlinear interference noise," *OSA Optics Letters*, vol. 43, no. 5, pp. 1123–1126, (2018) [49]

3. **Elson**, Puttnam, Rademacher, Luis, Sillekens, Galdino, Lavery, Awaji, Wada and Bayvel, "Nonlinearity Mitigation in the Presence of Intercore-Crosstalk," *European Conference on Optical Communications (ECOC)*, (2018) [31]

4. **Elson**, Puttnam, Rademacher, Luis, Sillekens, Galdino, Lavery, Awaji, Wada and Bayvel, "Impact of Intercore Crosstalk on Achievable Information Rates," *IEEE Photonics Society Summer Topical*, (2018) [30]

5. Saavedra, Semrau, Tan, Iqbal, **Elson**, Galdino, Harper, Killey and Bayvel, "Interchannel Stimulated Raman Scattering and its Impact in Wideband Transmission Systems," *Optical Fiber Communications Conference (OFC)*, paper Th1C.3, (2018) [114]

6. Galdino, Lavery, Liu, Balakier, Sillekens, **Elson**, Saavedra, Killey, and Bayvel, "The Trade-Off between Transceiver Capacity and Symbol Rate," *Optical Fiber Communications Conference (OFC)*, paper W1B.4, (2018) [40]

7. **Elson**, Saavedra, Shi, Semrau, Galdino, Killey, Thomsen, and Bayvel, "Investigation of bandwidth loading in optical fibre transmission using amplified spontaneous emission noise," *OSA Optics Express*, vol. 25, no. 16, pp 19529–19537, (2017) [29]

8. Saavedra, Tan, **Elson**, Galdino, Semrau, Iqbal, Phillips, Harper, Ellis, Thomsen, Killey, and Bayvel, "Experimental Analysis of Nonlinear Impairments in Fibre Optic Transmission Systems up to 7.3 THz," *Journal of Lightwave Technology*, vol. 35, no. 21, pp. 4809–4816, (2017) [115]

9. Koike-Akino, Cao, Wang, Draper, Millar, Kojima, Parsons, Galdino, **Elson**, Lavery, and Bayvel, "Irregular Polar Coding for Multi-Level Modulation in Complexity-Constrained Lightwave Systems," *European Conference on Optical Communications (ECOC)*, M.1.D (2017) [62]

10. Golani, **Elson**, Lavery, Galdino, Killey, Bayvel, and Shtaif, "Experimental characterization of the time correlation properties of nonlinear interference noise," *European Conference on Optical Communications (ECOC)*, paper W.3.E, (2017) [47]

11. Liu, Galdino, Hayes, Lavery, Karanov, **Elson**, Shi, Thomsen, Petrovich, Richardson, Poletti, Slavík, and Bayvel, "Record high capacity (6.8 Tbit/s) WDM coherent transmission in hollow-core antiresonant fiber," *Optical Fiber Communications Conference (OFC)*, paper Th5B.8, (2017) [70]

12. Saavedra, Tan, **Elson**, Galdino, Semrau, Iqbal, Phillips, Harper, Suibhne, Ellis, Lavery, Thomsen, Killey, and Bayvel , "Experimental investigation of nonlinear signal distortions in ultra-wideband transmission systems," *Optical Fiber Communications Conference (OFC)*, paper W1G.1, (2017) [113]

13. Galdino, Saavedra, Semrau, **Elson**, Tan, Iqbal, Harper, Killey, and Bayvel, "Digital Back-Propagation Performance in Wideband Optical Fibre Transmission Systems," *European Conference on Optical Communications ECOC*, paper Th.2.E, (2017) [38]

14. Millar, Galdino, Maher, Pajovic, Koike-akino, Saavedra, **Elson**, Shi, Erkılınç, Sillekens, Killey, Thomsen, Kojima, Parsons, and Bayvel , "A simplified dual-carrier DP-64QAM 1 Tb/s transceiver," *Optical Fiber Communications Conference (OFC)*, paper M3D.2, (2017) [86]

15. **Elson**, Galdino, Maher, Killey, Thomsen, and Bayvel, "High spectral density transmission emulation using amplified spontaneous emission noise," *OSA Optics Letters*, vol. 41, no. 1, pp 68–71, (2016) [28]

16. Maher, Galdino, **Elson**, Lavery, Alvarado, and Bayvel, "Algorithms and reach enhancement for ultra high bandwidth transceivers," *Optical Fiber Communications Conference (OFC)*, paper Th3A.1, (2016) [76]

2

Components of Optical Transmission Systems

OPTICAL NETWORKING systems are built from many smaller transmission systems, which are composed of 3 sections. In order they are, the transmitter, the channel and the receiver. The transmitter takes a stream of bits and converts it into the optical domain for transmission over the channel typically with the use of digital to analogue converters. The channel considered here is the silica glass optical fibre, which guides the optical signals from one place to another. The channel also includes the periodic mitigation of loss with optical amplifiers. The receiver converts the optical signals back to the electrical domain and then digitises them for processing with analogue to digital converters. After describing the optical channel and the tools to describe performance, direct detection is briefly discussed and the principle of operation of the digital coherent receiver is explained.

2.1 Communication over an optical channel

In this section, the definition of information and capacity are given, and information theoretical tools are used to measure the MI, a figure of merit (FOM) used throughout this thesis.

The amount of information that a discrete random variable X contains is quantified

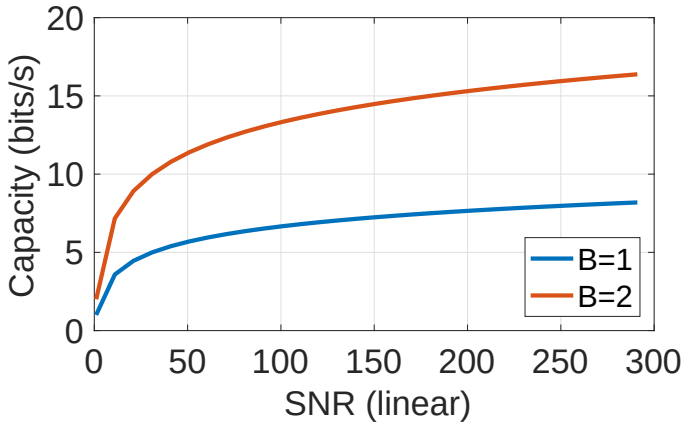

Figure 2.1: Capacity of a channel as a function of SNR for bandwidths of 1 and 2 Hz

in bits by the Shannon entropy H [51] as,

$$H(X) = -\sum_{i=1}^{m} P(x_i)\log_2 P(x_i), \tag{2.1}$$

where $P(x_i)$ is the probability of the symbol x_i appearing and m the number of possible symbols. To describe the amount of information a transmission system can transport, the channel through which the information is sent, must be considered.

The maximum reliable information rate (capacity) for a communication channel was defined in 1948 and is termed the Shannon–Hartley theorem [130]. For an AWGN channel the capacity per polarisation per core (C) in bits is given by,

$$C = B\log_2\left(1+\frac{S}{N}\right). \tag{2.2}$$

where B is bandwidth under consideration, S the average signal power and N the average noise power. This also shows how increasing the SNR increases the capacity but in the high SNR regime gives diminishing returns as the term is 'inside the log'. This is shown in Fig. 2.1.

As can been seen, doubling the bandwidth at an SNR of 31 (14.9 dB), the capacity doubles from 5 to 10 bits/s. Doubling the SNR to 62 (17.9 dB), for a bandwidth of 1, the capacity is increased to 5.96 bits/s. This is an improvement of only 0.96 bits. This equation has two main implications. When a channel has a fixed bandwidth the only way to increase the capacity is to increase the SNR. For a given SNR, the only way to increase capacity is to increase the bandwidth. Given the linear relationship between capacity and bandwidth, it means that it is beneficial to put effort into increasing and utilising larger bandwidths. With an optical fibre, the assumption that the channel is AWGN in nature, is not valid and this relationship defining capacity is no longer strict. This capacity calculated by this equation now sets an upper bound on the maximum achievable rate for the optical channel [2].

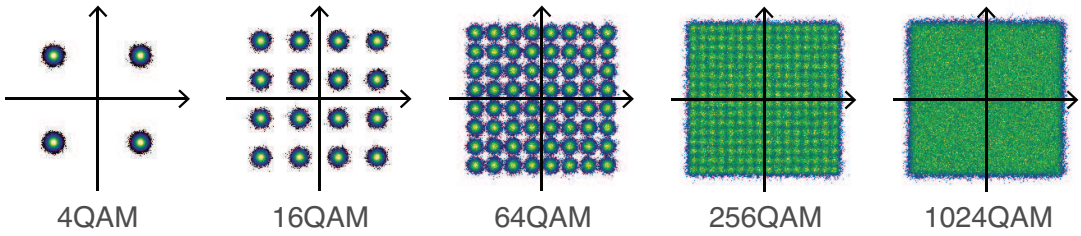

Figure 2.2: Constellation diagrams for different modulation formats, containing 2, 4, 6, 8 and 10 bits of information each. Noise loaded to an SNR of 20 dB modelled as Gaussian noise on real and imaginary components.

In an optical system it is useful to define the SNR and optical signal to noise ratio (OSNR). The OSNR is defined as the signal-to-noise ratio in the optical domain, see Eq. 3.1. This is distinct from the SNR which is the final resulting ratio after the information has been extracted from the received signal after optical to electrical conversion. The OSNR contributes towards the final SNR of a signal but is not the same. A signal could have an OSNR of 40 dB but the SNR could be 24 dB. This is the case for the optical transmitter used in this thesis. In the transmitter, the signal starts as a digital signal in the electrical domain and the SNR is set by the noise of the DACs and amplifiers used. In the receiver, the signal is further degraded by imperfect trans-impedence amplifiers (TIAs) and analogue to digital converters (ADCs). If there were no sources of electrical noise, the optical noise (OSNR) alone would set the maximum possible SNR.

2.1.1 Quadrature amplitude modulation (QAM)

The symbol alphabet of a phase-shift keyed modulation format such as quadrature phase shift keying (QPSK) is restricted to the optical phase, while quadrature amplitude modulation (QAM) formats such as 8QAM and 16QAM use distinct levels in inphase and quadrature component of the optical field to encode information.

The constellation diagram is a convenient way to represent the symbols of an optical field. This is the same as an Argand diagram that represents a complex number by plotting the real and imaginary parts on the x and y axes respectively. As the field can be represented in Cartesian space, each symbol can also be described in polar coordinates, such that every symbol has an amplitude and phase. The inphase component of a signal is shown on the constellation diagram as the x axis and the quadrature component as the y axis.

A QPSK symbol encodes 2 bits/symbol as one of four phase states with a phase difference of $\frac{\pi}{2}$ rad as depicted in the constellation diagram in Fig 2.2. 16QAM encodes 4 bits/symbol and uses 3 amplitude levels and 12 phase levels. From the cartesian representation this modulation scheme received its name, because it is modulated by 2

separate amplitude modulated carriers that are phase-shifted by $\frac{\pi}{2}$ rad, hence in quadrature. The modulation formats that contain more bits per symbol continue to separate the 2 dimensions further into smaller sections, requiring higher resolution from the transmitter.

Assuming that the optical channel is limited by additive white Gaussian noise the symbol error rate will be dominated by errors from the nearest neighbouring symbol. Therefore it is useful to map the bits to the constellation so that only one bit changes between neighbouring symbols. This bit to symbol mapping, which minimises the bit error rate given a certain symbol error rate is usually referred to as Gray coding.

As can be seen in Fig 2.2 as the number of symbols in the alphabet increases the distance between each symbol reduces. Hence for the fixed SNR (20 dB shown) symbol errors can occur leading to mistakes reducing the amount of information that can be decoded. As each polarisation is independent the inphase and quadrature of x and y polarisation can be modulated separately creating a polarisation multiplexed signal that contains twice the bits/symbol. Hence a PM-QPSK signal can carry a maximum 4 bits/symbol.

2.1.2 Mutual information

Achievable information rates indicate the number of bits per symbol that can be reliably transmitted through a channel. The channel capacity is the largest achievable information rate for which a coding scheme with vanishing error probability exists, in the limit of large block length [2]. SNR can be converted into an achievable rate by assuming a Gaussian channel and modulations format. By assuming a memoryless AWGN channel for each polarisation, the received symbols are $y[n] = x[n] + z[n]$, where $x[n]$ are the sent symbols, $z[n]$ is an independent and identically distributed zero-mean Gaussian random variable with (total) variance σ_z^2. This variance can be estimated based on the transmitted and received symbols (across both polarisations) as $\sigma_z^2 = \mathbb{E}\left[|\underline{z}|^2\right] = \mathbb{E}\left[|\underline{y} - \underline{x}|^2\right]$. The received SNR,

$$\mathrm{SNR}_{rec} = \frac{\mathbb{E}\left[|\underline{x}|^2\right]}{\sigma_z^2}, \tag{2.3}$$

where $\mathbb{E}\left[|\underline{x}|^2\right]$ is the average received symbol energy. This is a useful figure of merit for comparing optical systems to each other as it is defined independently of modulation format, symbol rate and transceiver setup.

Mutual information (MI) is an achievable information rate [3], and MI is a measure of how related two independent variables are. This is related to the amount of information that is contained in a received signal compared to a transmitted signal. The amount of information carried by a signal is set by the symbols being sent, that is the Shannon

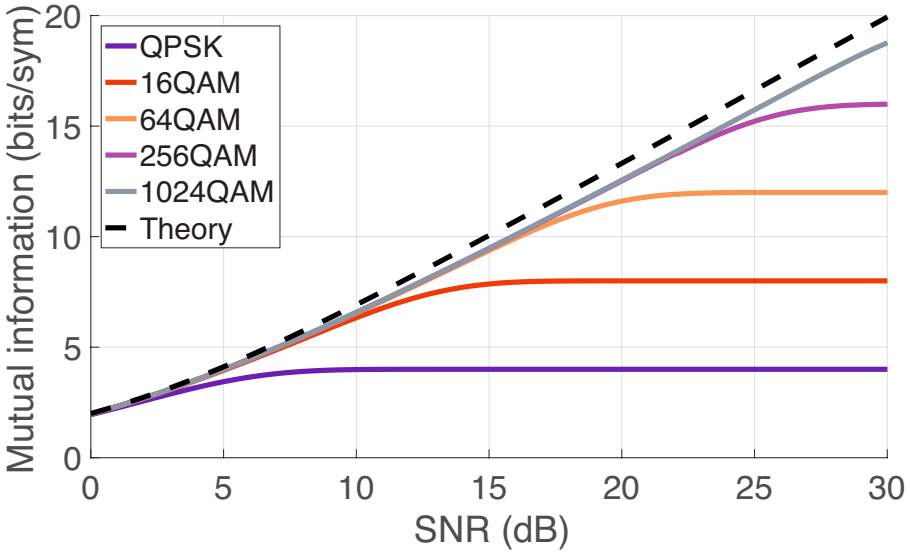

Figure 2.3: Capacity of a channel as a function of SNR and for two polarisation modulation formats, the black theory line is given by Eq. 2.2.

entropy, see Eq. 2.1. Fig. 2.3 shows Eqn.s 2.1 & 2.6, where the MI for different QAM formats are shown as a function of SNR. MI is defined mathematically as [3],

$$\begin{aligned} \mathrm{MI} &\triangleq \mathbb{E}\left[\log_2 \frac{P(X,Y)}{P(X)P(Y)}\right] \\ &= \frac{1}{m}\sum_{x\in\mathbb{X}}\int_{\mathbb{C}} P(y|x)\log_2\frac{P(y|x)}{P(y)}dy, \end{aligned} \tag{2.4}$$

where $\mathbb{X} = \{x_1, x_2, ..., x_m\}$ is the set of possible transmitted symbols and m the number of possible transmitted symbols, $P(x)$ the probability that an element of $\mathbb{X}$ is sent and $P(y)$ the probability that an element y of Y being received. The conditional probability $P(y|x)$, with the assumption of the AWGN channel, is the channel law and is given by:

$$P(y|x) = \frac{1}{\pi\sigma_z^2}\exp\left(-\frac{|y-x|^2}{\sigma_z^2}\right), \tag{2.5}$$

where σ_z^2 is the noise variance.

Using Eq. 2.5 in Eq. 2.4, the MI can be approximated using the following Monte-Carlo estimate [4],

$$\mathrm{MI} \approx q - \frac{1}{mN_s}\sum_{i=1}^{m}\sum_{n=1}^{N_s}\log_2\sum_{j=1}^{m}\exp\left(-\frac{|y-x|^2 + 2\,\mathrm{Re}\{(x_i-x_j)^* z[n]\}}{\sigma_z^2}\right), \tag{2.6}$$

where $\mathrm{Re}\{\cdot\}$ denotes the real part, $q = \log_2(m)$ is the number of bits per constellation symbol, and N_s is the number of transmitted symbols. Using Eq 2.6 it is possible to calculate the expected MI as a function of SNR for different modulation formats

and this is shown in Fig. 2.3. The MI curves shown never intersect and therefore, the largest constellation size will always provide the greatest achievable information rate for any given SNR [76]. This also demonstrates how square QAM is not matched to the AWGN as this has an offset from the theoretical capacity given by Eq. 2.2. For the case of an SNR of 24 dB the maximum MI for square QAM is 15.1 bits/sym, but for a constellation tailored to the AWGN channel, an MI of 15.96 bits/sym is possible. Throughout the work described in this thesis uniform square QAM is used exclusively and no consideration for any probabilistically shaped or geometrically shaped constellations is taken, apart from those mentioned in the literature review (chapter 1.1).

Spectral efficiency is defined as the number of bits per second, per unit bandwidth and has units of bits/s/Hz. Hence defining this for a system takes into account the bandwidth utilised so having a spacing between channels reduces the spectral efficiency. If a signal is filtered to take up less bandwidth then the spectral efficiency can be improved. This can result in a closer channel spacing, which fits more channels into the same bandwidth, improving the spectral efficiency.

The throughput of a system is given in bits/s, so to convert MI into a throughput, MI is multiplied by the symbol rate. The throughput calculated this way is an upper bound on the system throughput as this does not take into account the coding scheme. The coding scheme allows errors to be detected and correct errors. The coding scheme can also be imperfect and have its own implementation penalty and not achieve the MI calculated using Eq. 2.6. Net throughput is calculated after error correction and decoding so includes the impact of coding scheme. MI is used through this thesis because it is independent of the coding scheme and so the channel can be compared, rather than the coding scheme.

2.2 Optical fibre channel

In this section a description of the optical channel and the equations which govern the propagation of electromagnetic waves in an optical fibre are given. The impairments the signal receives are both linear and nonlinear. These can be described separately as different operations on the propagating electric field.

The propagation of electromagnetic waves is described by Maxwell's equations. These can be combined into the wave equation, hence solving the wave equation using appropriate boundary conditions will give a description of the waves' behaviour inside a fibre channel. The fibre is a dispersive medium with cylindrical symmetry, where its refractive index is a function of power. Light is confined into the fibre by the difference in refractive index between core and cladding. This is achieved by doping the glass during production to achieve the desired refractive index profile. In this thesis only fibres with a step index between core and cladding are considered.

The first phenomena to describe is due to fibre attenuation, which corresponds to,

$$\frac{\partial A(z,t)}{\partial z} = -\frac{\alpha}{2}A(z,t), \tag{2.7}$$

where α the absorption coefficient, z the position in the fibre and $t = t_0 - \beta_2 z$, which is the retarded time. This equation describes an electric field that is exponentially decaying with distance. Attenuation is measured in dB/km where a typical value for standard single mode fibre is 0.2 dB/km.

Different wavelengths travel through the fibre with different velocities which leads to chromatic dispersion. The equation which describes only this effect is,

$$\frac{\partial A(z,t)}{\partial z} = -\frac{i\beta_2}{2}\frac{\partial^2 A(z,t)}{\partial t^2}. \tag{2.8}$$

The second order dispersion parameter β_2 is derived from a Taylor expansion about the carrier frequency and is related to the dispersion parameter D expressed in units $(ps/(nm \cdot km))$ by,

$$D = -\frac{2\pi c}{\lambda^2}\beta_2, \tag{2.9}$$

where c is the speed of light. This parameter is measurable and is the sum of the dispersion from the fibre composition and the dispersion from confinement inside a waveguide. This can be engineered for desired purposes, but for standard single mode fibre is of the order 17 ps/(nm·km). Over large bandwidths the slope of the dispersion S becomes important and is given by,

$$S = \frac{dD}{d\lambda} = \frac{2\pi c}{\lambda^2}^2 \beta_3 + \frac{4\pi c}{\lambda^3}\beta_2^2, \tag{2.10}$$

where β_3 is the third order dispersion parameter coming from the same Taylor series expansion as β_2. This dispersion slope means different wavelengths have different dispersions so optical pulses from different channels are broadened by different amounts. This broadening needs to be compensated at the end of the channel especially with transmission over long distances as the dispersion accumulates. The overall accumulated chromatic dispersion from propagation can also be compensated digitally with electronic dispersion compensation (EDC) either at the transmitter or at the receiver [60, 124]. A more detailed discussion of EDC is presented in Appendix B.

Overall, the equation that describes the linear propagation through the fibre channel is then,

$$\frac{\partial A(z,t)}{\partial z} + \frac{i\beta_2}{2}\frac{\partial^2 A(z,t)}{\partial t^2} + \frac{\alpha}{2}A(z,t) = 0. \tag{2.11}$$

To contain the light and act as a waveguide, the fibre has a higher refractive index n_0 in its core than the surrounding cladding; this sets the boundary conditions. Due to

the cylindrical symmetry of optical fibres the wave equation is solved with specific solutions called modes [1]. These satisfy the symmetry and boundary conditions. In this work only single mode solutions are considered.

2.2.1 The nonlinear Schrödinger equation (NLSE)

The optical fibre channel is fundamentally nonlinear. That is n_{eff} the effective refractive index is $n_{\text{eff}} = n_0 + n_2 I$, where n_2 is the nonlinear refractive index or Kerr coefficient and I the optical intensity. The nonlinearity enters the equations from the assumption made at the electron level: the restoring force of an electron being pulled from its atom is proportional to its displacement. Once the displacement becomes too large the restoring force is no longer proportional, leading to a nonlinear response. This change in refractive index leads to a phase shift in the propagating electric field.

The nonlinear Schrödinger equation (NLSE), which describes the overall propagation in an optical fibre is,

$$\frac{\partial A(z,t)}{\partial z} + \frac{i\beta_2}{2}\frac{\partial^2 A(z,t)}{\partial t^2} = -\frac{\alpha}{2}A(z,t) + i\gamma|A(z,t)|^2 A(z,t). \tag{2.12}$$

Absorption is a function of wavelength λ, where λ_0 is the carrier wavelength. The wavelength dependence of attenuation is small over the commonly used bandwidths. The fundamental limit on attenuation is defined by Rayleigh scattering and infrared absorption [1]. Previously, so called water (OH) absorption peaks occurred but modern fibre production techniques have removed these [117].

The nonlinear coefficient γ used in Eq. 2.12 describes how the refractive index (n_{eff}) is a function of electric field intensity and has units 1/(W·km). This comes from the Kerr effect, and hence, the generation of noise as a function of power can be described. The nonlinear coefficient γ for a fibre depends on its physical parameters that is,

$$\gamma = \frac{2\pi n_2}{\lambda_0 A_{\text{eff}}}. \tag{2.13}$$

The n_2 of a fibre is material dependent, the A_{eff} the effective mode area of the propagating light and is a property that is controllable during manufacture. For special fibres such as large effective area fibre (LEAF) or quasi-single mode (QSM) fibre the area is made larger so that the γ is lower leading to better performance at high input powers. But if the area of the core gets too large then the fibre is capable of supporting more transmission modes which if not dealt with can lead to inter-modal interference [117]. The values of α, D, S and γ vary from each fibre so the resultant SNR and hence capacity can change for each fibre.

The NLSE can be solved using the split step Fourier method. This is where the evolution is treated as 2 separate operators: the linear section and nonlinear section. The

linear section stems from dispersion which is implemented as a filter in the frequency domain (see Appendix. B.3) and the nonlinear section is a power dependent phase shift in the time domain. For each step along the fibre, half the dispersion is applied, then the nonlinear operator and finally the dispersion for the second half. Each step requires 2 Fourier transforms to switch between the time and frequency domains to apply the corresponding operator. This technique is useful in simulating transmission systems to check theoretical models, corroborate experimental results or as a form of nonlinear compensation see Appendix B.4.

The nonlinear nature of the fibre leads to interference which can distort signals. The intensity dependence of the refractive index results in a signal-dependent nonlinear phase shift. Hence, the resulting nonlinear phase shift from the channel of interest from itself is termed self phase modulation. The Kerr effect also leads to other nonlinear phenomena termed four wave mixing (FWM) and cross-phase modulation (XPM) [133]. The effects of FWM in the context of this thesis is negligible compared to XPM but is important in the case of operation at low dispersion wavelengths. XPM occurs when multiple optical channels are transmitted simultaneously through the optical fibre and is present in WDM transmission. In WDM systems, the total nonlinear phase shift for the channel of interest not only depends on the optical intensity of the propagating channel of interest but also on the intensity of the signals co-propagating at other frequencies.

2.2.2 Optical amplification

The ASE-noise introduced by EDFAs is the ultimate limiting factor in optical transmission systems requiring amplification. It is necessary to compensate the fibre loss by using optical amplifiers to prevent the signal from becoming too weak to be detected. An erbium doped fibre is excited so that higher-energy states become more populated than the lower-energy state, termed population inversion. Incoming photons can cause the excited ions to return to a lower-energy state, transferring their energy to the optical domain in the form of photons with the identical phase and polarisation to the incident photons, through the process of stimulated emission. Hence, a signal input into a erbium doped fibre with a population inversion experiences amplification. Erbium ions in the excited energy state can also release their energy to the optical domain spontaneously, where the photons will have random frequency, phase, polarisation and direction. Some of these spontaneously emitted photons can travel in the doped fibre along with the signal and can interact with other excited erbium ions and hence can be amplified via stimulated emission in the same manner as the original signal [43]. Since the amplified spontaneous emission has random frequency and phase, total noise power is increased and hence, the OSNR is reduced during amplification. The ASE

noise can be modelled as an independent and identically distributed Gaussian random process. The amount of noise power generated by an EDFA (P_{ASE} in W) is governed by the following equations [1],

$$P_{\mathrm{ASE}} = 2n_{sp}(G-1)hF_cF_{bw}, \tag{2.14}$$

$$n_{sp} = \frac{N_f G}{2(G-1)} \approx \frac{N_f}{2}, \tag{2.15}$$

where, the 2 comes from the dual polarisation ASE, n_{sp} is the spontaneous emission factor, G is the gain of the amplifier, h is Plank's constant, F_c is the carrier frequency, F_{bw} the reference bandwidth being considered in Hz and N_f the noise figure of the EDFA. The term hF_c describes the average photon energy. When the gain is higher than 16 dB it can be seen that the approximation becomes valid [128].

The ASE noise is unpolarised, that is there is equal power in both polarisations and it affects both the in-phase (I) and quadrature (Q) components of the optical signal in both polarisations, the same way. Therefore, the tolerance of a given modulation format to ASE noise can be measured based on the closest Euclidean distance between the symbols, because it appears as a symmetrical spreading of the symbols on a constellation diagram.

2.3 Coherent receiver

An optical receiver has 2 distinct sections, when the signal is in the optical domain and when in the electrical domain. The conversion of the signal from optical to electrical happens inside photodiodes. The output of the photodiodes are analogue, and so, must be sampled with an ADC to obtain a digital signal. Once in the digital domain the signals can be processed and imperfections can be removed. After this, decisions are made on what symbols were sent, then checked to see if there are any errors, which in a real transmission system are detected and corrected. At this stage the required FOM can be calculated. Please see Appendix B for details of the DSP used in this thesis.

In order to recover phase and polarisation information, the received optical signal is coherently combined with a local oscillator (LO), this is called coherent detection. This allows the detection of phase and polarisation for useful information transmission. Use of coherent receivers allows high frequency selectivity, higher sensitivity and polarisation diversity. For spectrally efficient transmission formats such as DP-16QAM, a coherent receiver is the only option as it enables the full electrical field information to be captured in the receiver. This is done by mixing the received optical with a local continuous optical field whose frequency is close to that of the received signal. The layout of a polarisation diverse coherent optical receiver is given in Fig. 2.4.

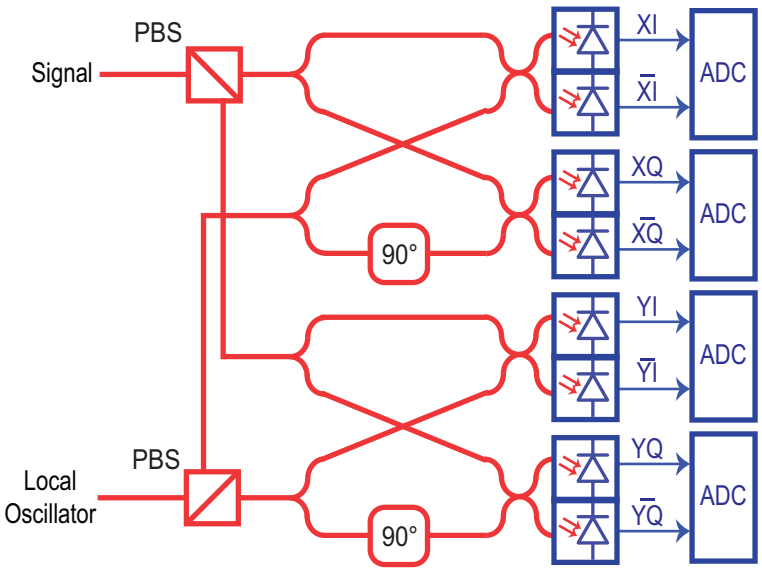

Figure 2.4: Diagrammatic view of a polarisation diverse coherent receiver with balanced photodiodes. Optical paths are shown in red and electrical paths are shown in blue.

Here, the input signal is put into a polarisation beam splitter (PBS) where the vertical and horizontal (X and Y) polarisation components are split apart from each other. Each polarisation component is then split further with a 3 dB coupler. The LO is separated in the same manner, that is, the LO is split into X and Y components and again each component is split with a 3 dB coupler. Splitting of the LO is done by aligning the single polarisation laser light to the PBS at 45° such that equal power is emitted in X and Y. The LO and signal each now have 4 components, two X and two Y. A phase shift of 90° is then applied to one X and one Y component of the LO. The corresponding X and Y components of the signal and LO are combined in 3 dB couplers and then incident on photodetectors. These mixed fields result in a beat product. The mixing is done using a component called a 90° optical hybrid [57], which is the combination of 4 couplers and a 90° phase shift. The result of this technique means the signal is mixed with the four quadrature states associated with the LO in complex field space.

The resulting electric field at each of the photodetectors can be described mathematically by letting the LO (E_{LO}) be represented as,

$$E_{LO} = A_{LO} e^{-i(\omega_{LO} t + \phi_{LO})}, \tag{2.16}$$

where A_{LO}, ω_{LO} , and ϕ_{LO} are the amplitude, frequency and phase of the local oscillator respectively. As each photodiode only detects power (the square of electric field) the received powers can be written as,

$$P_{I+} = |E_{LO}|^2 + |E_S|^2 + 2\,\mathrm{Re}[E_s E_{LO}^* e^{(i(\omega_s - \omega_{LO})t)}] \tag{2.17}$$

$$P_{I-} = |E_{LO}|^2 + |E_S|^2 - 2\,\mathrm{Re}[E_s E_{LO}^* e^{(i(\omega_s - \omega_{LO})t)}] \tag{2.18}$$

$$P_{Q+} = |E_{LO}|^2 + |E_S|^2 + 2\,\mathrm{Im}[E_s E_{LO}^* e^{(i(\omega_s - \omega_{LO})t)}] \tag{2.19}$$

$$P_{Q-} = |E_{LO}|^2 + |E_S|^2 - 2\,\mathrm{Im}[E_s E_{LO}^* e^{(i(\omega_s - \omega_{LO})t)}]. \tag{2.20}$$

As can be seen from Eqs. 2.17 – 2.20 the powers at each photodiode are mixed with each possible combination of real (I) or imaginary (Q), positively or negatively. These mixed signals are then differentially combined leading to a cancelling of the squared terms, leaving the received terms to be just the I or Q the original signal. These equations are just for one polarisation, so in a polarisation diverse receiver, which separates each polarisation into independent paths, the equations can be used to represent either polarisation.

One of the main advantages of using coherent detection with respect to narrow spaced channel transmission is the frequency selectivity. The bandwidth of a transmitted signal is typically limited by the amplifying technology, so in the case of the C-band this from 1530 – 1565 nm. The coherent receiver down converts the signal of interest from its carrier frequency (around 193 THz) to a baseband signal which can then be more easily filtered by the receiver.

The coherent receiver is used throughout the work described in this thesis for its ability to detect the relative phase of the incoming signal. The subsequent chapters use this information to receive high order modulation formats and correct for accumulated propagation impairments.

2.4 Back-to-back limitations on signal-to-noise ratio

The fundamental limit on the maximum reliable information rate was discussed in the previous chapter. In optical fibre transmission systems the noise associated with the generation process of an optical signal sets a practical limit on the maximum information rate. The upper limit on the achievable SNR in a coherent optical transmission system, that is in the absence of the fibre channel, is bounded by the transceiver subsystems. It was demonstrated that the upper limit on the throughput of any optical transmission system is ultimately limited by the finite SNR of the digital coherent transceiver subsystems [76]. In particular, the modulation format and code scheme of a practical optical system must be simultaneously optimised to match the specific SNR achieved after optical signal generation and digital coherent detection [76]. In this chapter the details of the construction of a transmitter and a nonlinear compensation technique to reduce the amount of noise at the transmitter is investigated.

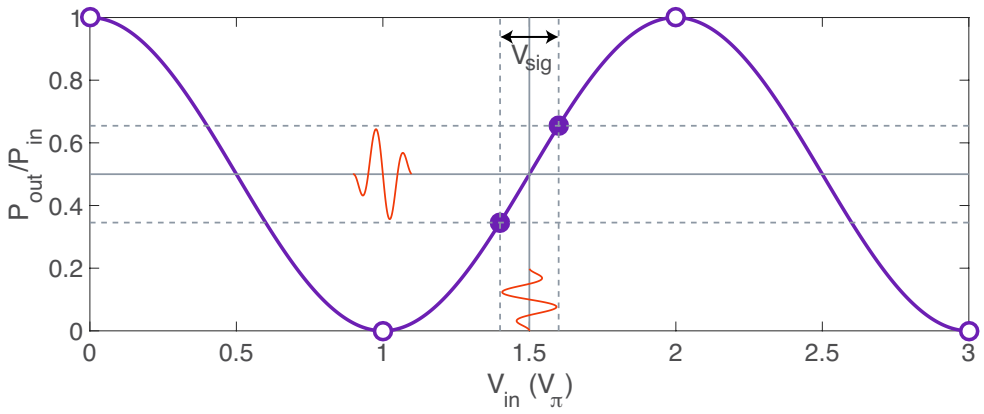

Figure 2.5: Optical power transmission function for a Mach-Zehnder modulator biased at $1.5V_\pi$. Red lines showing the signal applied and signal transmitted by the MZM.

2.4.1 Construction of an optical transmitter

The optical transmitter is a means to convert digital data into an analogue optical signal for transmission along the channel. The information starts as a signal in the electrical domain, whilst the optical signal starts as a single wavelength optical carrier upon which the information is encoded by the modulator.

Reconfigurable multipurpose transmitters start with a digital to analogue converter (DAC) from which independent RF signals are sent over cables to optical modulators. For low symbol rates with low oversampling, low pass filters are required to remove aliasing artefacts from causing in band interference in the optical domain [75]. These signals are passed to electrical amplifiers to increase the voltage swing before being put in to Mach-Zehnder modulators (MZM)s but may require attenuators to not run the amplifiers in saturation. These MZMs work by changing their refractive index with respect to the applied electrical field, this changes the relative phase of the optical wave, results in destructive or constructive interference. At MZM output, the expression for the optical power is,

$$P_{out} = P_{in}\cos^2\left(\frac{\pi}{2V_\pi}[V_{bias} + V_{in}]\right), \tag{2.21}$$

where P_{in} is optical power input to the MZM, V_π being the half wave voltage (voltage required for a π phase shift), V_{bias} the electrical direct current (DC) voltage applied to the MZM input and V_{in} the alternating current (AC) voltage of the input signal. It is an important point to note that the peak-to-peak voltage of V_{sig} affects the amount of transmission. A peak-to-peak voltage of V_π resulting in the best extinction rate as both the full transmission point and null transmission point are used but at the expense of a nonlinear response.

As can be seen in Fig. 2.5 where Eq. 2.21 is plotted for $V_{\text{in}} = 0.2V_\pi$ and $V_{\text{bias}} = 1.5V_\pi$, the exact peak-to-peak voltage and bias voltage determines the power response. At a bias voltage of V_π transmission is at a minimum due to destructive interference.

The optimal DC biasing voltage is known to be V_{bias} =1.5V_π, corresponding to the most linear zone of MZM transfer function. At this optimum bias and a signal with a peak-to-peak voltage of $0.2V_\pi$ the difference in output power variation is only 0.309 of the maximum possible. If the bias is shifted the power variation changes and the response becomes asymmetric.

A generalised transmitter is shown in Fig. 2.6. Fig. 2.6 a) shows the optical paths of a single polarisation inphase and quadrature (IQ) modulator consisting of a nested MZM structure. Fig. 2.6 b) shows a general digital signal processing (DSP) chain converting from bits to symbols to an analogue waveform at the driver amplifier (DA), the subsequent radio frequency (RF) and optical paths. The complete DSP description is given in Appendix B. IX and QX are the I and Q signals of the waveforms for the X polarisation. The optical path starts from a single laser, goes through the dual polarisation MZM and then is amplified ready for the transmission.

From Fig. 2.6, the single IQ-modulator can be seen to use two nested MZMs and a single phase shift on one of the optical paths to generate a complex waveform from the input laser source. $\varphi_{\text{I}}, \varphi_{\text{Q}}$ and φ_{P} are the DC biases for the I, Q and phase sections of the modulator respectively. Firstly, the laser is split into two paths and incident on the MZMs. This creates two independent amplitude modulated optical signals with the response described by Eq. 2.21. Secondly, one signal is then phase shifted by 90° relative to the other and recombined. The result is an optical waveform with single polarisation optical signal with independent data on the amplitude and phase of the wave. To generate a dual polarisation signal, the input laser is split into two with a polarisation beam splitter. Each polarisation component is then modulated with a single polarisation modulator and recombined, hence a dual polarisation modulator requires 6 bias voltages and 4 data inputs.

The bias point changes as a function of wavelength and temperature so needs to be monitored to produce the best signal. Biasing can be performed manually or automatically.

In this thesis electronic signals are generated from reconfigurable DACs. This allows the generated waveforms to be processed offline and optimised before transmission. The waveforms sent to the DACs can also be quickly rewritten allowing changing of modulation format, symbol rate or any other desired parameter.

A popular technique to implement is root raised cosine (RRC) filtering. Since rectangular pulses have a very broad frequency spectrum, it is desirable to truncate the transmitted pulses using the RRC filtering [99] to reduce the bandwidth of the modulated signal. The digital signals are first filtered using RRC pulse shaping at the transmitter with an impulse response with the desired rolloff. At the receiving end of the transmission link, the incoming signals are filtered by another RRC pulse shaping function which acts as a matched filter for optimum performance. The product of the

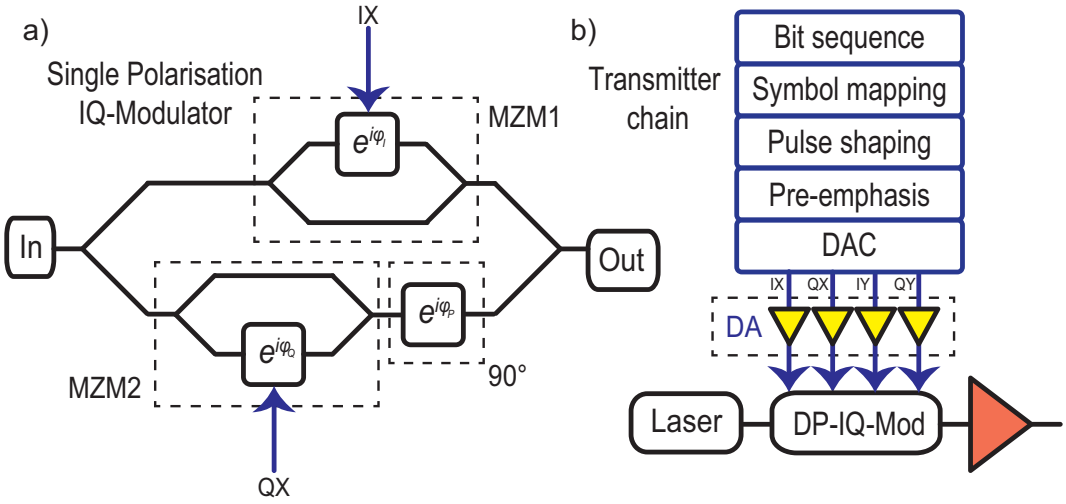

Figure 2.6: Layout of a single polarisation Mach-Zehnder modulator and the chain of components for a dual polarisation optical transmitter

two filter responses lead to an overall raised-cosine response having low inter-symbol interference (ISI), maximising the received SNR [74], coming from the orthogonality in time of sinc pluses.

2.5 Pre-distortion of transmitter components

To achieve the best possible information rates from a transceiver subsystem predictable waveforms are required. This supports digital pre-compensation of optical impairments such as fibre nonlinearity [66] and dispersion which can improve the resulting SNR. In these cases a well known waveform needs to be launched into the fibre. Each electrical component has a frequency response and phase response including the cables between them. All of these add up to create an imperfect transmission line each step affecting the resultant SNR.

The performance of nonlinear pre-distortion is affected by transmitter components. The idea for using a Volterra series for compensating a nonlinear system is not new [67] and has been used in the context of optical communications [7, 59]. The following section's novelty is limited to quantifying the performance improvement for the experimental system used for the subsequent research in this thesis.

2.5.1 Linear pre-distortion

A simple method to compensate for the frequency roll off of components in the transmitter is to measure its transfer function, calculate an inverse transfer function, then apply this filter to each waveform before being uploaded to the DAC. In principle, this allows for pulse-shaping, skew compensation and linear pre-distortion jointly for

all transceiver components with only a single linear filter. The transfer function of a general linear system is given by,

$$H(z) = \frac{X(z)}{Y(z)}, \tag{2.22}$$

where $X(z)$ and $Y(z)$ are the z-transforms (discrete Laplace transforms) of the input and output signals $x(n)$ and $y(n)$.

By assuming the system is linear the transfer function can be inverted such that for a desired output the input can be calculated. This inverse transfer function can be calculated by dividing the output by the input as follows,

$$H^{-1}(z) = \frac{Y(z)}{X(z)}. \tag{2.23}$$

The pre-distorted signal that needs to be input to the linear system for the desired output is then,

$$X_{pre}(z) = H^{-1}(z)Y(z), \tag{2.24}$$

For the signals considered here that are discrete and periodic in nature, the discrete Laplace transform can be replaced with a discrete Fourier transform. $X_{pre}(z)$ now becomes,

$$X_{pre}(\omega, n) = H^{-1}(\omega, n)Y(\omega, n). \tag{2.25}$$

To calculate the pre-distortion the frequency response of the transceiver must be calculated. For the transfer function to be calculated, a swept sine signal is sent to the DACs over the desired frequency spectrum. The received and transmitted signals are then Fourier transformed, the ratio and hence the inverse transfer function is then found. This is then transformed back into the time domain and saved as a 2^{15} tap long finite impulse response (FIR) filter. This filter is then applied to the signal before it is pushed to the DACs. This, in the ideal case, linearises the transmitter and receiver response.

The weakness with this method is in the assumption that the system is linear. In this case this technique will fail to capture the effects of the inherently nonlinear MZM transfer function of the transmitter and DA (see Fig. 2.5) . This case is termed linear pre-distortion and will be compared to a nonlinear pre-distortion described in the next subsection.

2.5.2 Volterra pre-distortion

To perform the nonlinear pre-distortion offline, the transfer function H is modelled as a truncated, time-invariant Volterra series representing the combined DAC, DA and MZM system. The relation between the received samples $y[n]$ and transmitted signal

samples $x[n]$ with Volterra operators of Pth order $H_p\{\cdot\}$ are given by,

$$y[n] = h_0 + \sum_{p=1}^{P} H_p\{x[n]\}, \tag{2.26}$$

where,

$$H_p\{y[n]\} = \sum_{k_1=0}^{m_p-1} \dots \sum_{k_p=k_{p-1}}^{m_p-1} h_p[k_1,\dots,k_p] \cdot \prod_{i=1}^{p} x[n-k_i-\tau_p], \tag{2.27}$$

The Volterra series is fully determined by the kernels h_p with memory lengths m_p, where the subscript p denotes the order of the kernel. The order dependent delay τ_p is used to align the higher order kernels centric to the first order kernel. As the kernels contribute linearly to the output $y[n]$, this property is used to determine the kernels of H from an input/output measurement by applying a least-squares fit [65], [90]. For the DAC, DA and ADC used in this work, Volterra series up to third order with memories m_1 = 256, m_2 = 8 and m_3 = 3 were used. The long memory in the linear kernel is required to capture reflections, which can occur in the cables between the amplifier and MZM and especially long cables between the DAC and amplifier (5 cm and 30 cm respectively). V_{rms} for the Volterra filter is increased from 700mV to 800mV because the pre-distortion is able to partially compensate the nonlinearities from higher voltages as shown in [7]. Lower voltages have lower nonlinearity from the power amplifiers but higher quantisation noise so optimum V_{rms} is determined by the balance of these two noises.

2.5.3 Comparison of pre-distortion techniques

The original contribution is described in the following text. The effect of using a Volterra series to predistort was investigated and compared to a linear pre distortion in an experimental setting. The dual polarisation modulator had a 3 dB bandwidth of 15 GHz and the DA were balanced amplifiers with 22 GHz bandwidth. Example kernel coefficients are shown in Fig. 2.7, calculated for a 46 GBd RRC channel with a roll off of 0.01 that carried PM-256QAM. Here the figure shows the frequency response of the overall system, indicating a small reflection at around 17 GHz. The colours in b) are normalised to the same colour bar in c), showing the captured nonlinear response of system. The size and the colour of the markers in c) describe the two degrees of freedom of the third order coefficients.

The results of using the Volterra series pre-distortion are shown in Fig. 2.8, where (a) shows the whole optical spectrum and (b) shows just the top. The bias voltages of the modulator were set to either be automatically controlled or manually adjusted to minimise the carrier. Here it can be seen that the most important aspect for getting a smooth output spectrum is to adjust the bias voltages appropriately. It is noted that for

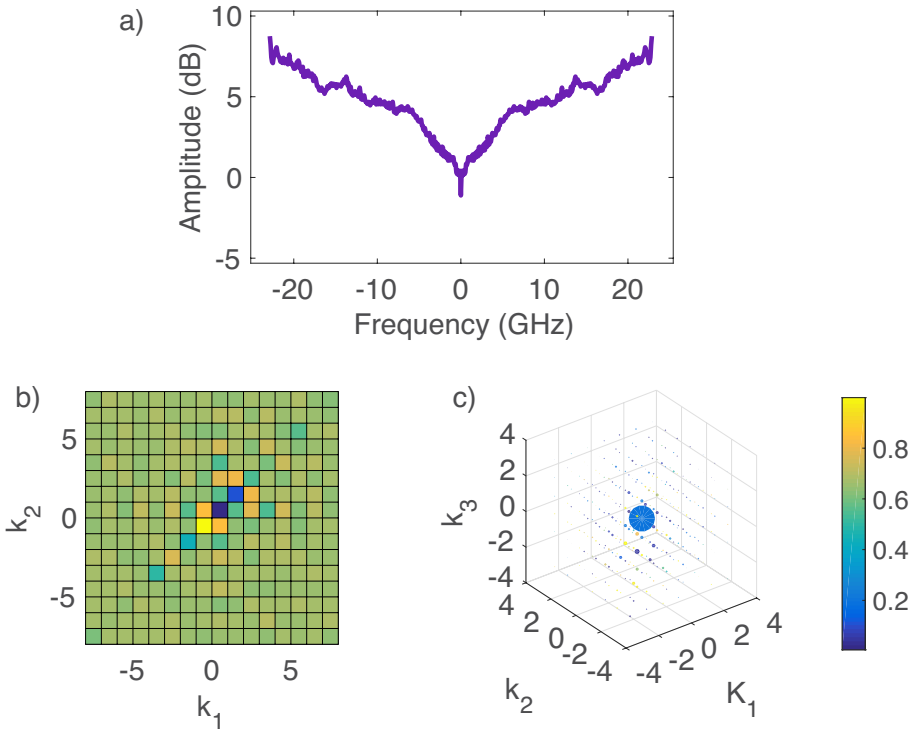

Figure 2.7: Experimentally obtained kernel coefficients for the signal path of the in-phase component of the X-polarization. (a) frequency response of the first order kernel, normalised coefficients for the second (b) and third (c) order kernel, with memories of 256, 8 and 3 long respectively.

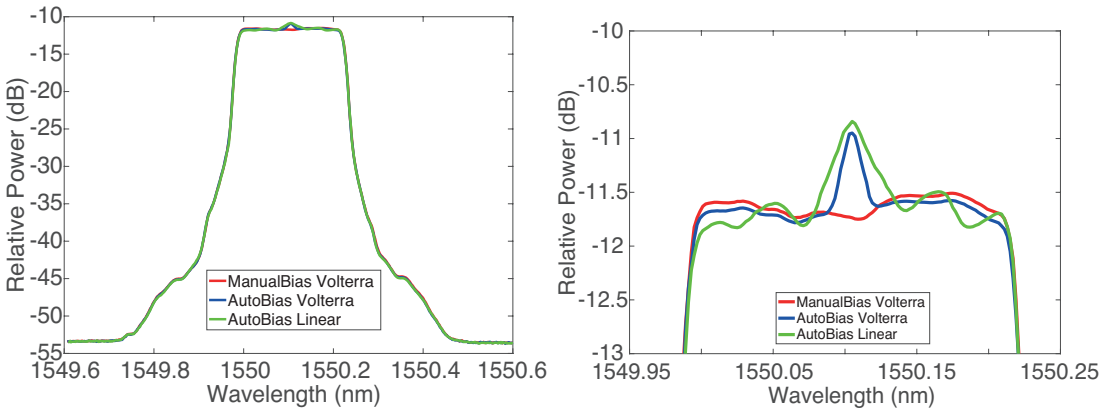

Figure 2.8: OSA plots showing the effect of using a linear filter or Volterra filter for electronic pre-distortion in the optical domain, taken with 0.02 nm resolution

this case the dual polarisation modulator had low output from one of the monitoring photodiodes, which may have led to the incorrect automatic biasing.

The Volterra filter and the linear filter both improve the response of the system, as the optical spectrum is flatter over the channel bandwidth. The residual response could be from the receivers response as the OSA trace is taken at the midpoint of the system before being converted back to a digital signal. It is noted that the generated 46 GBd signal is larger than the 3 dB bandwidth of the modulator at 15 GHz, showing

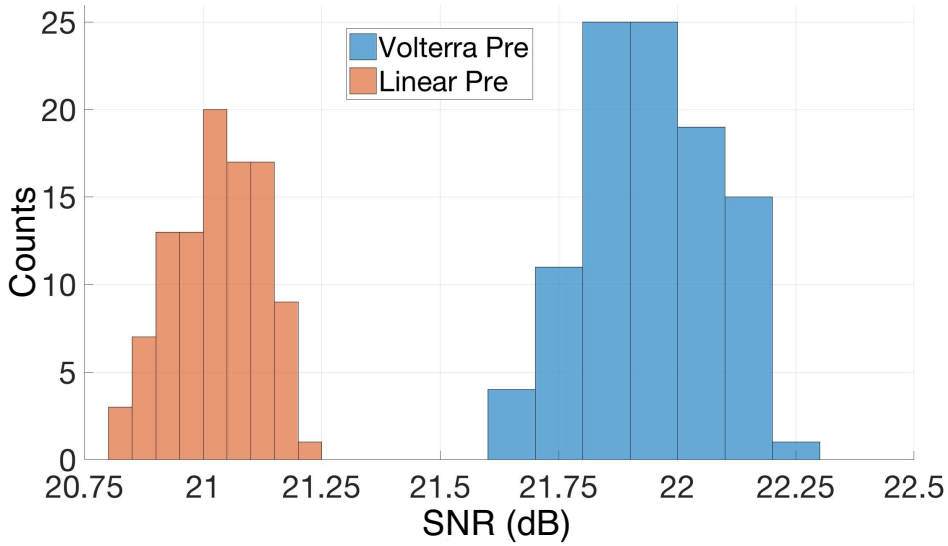

Figure 2.9: Histograms showing the back-to-back SNR over time for a Volterra pre-distortion and Linear pre-distortion

the benefit of pre-distortion.

It can be seen that using the Volterra filter does not alter the total bandwidth of the signal but only the frequencies inside the signal. When the Volterra filter is applied the incorrect biasing can be seen more clearly, allowing manual biasing to suppress the carrier by 1 dB. The optical spectrum can also be seen to be far flatter than the linear pre-distortion. It is noted that the modulator is very sensitive in its physical connections. This is due to the GPO connectors on the modulator, which according to their specification are one-time use but have been connected and reconnected multiple times before this experiment was conducted. The heavy use of these connectors affected the resultant transfer function of the transmitter. If the modulator was moved, the quality of the connection would change and hence the transfer function. This means that the linear and Volterra pre-distortion would need to be updated if the connections changed, in order to be correctly matched.

In order to quantify the effects of the two filters the resulting SNR needs to measured. Fig. 2.9 shows the measured SNR over time in a back-to-back configuration. Each histogram contains 100 measurements that were taken over a duration of approximately 1 hour. The mean SNR for linear and Volterra pre-distortion are 21.03 dB and 21.94 dB, respectively. This means the Volterra pre-distortion improved the received SNR by 0.92 dB, equivalent to a potential 0.66 bit increase in MI for 256QAM. It can also be seen that when using the Volterra pre-distortion the standard deviation of the SNR increases from 0.093 dB in the linear case to 0.13 dB. This is theorised to be due to the Volterra filter being more sensitive to the exact condition of the transmitter that it was tailored for. That is the particular bias point, state of polarisation and transceiver delays. The filter was optimised for this single particular transfer function so any devi-

ation from that function will cause a nonlinear shift resulting in a change of received SNR. It was noted that from the measured coefficients plotted in Fig. 2.7, spikes would appear in the first order of transfer function. This is likely to be due to poor RF connections where reflections setup standing waves, increase the loss of specific frequencies and the pre-distortion filter attempting to mitigate the loss.

A Volterra series was used to model the transfer function of the optical transmitter containing a MZM and DA. An increase is SNR was seen over the linearly pre-distortion technique for a symbol rate higher than the 3 dB bandwidth of the MZM. Increasing the back-to-back SNR may allow use of higher order modulation formats and increase the capacity of any optical transmission system that is transceiver noise limited.

The nonlinear pre-distortion technique described in this section is used in this thesis to improve the back-to-back performance of the transceiver in sections 3.3.4, 4.2 and 4.3.

3

Transmission Emulation

THIS CHAPTER FOCUSES on how transmission experiments can be conducted and emulated in controlled laboratory conditions. In an installed network link spans of fibre are placed between a transmit location and a receive location. The transmission over multiple spans requires optical amplifiers after each span in order to compensate for the periodic loss. This can be achieved in laboratories using a few different experimental approaches. Here, a recirculating loop is compared to a straight line link and the complications arising from wide band transmission are also discussed. The discussion in this chapter covers experiments and calculations that were conducted during the course of this PhD.

Due to fibre losses, signal transmission requires periodic amplification. This occurs in EDFAs which boost the signal back up but in turn add some noise. Amplification is performed repeatedly after each span until the receiver at the destination is met where the signal is processed and information is decoded. Optical transmission can be achieved in a lab by having all the required separate amplifiers and fibre spans connected. In order to minimise size, the fibre is kept on a reel. This setup where the required spans and EDFAs are connected in a row is called a straight line, which is a close approximation to an installed link. For cases where only a limited number of fibre spans are available, a recirculating loop can be used. This is where a loop is constructed containing the fibre, amplifiers to combat the loss of loop components and the signal is sent around this until a sufficient distance has been attained then sent to a receiver. Most of the work described in this thesis used a recirculating loop except for

section 4.4 where a straight line link is utilised.

3.1 Recirculating loop

One of the characteristics of transmission is the resulting OSNR profile. This is how the noise from the amplified and other optical components affect the achievable information rates. The closest to an installed fibre link that can be evaluated in the lab is the straight line link, followed by a multispan loop, then a single span loop. In schematic form, an installed fibre link would be identical to a straight line and have a very similar OSNR profile. The schematic for a single span loop is shown in Fig. 3.1. The implementation of a loop comes at the expense of additional loss for any transmission distance. These losses all require additional amplification in order to restore the signal power and this comes with associated additional noise. The OSNR profiles of each setup can be modelled using the following equation,

$$\text{OSNR} = \frac{P_{sig}}{P_{noise}} = \frac{P_{sig}}{N_A P_{\text{ASE}}}, \tag{3.1}$$

where P_{sig} is the power of the signal, P_{noise} is the total noise power, N_A is the number of amplifiers and P_{ASE} is the power of the amplified spontaneous emission (ASE) noise generated by each amplifier.

Inside a straight line the OSNR calculation follows Eq. 3.1, where P_{ASE} is calculated from setting the gain of each EDFA to equal the loss of the fibre span [8, 9]. For a recirculating loop the amplifier gain is set to overcome the span loss and the components inside the loop. Since the components inside the loop affect the OSNR reducing the loss of these components can mean an increase in performance. The loop coupler shown in Fig. 3.1 is typically 50:50.

The OSNR for a recirculating loop with a 50:50 coupler is as follows,

$$\text{OSNR}_{50:50} = \frac{P_{\text{in}}}{2P_{50} + N_A(P_{\text{span}} + P_{\text{loop}}) + (N_A - 1)P_{50}}, \tag{3.2}$$

where P_{in} is the power input to the loop, P_{50}, P_{span} and P_{loop} are the noise powers for overcoming the losses from a 50% arm of the coupler (3 dB), the fibre span and the loop respectively. The OSNR for a 10:90 coupler is as follows,

$$\text{OSNR}_{10:90} = \frac{P_{\text{in}}}{2P_{10} + N_A(P_{\text{span}} + P_{\text{loop}}) + (N_A - 1)P_{90}}, \tag{3.3}$$

where P_{10} and P_{90} are the noise powers for overcoming the losses for the 10% and 90% arms of the coupler, 0.45 dB and 10 dB respectively.

OSNR can now be calculated as a function of distance and this is shown in Fig. 3.2.

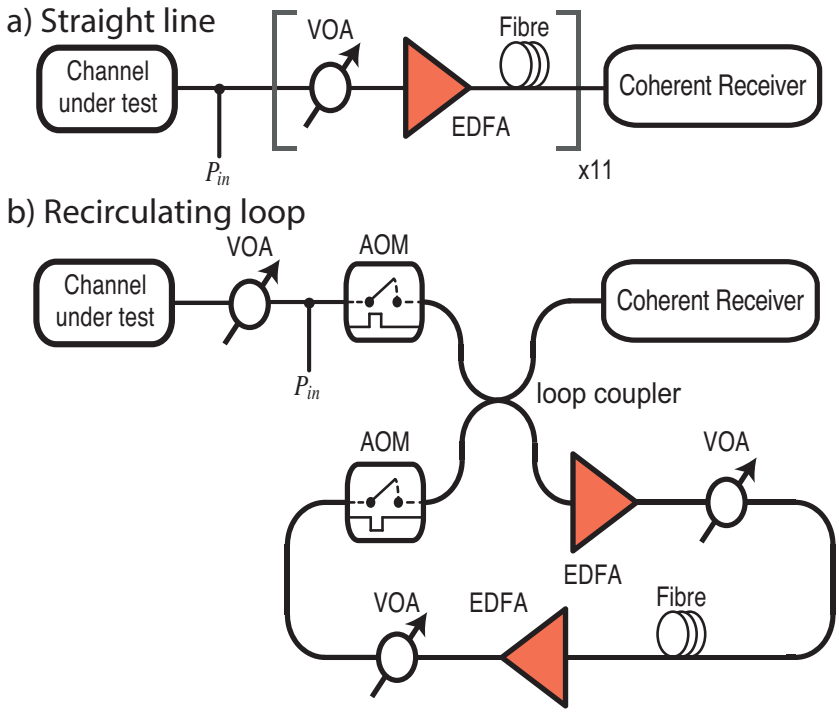

Figure 3.1: System setup for analysis of transmission OSNR impairment when using a) straightline and b) recirculating loop. Loop coupler can be 50:50 or 90:10 which changes the insertion loss and loop loss . The loop loss can be emulated with the VOA after fibre span.

For the case of a straight line link it can be seen that the OSNR in dB drops linearly with distance. When a recirculating loop with a 50:50 coupler is used the OSNR again drops linearly with distance but is 2.55 dB worse, which corresponds to a penalty in distance of 2500 km at an OSNR threshold of 15 dB. This is due to the loop losses which need to be overcome, on top of the loss from fibre span. When a 90:10 coupler is used in the loop it can be seen that at short distances the OSNR is worse than using a 50:50 coupler. The performance drop is due to the large loss in entering and exiting the loop. Then, after 1800 km, it can be seen that due to the lower loss of the coupler inside the loop the OSNR is higher than the 50:50 coupler.

Using Equation 3.2 and 3.3 the number of amplifiers at which the amount of accumulated noise power P_{ASE} for both cases is equal is,

$$N_A = \frac{2(P_{10} - P_{50})}{P_{50} - P_{90}}. \tag{3.4}$$

Multiplying this value by the length of the span gives the transmission distance at which the OSNR_{5050} and OSNR_{9010} cross over. It can be seen that this cross over point is independent of loop loss and fibre loss. If loop loss was larger the recirculating loop would perform even worse against the straight line case.

Fig. 3.3 shows the change in OSNR between a 50:50 and 90:10 coupler for three fibre span lengths 50, 80 and 100 km. For a larger span length the signal goes further

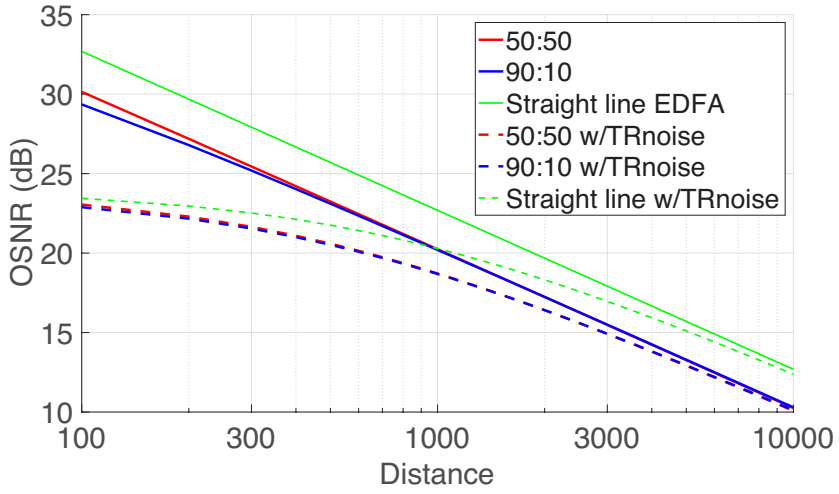

Figure 3.2: OSNR as a function of distance for a straight line system and compared to single span loop with different coupling ratios. Dotted line showing the OSNR when limited by transceiver noise to 24 dB, with a span length 100 km.

for each recirculation, this means the contribution to noise from the loop becomes relatively smaller so the effect of changing the coupler loss also becomes smaller. At 10,000 km of transmission it can be seen that the improvement in OSNR by using a 90:10 loop coupler is 0.1 dB whilst the drop in OSNR at 100 km is -1.1 dB. Different modulation formats perform best at different SNRs so this cross over point can be changed by altering the coupler ratio in order to get the best performance at a given distance. Given the magnitude of this improvement it can be concluded that changing the loop coupler is not an avenue worth pursuing as the gains are minimal compared to changing the number of spans inside the recirculating loop.

Here, the impact of imposing an upper limit to SNR is considered. Another factor P_{TR} is added to account for the transceiver noise, this sets the maximum possible SNR [39]. Equations 3.2 & 3.3 now become

$$\mathrm{SNR}_{50:50\mathrm{TR}} = \frac{P_{\mathrm{in}}}{2P_{50} + N_A(P_{\mathrm{span}} + P_{\mathrm{loop}}) + (N_A - 1)P_{50} + P_{\mathrm{TR}}}, \tag{3.5}$$

$$\mathrm{SNR}_{10:90\mathrm{TR}} = \frac{P_{\mathrm{in}}}{2P_{10} + N_A(P_{\mathrm{span}} + P_{\mathrm{loop}}) + (N_A - 1)P_{90} + P_{\mathrm{TR}}}, \tag{3.6}$$

where, $\mathrm{SNR}_{50:50TR}$ and $\mathrm{SNR}_{10:90TR}$ are the SNRs in the case of transceiver noise for a 50:50 and 90:10 coupler respectively.

The dashed lines in Fig. 3.2 show the SNR when the transceiver noise (TRnoise) limits the maximum achievable SNR to 24 dB, as described by Eqs. 3.5 & 3.6. It can be seen that the transceiver SNR impacts the received SNR heavily at the beginning of transmission. This is because the additional noise from the first amplifiers is small in comparison to the noise from the transceiver. As the distance increases it can be

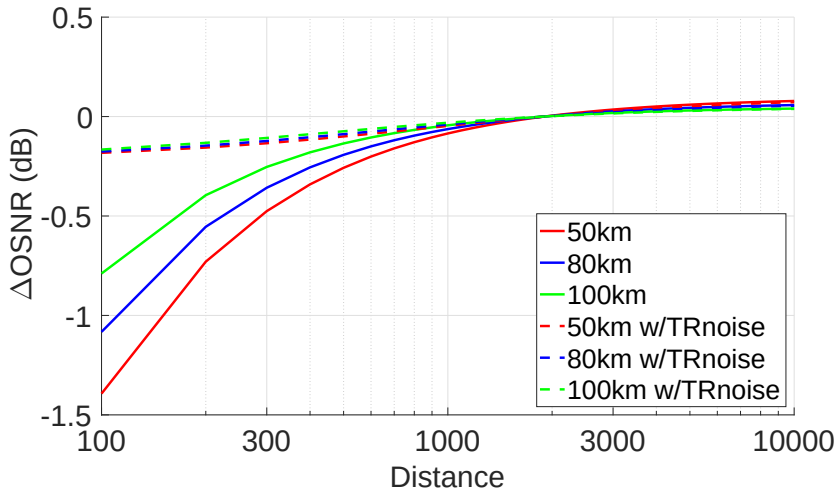

Figure 3.3: Change in SNR for 90:10 loop coupler relative to 50:50 as a function of distance. For one span of 50, 80 and 100 km with total loop loss of 9.4, 15 and 18.8 dB respectively. Dotted lines showing the SNR when limited by transceiver noise to 24 dB

seen that the SNR tends to that without transceiver noise. This is due to the transceiver noise becoming small in comparison to the total noise from transmission. It can be seen that cross over distance does not change when considering transceiver noise and impact of changing the coupler is reduced. At short distances the improvement in SNR becomes 0.2 dB and after the cross over always remains just slightly below that without transceiver noise.

3.2 Gain equalisation

Transmission emulation by using a recirculating loop has implications on OSNR, which has already been discussed, but here the experimental problems are addressed. The use of a recirculating loop implies that the signal is propagated around the same loop elements many times. Each element will have its own minor optical imperfections but since each piece is passed though multiple times the impairments on the signal due to said imperfections accumulate. Wavelength dependent loss, gain and polarisation dependent loss can become major issues. 2000 km transmission using a single 100 km span recirculating loop means the signal recirculates 20 times. For this distance a small loss of 0.4 dB at one frequency would multiply to 8 dB by the end of transmission.

To combat polarisation dependent loss, a loop synchronous polarisation scrambler is used. This device can change the state of polarisation of the light passing through by $\pi/2$ rad in 1.4 μs. By synchronising the changes in polarisation with the period of the light inside the recirculating loop, the state of polarisation can be randomised such that polarisation dependent loss is averaged out. The AOM switching speed is around 100 ns, negligible compared to that of the scrambler or the fibre propagation delay

400 μs.

Wavelength dependent loss requires more complex compensation, as each wavelength requires different levels of amplification to return to its flat state. In Fig. 3.1 a wavelength selective switch (WSS) is used to filter the transmitted signal. A WSS allows reprogrammable filtering of the broadband signal to maintain a flat spectrum. The result of flattening a signal means the overall loop loss will change. This will effect the OSNR by changing the effective loss of the loop and changing the input power to the following amplifiers. For EDFAs operating in constant output power modes a change in input power results in a change of gain. Due to characteristics of EDFAs different wavelengths have different gains and the wavelength dependent gain changes for different gains. The net effect of this inside a recirculating loop, is an unstable system that requires slow changes to achieve a flat spectrum.

In order to explore fibre nonlinearity, a sweep of launch power in to the fibre is a useful diagnostic as it demonstrates the highest possible performance as well as the changes with different parameters. A launch power sweep can vary from -14 dBm to 6 dBm per channel. This is a large dynamic range of 20 dB, which can create problems. A compounding experimental issue arises when considering varying the bandwidth being loading in the recirculating loop. A single channel 8 GBaud channel with RRC pulse shaping (see 2.4.1), would cover 8 GHz of optical bandwidth. In comparison, 7$\times$40 GBaud channels RRC pulse shaped would take up 280 GHz of bandwidth. As an example, the extremes of total power for these can vary from -14 dBm to 21 dBm. If this is extrapolated to loading a full C-band (of width 4 THz), a maximum total power of 33 dBm is expected. This means the recirculating loop needs to cope with a huge dynamic range of 47 dB. In order to minimise the dynamic range two configurations should be used, one for small bandwidths and another for broadband transmission experiments.

3.2.1 Experimental broadband transmission

The recirculating loop in Fig. 3.4 was implemented in order to investigate the issues with broadband transmission experiments. This information is then used to check the feasibility of experiments that require filling of the transmission bandwidth. Here, the channel under test was 4 THz of spectrally shaped-amplified spontaneous emission noise (SS-ASE) see section 3.3 for details. EDFAs with 33 dBm of output power were used in order to create and maintain sufficient power for full C-band launch power sweep. The EDFAs used were gain flattened to $\pm$1 dB for an amplifier gain of 33 dB. From characterisation tests it is noted that when the total input power changes by 1 dB the output can be seen to tilt by 0.25 dB/THz, so 1 dB over the total bandwidth.

The initial SS-ASE is generated by amplifying ASE then passing it through a WSS

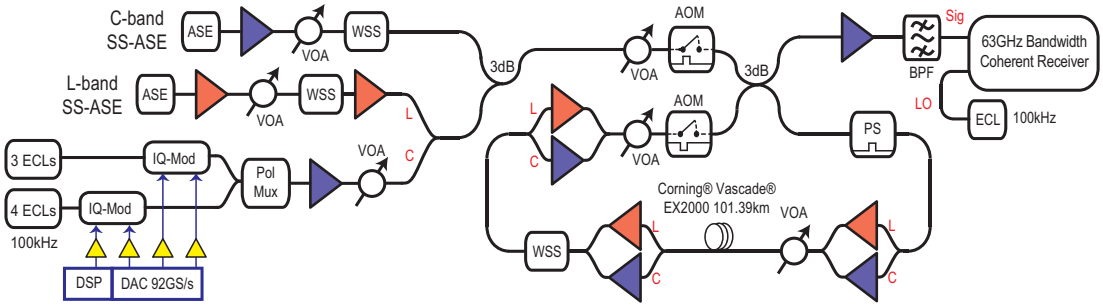

Figure 3.4: Experimental setup to investigate nonlinear distortions in wide bandwidth transmission.

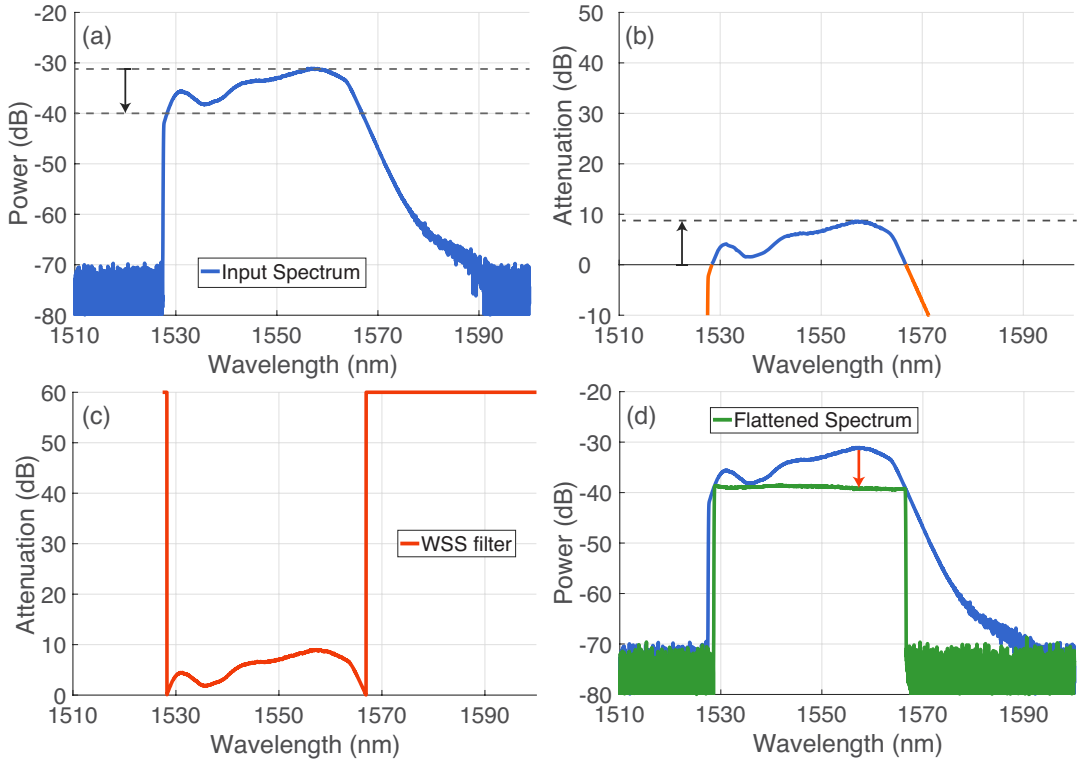

Figure 3.5: (a) Optical spectrum taken from an OSA with resolution of 0.05 nm. (b) Filter attenuation profile defined by dynamic range (c) Generated filter uploaded on to the WSS (d) Input and output spectra compared.

and then another EDFA. The high powered EDFAs used in this experiment have a minimum input power requirement. This means if the wavelength dependent loss is large, then the total loss will cause the subsequent EDFA to turn off so transmission cannot occur. Additional experimental problems were identified and overcome. Matching the power spectral density (PSD) of the SS-ASE to a channel, whilst maintaining power spectral density high enough in order to investigate the nonlinear effects involved using more attenuators than would be used for a narrow band system. This caused the back-to-back performance of the channel under test to be affected due to the additional variable optical attenuator (VOA)s.

The method for flattening ASE for use as SS-ASE, is shown in Fig. 3.5. First the

input to the span was monitored by an OSA. This trace is used as the basis for the WSS custom filter. A dynamic range, over which flattening is permitted, is defined, limiting the maximum attenuation that can be used by the WSS. The wavelength with the highest power of the trace is found and the trace is inverted. The entire trace is then translated up until the previously found largest power is set to the maximum attenuation permitted by the dynamic range. Then, all wavelengths with a negative attenuation were set to block (60 dB). This generates a filter with attenuation as a function of wavelength that would flatten with one pass through the WSS. The attenuation is then divided by the number of recirculations as the signal will pass through the WSS that many times. This filter is then applied to the WSS and the resultant output is monitored using an OSA. If the change in attenuation from updating the filter was large, there will be a change in EDFA gain, which results in a change of gain tilt and the output will not be flat. If this is the case, the resultant output can then be used to update the filter recursively, to obtain a flatter output. This iterative process fails to flatten if used more than 3 times at the same number of recirculations, as small errors start to multiply. To obtain a flat output at different distances, the number of recirculations was started from 1 where a filter is obtained, then the number of recirculations are doubled and a filter update is obtained. This method iteratively adjusts the attenuation such that the WSS does not update with large adjustments in total attenuation. Incrementing the launch power by 1 dB at distances greater than 4 recirculations was found to cause too large a change in tilt. This necessitated for every change in launch power starting a new filter from scratch. That is, returning to 1 recirculation, adjusting the launch power and then following the above process until returning to the desired number of recirculations. A practical issue with this method is that updating the filter can change the launch power, so this also must be monitored in order to obtain the desired launch power.

4 THz of flat SS-ASE was launched into the recirculating loop and was flattened by the WSS for each number of spans. Fig. 3.6 shows the measured optical spectrum after the fibre span after 2, 4, 8, 16 and 32 spans of transmission using the previously described technique. The curve labelled 32BPF is where the WSS was set to a band-pass filter to suppress ASE outside the bandwidth of interest and pass the SS-ASE. It can be seen that the flattening done by using the above algorithm is very effective at maintaining a flat power spectral density.

Fig. 3.7 was obtained in the same way as Fig. 3.6 but with a different scale and is used to illustrate the limits of flattening. The small fluctuations in power seen in Fig. 3.7, are due to the uploaded filter. The uploaded bandpass filter does not have any fluctuations over fine wavelength grid, neither does the associated output. This is in comparison to the recirculation filters which contain fine wavelength attenuation adjustments, which are magnified by the recirculations. It can also be seen that fluctuations are unique for each total number of recirculations as a different filter is used for

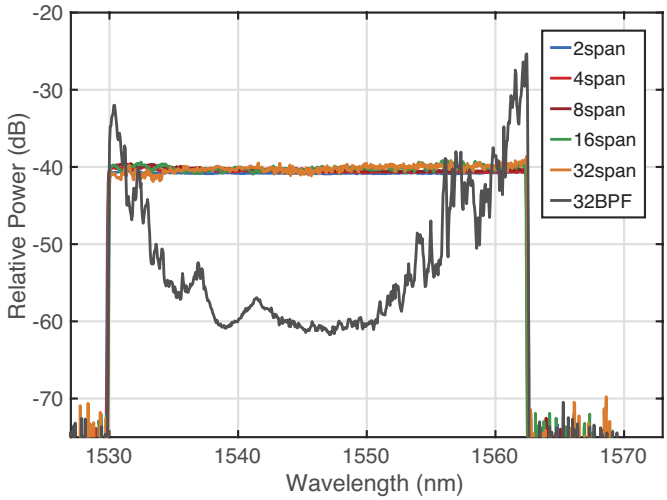

Figure 3.6: Optical spectrum taken from an OSA with resolution of 0.1 nm after varying the number of recirculations. The WSS being used as a GFF was optimised in every case except 32BPF. This trace shows the spectrum with the WSS set to a band pass filter at 32 recirculations.

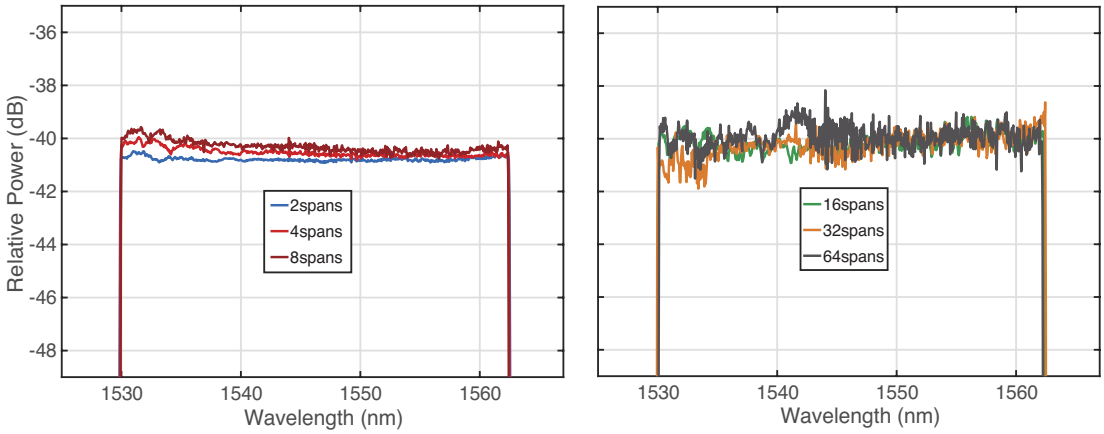

Figure 3.7: Subset of data from Fig 3.6 for clarity, showing the optical spectrum taken from an OSA with resolution of 0.1 nm.

each case. The low power spectral density (-10 dBm/10 GHz) of this trace means the effect of four wave mixing (FWM) should be negligible and hence is not a factor in the overall flatness.

No published broadband transmission experiments show any SNR measurements as a function of launch power so there is novelty in measuring SNR for large bandwidths. This demonstrates that nonlinearity is still a limiting factor in setting maximum achievable rates. This was attained and published in [115] using SS-ASE and a recirculating loop and is shown in Fig. 3.8. In section 4.4 a straight line link is used and transmission of 112 channels covering 4.2 THz a full C-band. This technique was also used to investigate interchannel stimulated Raman scattering over 9.1 THz of bandwidth [114].

Fig. 3.8 shows the system performance was evaluated after transmission over a fixed distance of 1010 km, corresponding to 10 spans. This distance provides enough

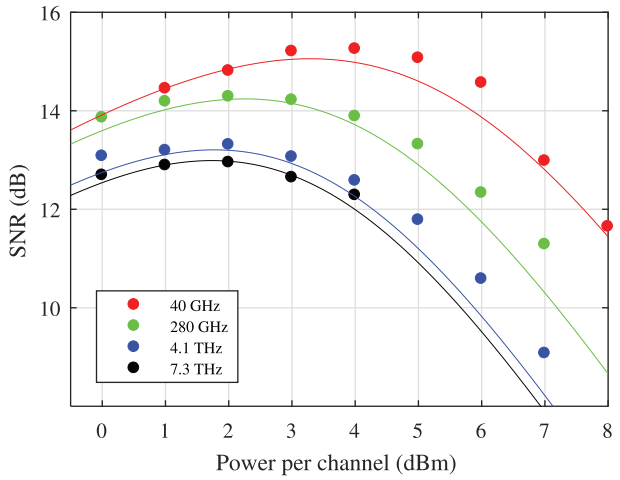

Figure 3.8: SNR performance of the transmission system utilising SS-ASE for different transmitted bandwidths after 1010 km of propagation, solid lines represent the predictions obtained using Eqn. 4.9 and markers correspond to experimental data. Taken from [115].

accumulated dispersion for the GN model assumptions on signal Gaussianity to be valid. The signal launch power per channel was varied between -1 and 7 dBm and SNR of the received signal was measured. The SNR as a function of the signal launch power for different transmitted bandwidths is shown in Fig. 3.8. In the linear regime, a small difference in receiver SNR can be observed among the different transmitted bandwidths, this is due to the power equalisation process carried out by the WSS within the recirculating loop. As the propagated bandwidth is increased, the tilt from the EDFAs becomes larger and the WSS must intervene in an increasingly manner to correct the tilt, leading to a small difference in the overall loop loss. Towards the highly nonlinear regime, for a fixed signal launch power, a penalty in SNR can be observed with increase of transmission bandwidth, as expected from the growth of the NLI noise power. For instance, at a launch power of 4 dBm per channel, the difference observed in SNR between the transmission bandwidths of 40 GHz and 7.3 THz is approximately 2.7 dB. Fig. 3.8 additionally depicts the theoretical performance of the system (solid lines) for all the evaluated bandwidths obtained using Eq. 4.9. One well-known limitation of the GN-model is the assumption is that the transmitted signal behaves statistically like Gaussian noise, neglecting this way modulation format dependence of the NLI noise. Even though this has been addressed in the literature [15, 25] it leads to additional complexity when computing the NLI noise power, specially for large bandwidth systems. This limitation is translated in an overestimation of the NLI noise by the GN model compared to the use of QAM modulated signals, and therefore a underestimation of the system performance in the nonlinear regime. Using the experimental data, the model was confirmed to give a slightly pessimistic prediction of performance in the nonlinear regime for the all evaluated bandwidths.

3.3 Bandwidth emulation using spectrally shaped noise

Transmission over broad bandwidths is a very expensive and resource consuming avenue for research in capacity. In an AWGN channel achievable capacity is linearly proportional to bandwidth. This means pushing record transmission rates further requires broadband transmission. The success and widespread deployment of EDFAs now presents a limitation to capacity growth, as the available gain bandwidth, over which WDM signals can be transmitted, is limited to approximately 5 THz for the conventional band (C-band) and 8 THz for the C+L band. Given a fixed bandwidth limit, one way to increase the transmission rates is to increase the system signal-to-noise ratio (SNR), and the spectral efficiency [76].

As is well known, the optical fibre channel is subject to Kerr nonlinearity; its refractive index depends on optical intensity (Eq. 2.2.1). This causes nonlinear phase shifts and the signal is irreversibly distorted from the interaction between nonlinearity and amplified spontaneous emission noise, reducing the SNR. Techniques to increase the SNR in the presence of nonlinearity have been proposed such as digital back propagation [75], coded modulation schemes [76] or novel equalising strategies [86]. However, the question of how these techniques perform in a practical, fully loaded C-band transmission system needs to be answered for every studied system, and simply extrapolating is not reasonable.

Transmission experiments with bandwidths using the full C-band require a large number of channels, which comes at the expense of more complex experimental implementation; the use of additional light sources and modulators to implement independent channels can require large banks of laser sources, modulators and schemes to overcome data correlation issues. An attractive alternative, due to its simplicity, is the use of spectrally shaped-amplified spontaneous emission (SS-ASE) instead of independently modulated channels. This technique has been shown in [28, 80], and has been used in C-band experiments [20, 38, 86, 148] as well as extended L-band transmission [115].

As shown through extensive theoretical models the use of signals with Gaussian statistics, similar to noise, give a lower bound on system performance compared to modulated channels [15, 82, 95]. In the Gaussian noise (GN) model, the nonlinear distortions are represented as an additional noise term in the overall system signal-to-noise ratio, and referred to as NLI noise [95]. Corrections for modulation format can be applied to the GN model to make what is termed the enhanced Gaussian noise (EGN) model [15], which addresses the non Gaussianity of the signals. These models can be used to estimate the expected performance from using SS-ASE and modulated channels as interferers.

In this section the use of SS-ASE as a channel loading scheme is evaluated, com-

pared to modulated interferers and the effect of the additional NLI noise from this scheme on 4QAM and 64QAM modulated channels is quantified. The EGN model was used to verify the experimental results. Advanced transmission systems operating at 400 Gb/s and higher use coded modulation to achieve the required high spectral efficiencies, hence, the penalty in terms of MI was also investigated as a function of distance. This enabled the impact of SS-ASE as a loading source to be quantified in terms of achievable information rate.

3.3.1 Statistics of SS-ASE

In dispersion uncompensated links, one source of discrepancy between the Gaussian noise model and system performance comes from the modulation format dependence of the nonlinear distortion [16]. To investigate the suitability of SS-ASE for use as a substitute for transmission channels, a statistical analysis has been conducted and the evolution of the electric field probability density function (PDF)s, have been compared. This allows for the quantification of how much accumulated dispersion is required for each format's PDF to evolve into a steady state. It has been shown that without dispersion, the samples of the In-Phase (I) and (Q) Quadrature components of PDM-QPSK evolve into a Gaussian-like distribution after transmission over 500 km of SMF [16]. Even under this steady state the underlying process of the signal is non-Gaussian and so modulation format dependence of NLI is observed [24, 89].

To investigate the statistics of SS-ASE simulations were employed using the split-step Fourier method. Two independent sets of data channels, modulated with Nyquist pulse shaped QPSK and 16QAM channels, and an SS-ASE channel were generated and compared. A pseudo-random binary sequence (PRBS) was used to generate PDM-QPSK and 16QAM channels, at 10 GBaud and 2 samples per symbol, and then Nyquist pulse shaped with a root raised cosine (RRC) filter with a roll-off factor of 0.001 (shown in Appendix B) in order to obtain minimum subchannel spacing without crosstalk and a spectrally flat superchannel that matches SS-ASE. The electric field was oversampled to 8 samples per symbol to avoid simulation artefacts. The launch power was set to -10 dBm per channel [Launch power was swept from - 20 to 0 dBm in simulation with no significant change in statistical evolution; the electric field is dominated by dispersion rather than the nonlinear distortion at these powers].

Propagation over fibre was evaluated using the split step Fourier method to solve the nonlinear Schrödinger equation Eq. 2.12 with a step size of 0.1 km. The fibre parameters were set as follows: dispersion 16 ps/nm/km, attenuation 0.16 dB/km and nonlinear coefficient 1.1 $(Wkm)^{-1}$. The fibre span length was set to 80 km and an EDFA with 5 dB noise figure was implemented to compensate for the fibre loss.

To realise a SS-ASE channel, white Gaussian noise was generated as I and Q ele-

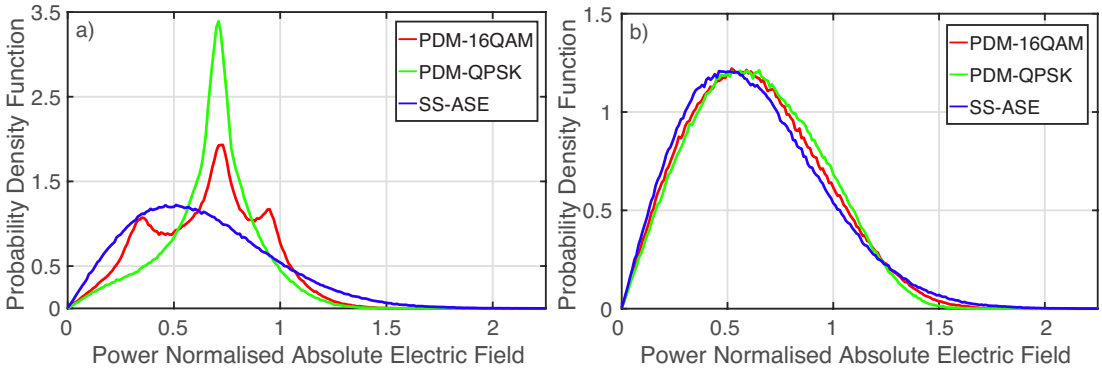

Figure 3.9: Probability density functions of absolute electric field for SS-ASE, Nyquist pulse shaped PDM-16QAM and PDM-QPSK at (a) transmitter and (b) after 240 km of fibre propagation.

ments of the electric field. Use of Gaussian statistics for both I and Q gives rise to a Rayleigh distribution in the absolute value of electric field, as shown in Fig. 3.9. The white noise is then filtered by a 10 GHz 'brick-wall' bandpass filter in order to achieve a signal with the same spectral width as the modulated data channels. The power was set to match the PSD of the PDM-QPSK and 16QAM channels. The PDFs, shown in Figs. 3.9 (a) & (b), were taken of the power-normalized electric field, which is the absolute value of electric field divided by the square root of average power in the channel; such that the PDF does not scale as the signal power varies with fibre loss. The signal distributions at the transmitter are shown in Fig. 3.9 (a). The PDM-QPSK and PDM-16QAM signals are be expected to show 1 and 3 peaks, respectively, in electric field magnitude as the symbols have discrete amplitudes. However, as can be seen from Fig. 3.9 (a) the peaks are broadened due to the Nyquist pulse shaping.

The field amplitude distribution of the three signals after propagation over 240 km is shown in Fig. 3.9 (b). It can be seen that, due to accumulated dispersion, noise and fibre nonlinearity, the PDM-QPSK and PDM-16QAM signal amplitude distributions have almost converged to that of the SS-ASE. After this distance the SS-ASE, PDM-16QAM and PDM-QPSK signals have variances with similar values of 0.108, 0.099 and 0.095, respectively.

To characterise the evolution of the signal amplitude distribution with propagation distance, the evolution of the peak to average ratio (PAR) of absolute value of electric field is shown in Fig. 3.10. It can be seen that, the SS-ASE's PAR does not change during transmission but both the PDM-16QAM and PDM-QPSK signals converge to the same ratio as the SS-ASE. The PDM-QPSK has a higher initial PAR and converges to SS-ASE after approximately 240 km whilst the PDM-16QAM takes only 180 km.

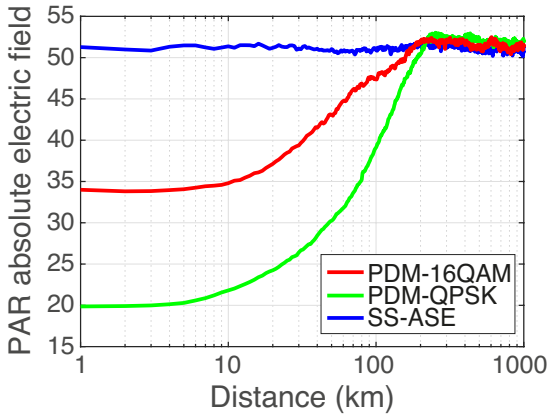

Figure 3.10: Peak to average ratio (PAR) of absolute electric field as a function of distance for: PDM-QPSK, PDM-16QAM and SS-ASE.

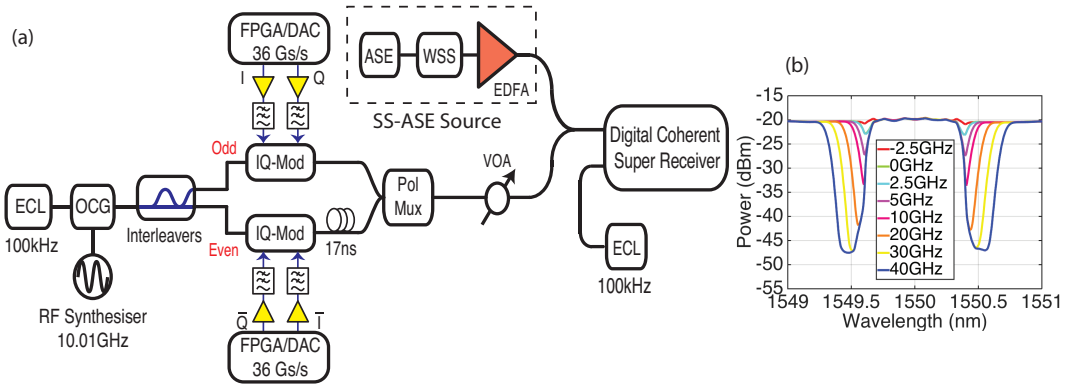

Figure 3.11: (a) Overall system setup consisting of an external cavity laser (ECL), optical comb generator (OCG), IQ modulators, polarisation multiplexer (Pol Mux). The recirculation loop uses acousto-optic modulators (AOM), variable optical attenuators (VOA). (b) Optical spectra of SS-ASE and 9 sub- channel superchannel with various guardbands.

3.3.2 Experimental generation of SS-ASE

The experimental setup used to quantify the effects of using SS-ASE, in terms of SNR and achievable rate, is shown in Fig. 3.11 & Fig. 3.13. The transmitter consisted of two sections, namely the SS-ASE source and the digital channel transmitter.

The SS-ASE source was initially designed as shown in Fig. 3.11. The SS-ASE was generated from an ASE noise source and was launched into a WSS, followed by an EDFA with an output power of 19 dBm. The WSS was used to limit the bandwidth of the ASE noise source and flatten the ASE spectral profile by pre-emphasising for the gain profile of the following EDFA. The SS-ASE was then combined with the superchannel source using a 3 dB coupler. The PSD of the SS-ASE noise and the superchannel were matched to within 0.3 dB, as shown in Fig. 3.11 (b). The power of the combined signal was measured using an OSA with a resolution of 0.1 nm. This enables emulation of a reconfigurable number of SS-ASE channels with arbitrary spacing and bandwidth.

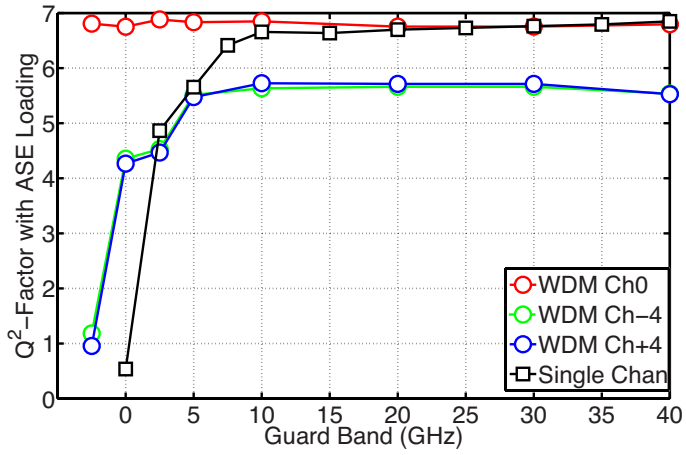

Figure 3.12: Back-to-back performance for the central (Ch0) and outermost subchannels (Ch±4) of the test superchannel with SS-ASE loading. Also shown as squares is the performance of a single channel system.

The back-to-back (BTB) performance was measured to verify the impact of combining the superchannel with 720 GHz of SS-ASE before transmission impairments. The effect of changing the SS-ASE's proximity to the superchannel (hence guardband) was investigated, with the results shown in Fig. 3.12. The WSS used for shaping is not a perfect filter, see Fig. 3.11 (b); it has a specified resolution of 12 GHz, a roll-off of 1.0 dB/GHz and a finite extinction ratio limit of 35 dB. After subsequent amplification to match spectral density the extinction becomes 27 dB, which results in linear crosstalk, even for large guardbands. The Q-factor as a function of guardband between the superchannel and the SS-ASE for the central subchannel and outermost subchannels (±40 GHz relative to the central subchannel) is shown in Fig. 3.12. For guardbands greater than 10 GHz, the outermost subchannels (Ch±4) exhibited an additional penalty of 1 dB compared to the central subchannel (Ch 0). This penalty in performance was due to the limited effective number of bits in the ADCs used in this work. When the guardband was less than 10 GHz, a penalty was observed on the outermost subchannels arising from linear crosstalk, whilst Ch 0 maintained the same performance. The impact of the SS-ASE guardband when the superchannel was replaced with a single channel is also characterised. In this case the linear crosstalk can be seen occurring at just below 10 GHz, which is a larger guardband than that corresponding to the outermost subchannels. This was because a single channel is subject to crosstalk from both sides and the WSS resolution. When the guardband was larger than 10 GHz the performance was unaffected by the SS-ASE as the only noise added arose from the extinction ratio rather than the WSS roll-off. The spectral distance between the SS-ASE and the channel under test was minimised, in order to maximise spectral efficiency, but not incur a linear penalty; the transmission experiments were conducted with a guardband of 5 GHz.

In the subsequent experiments the SS-ASE source was improved by launching an ASE noise source into an EDFA with an output power of 27 dBm, followed by the WSS. The WSS cut a notch into the ASE with a width of 43 GHz centred on the carrier frequency of the CUT. The SS-ASE source was improved by updating the design, such that the WSS was the last component in the chain. This improved the extinction ratio in the notched section of the SS-ASE and the SS-ASE is amplified after being combined with the CUT mitigating the extinction ratio contribution. Emulating a larger bandwidth channel takes away the dependancy on the WSS roll-off so the channel under test was set to have a symbol rate of 40 GBd. The next subsection describes the GN model, which can be used to estimate the expected difference in nonlinear noise from different modulation formats and using SS-ASE.

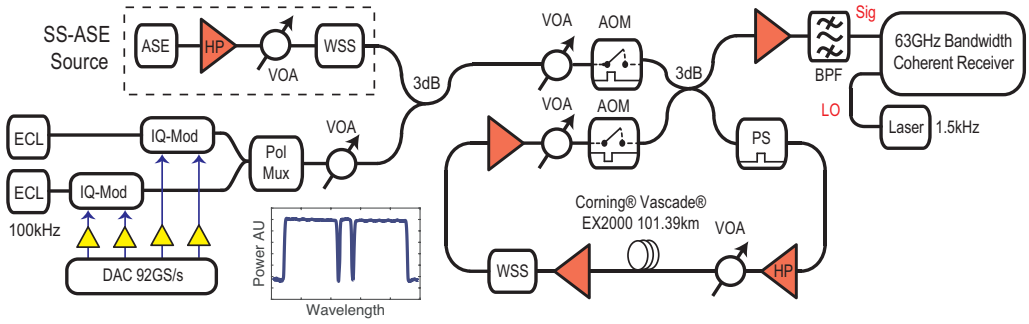

Figure 3.13: Experimental Setup, showing the SS-ASE source constructed from an ASE source, high power (HP) EDFA, variable optical attenutator (VOA) and wavelength selective switch (WSS), the digital transmitter using external cavity lasers (ECLs), polarisaton multiplexer (Pol. Mux.) and IQ modulators (IQ Mod.), and a recirculating loop using acousto-optic modulators (AOMs), polarisation scrambler (PS) and WSS for gain flattening and a band pass filter just before the coherent receiver. Inset, optical spectrum showing one channel with 240 GHz of SS-ASE.

3.3.3 SS-ASE modeling

Research on the nonlinear fibre channel has led to various mathematical models to predict the NLI and hence the received SNR, which is used in system design and achievable rate estimations. These models use expressions to provide a theoretical understanding of the experimental phenomena being investigated. A commonly used model due to its simplicity is the GN model [95]. This model has limitations as it assumes the CUT and interfering channels are made up of Gaussian noise (spectrally shaped as the actual channels) or, equivalently, by channels modulated by a Gaussian constellation. To properly account for non-Gaussian modulation formats, such as QAM, corrections have been applied to obtain the EGN model [15], which is used here. To confirm experimental results with the different schemes of interferers the GN and EGN models were used together to estimate the amount of NLI and hence the SNR of the CUT and hence the achievable rate can also be estimated.

The received SNR can be expressed as [39],

$$\mathrm{SNR} = \frac{P}{N^{(1+\varepsilon)}\eta P^3 + \kappa P + N P_{\mathrm{ASE}}}, \tag{3.7}$$

with signal power P, the number of spans N, the coherence factor ε, the NLI coefficient for the entire link η and the ASE noise power from each amplifier P_{ASE}. The transceiver $\mathrm{SNR_{TR}} = 1/\kappa$ is the maximum SNR that can be achieved in the transmission system in the absence of NLI and ASE noise. This variable phenomenologically includes all impairments of the system under test and can be measured in a back-to-back configuration without ASE noise loading. In this work, a $\mathrm{SNR_{TR}}$ of 20.1 dB was measured. The NLI coefficient η includes contributions from self phase modulation, cross phase modulation and four-wave mixing [15].

It has already been shown that the input distributions of the transmitted channels affect the amount of NLI [129] and this has been verified experimentally [37]. It has been shown that the amount of additional NLI is related to 4^{th} standardised moment (kurtosis) of the modulation format. The excess kurtosis of a complex random variable (kurtosis minus 2) such as a QPSK modulated signal is -1, whilst for SS-ASE it is 0. The higher the kurtosis the larger the nonlinear distortion [129]. The excess kurtosis is used as an input to the EGN in order to calculate η and hence each modulation format has its own respective η.

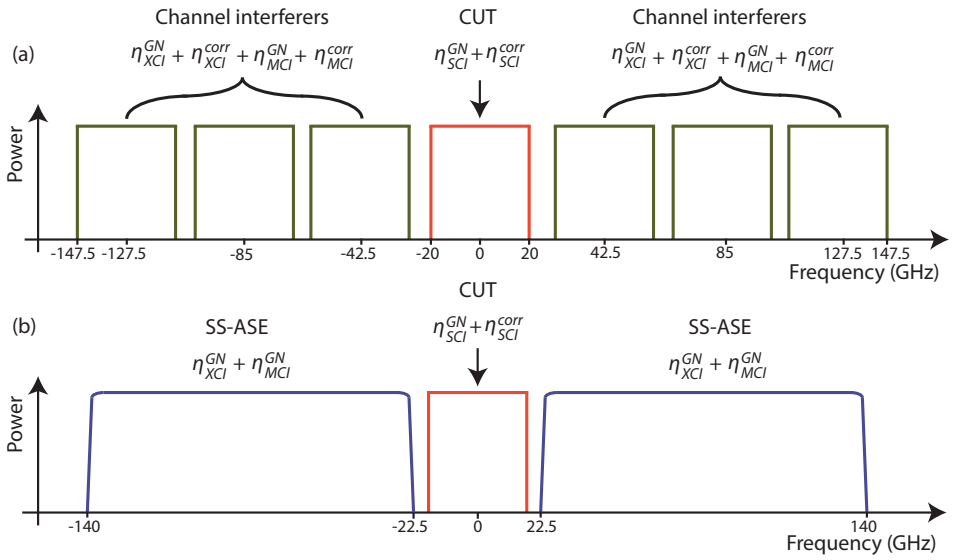

Figure 3.14: Diagrammatic setup showing the optical spectra for two different interfering schemes for the CUT. (a) 6 channels carrying modulated data and (b), spectrally shaped ASE with the same occupied bandwidth

The EGN model was used to estimate the SNR of the channel under test with modulated channels as interferers. The correction from [15] was applied for self channel interference (SCI), multi channel interference (MCI) and cross channel interference (XCI) accounting for the modulation format dependence of the NLI noise. When

using SS-ASE as an interfering channel, the EGN model was used to calculate the self channel interference but the correction for XCI and MCI are not applied. This corresponds to the GN model being used to model the behaviour of interferers. That is the overall NLI coefficient for all channels (η_{chans}) and SS-ASE ($\eta_{\text{SS-ASE}}$) are calculated as follows,

$$\eta_{\text{chans}} = \eta_{\text{SCI}}^{(\text{GN})} + \eta_{\text{SCI}}^{(\text{corr})} + \eta_{\text{XCI}}^{(\text{GN})} + \eta_{\text{XCI}}^{(\text{corr})} + \eta_{\text{MCI}}^{(\text{GN})} + \eta_{\text{MCI}}^{(\text{corr})}, \tag{3.8}$$

$$\eta_{\text{SS-ASE}} = \eta_{\text{SCI}}^{(\text{GN})} + \eta_{\text{SCI}}^{(\text{corr})} + \eta_{\text{XCI}}^{(\text{GN})} + \eta_{\text{MCI}}^{(\text{GN})}, \tag{3.9}$$

where $\eta_{\text{SCI}}^{(\text{GN})}$, $\eta_{\text{XCI}}^{(\text{GN})}$ and $\eta_{\text{MCI}}^{(\text{GN})}$, are the NLI coefficient contributions from the Gaussian noise model for self channel interference (SCI), cross channel interference (XCI) and multi channel interference (MCI) respectively and $\eta_{\text{SCI}}^{(\text{corr})}$, $\eta_{\text{XCI}}^{(\text{corr})}$ and $\eta_{\text{MCI}}^{(\text{corr})}$ are the NLI coefficient corrections from the EGN model for SCI, XCI and MCI respectively. This is shown diagrammatically as optical spectra in Fig. 3.14. The additional $\eta_{\text{XCI}}^{(\text{corr})}$ contributions that have modulation format dependence of the CUT itself have been neglected. It is noted that the correction terms are always negative, this means that SS-ASE will theoretically generate more NLI than a modulated channel.

The modelling of SS-ASE is carried out by assuming that the power spectral density is flat. This is unlike the case of channel interferers in which guardbands are placed between each channel. In order to mitigate the discrepancy in transmitted bandwidth between the two cases, the total occupied bandwidth was maintained.

3.3.4 Experimental evaluation of SS-ASE

The WSS was used to limit the total bandwidth of the ASE noise source to 240 GHz and flatten the spectral profile by attenuating the wavelengths as necessary, in order to emulate the Nyquist spaced channels as shown in Fig. 3.14. To evaluate the performance of the system using SS-ASE all the external cavity lasers (ECL)s at the transmitter, with exception of the CUT, were switched off, allowing the coupling of the CUT with the SS-ASE. The performance of channel interferers was evaluated by using all 7 ECLs and switching off the SS-ASE source, allowing transmission of modulated channels only.

The digital transmitter used in the subsequent experiment does not use an optical comb generator and was constructed as follows. Drive signals were generated from a sequence of random data 2^{16} bits long before being mapped to either 4QAM or 64QAM symbols, as required for multiformat comparisons. These digital signals were then nonlinearly pre-distorted using a Volterra filter to compensate for the non-ideal transmitter components [7, 59] as described in section 2.5.2. The symbol rate was set to 40 GBaud and then a RRC filter with a roll-off of 0.001 was applied. These

40 GBaud signals were uploaded to 92 GSa/s DACs and were amplified before going into 2 separate IQ modulators. Two groups, one of 4 and one of 3 ECLs, with 100 kHz nominal linewidth, were passed into the single polarisation modulators such that independent odd and even modulated channels were obtained. The spacing of the lasers was set at 42.5 GHz. The output of the modulators went into a polarisation multiplexing emulator in order to generate polarisation division multiplexed signals.

The output of the digital transmitter was then combined with the SS-ASE source using a 3 dB coupler. The power spectral density of the SS-ASE noise and the transmitter were matched to within 0.3 dB. The power of the combined signal was measured using an OSA with a resolution of 0.1 nm. The setup enables emulation of a re-configurable number of SS-ASE channels with arbitrary spacing and bandwidth with an improved performance compared to that reported in [29]. The extinction from the stop band to the pass band was 35 dB and an EDFA with higher output power of 33 dBm allowed a larger ASE bandwidth to be filled whilst maintaining a constant power spectral density.

For transmission, a recirculating loop was used, with a loop synchronous polarisation scrambler (PS), and a single span of 101.39 km of Corning Vascade EX2000 fibre with a total loss of 16.2 dB. The span was followed by an EDFA with 18 dBm output power and 5 dB noise figure to overcome fibre attenuation. This was followed by another WSS which was used as a programmable gain flattening filter to compensate gain tilt from the optical amplifiers, followed by another EDFA in order to overcome the remaining component losses. An ECL with 12 dBm output power and 1.5 kHz nominal linewidth was used as the local oscillator in the coherent optical receiver. Detection was carried out using balanced photodetectors with an optical bandwidth 140 GHz. The received signals were captured by a real-time digital oscilloscope with an optical bandwidth 126 GHz at 160 GSa/s. The symbol rate and spacing is such that 3 channels can be simultaneously captured. The complete setup is shown in Fig. 3.13.

The captured traces were processed offline, applying the DSP chain shown in Appendix B. A correction for IQ delay in the receiver was applied, followed by ideally compensated chromatic dispersion. The signal was then root raised cosine filtered before equalisation. The equalisation was performed by a 61 tap least mean squares radially directed equaliser with using a constant modulus algorithm for pre-converge. The frequency offset between carrier and LO was then estimated before a decision directed algorithm was used for carrier phase estimation using 256 taps. Gram-Schmidt orthogonalisation procedure (GSOP) was finally performed to compensate for suboptimal phase biasing of the transmitter IQ modulators. Decisions were then made on the symbols and compared to the ones that were sent to calculate a SNR. Then MI was calculated over both polarisations, using the sent and received symbols for the experiment, and for the model as a function of the measured SNR and modulation format; details of the MI calculations are in Chapter 2.1.2.

The channel under test was modulated with either 4QAM or 64QAM data and propagated over 20 recirculating fibre loop spans, with a total distance of 2028 km. For bandwidth loading two schemes were used, with channels either carrying the same modulation format as the CUT or loaded to the same bandwidth of 282.5 GHz with SS-ASE, from here on referred to as channel interferers and SS-ASE respectively. The results from sweeping the launch power, the transmission distance and varying the total transmission bandwidth follow.

3.3.5 Launch power investigation

The received SNR was experimentally measured for launch powers in the range -5 to +7 dBm per channel, and is shown in Fig. 3.15 (a) and Fig. 3.16 (a) for 4QAM and 64QAM respectively. For modelling channel interferers using the EGN, a channel spacing of 42.5 GHz was used. For SS-ASE a flat spectral density was assumed and the width of the CUT was taken as 42.5 GHz, which includes the guardband. Considering the remaining guardbands, the SS-ASE bandwidth was limited to that occupied by the channels not including the guardband i.e. 240 GHz. It can be seen that for both schemes of interfering channels the performance of the CUT at low launch powers is identical. This is due to the main source of noise being P_{ASE} from the EDFAs. As the launch power was increased the performance of the CUT was affected by NLI noise and the performance achieved a maximum and then started to decrease.

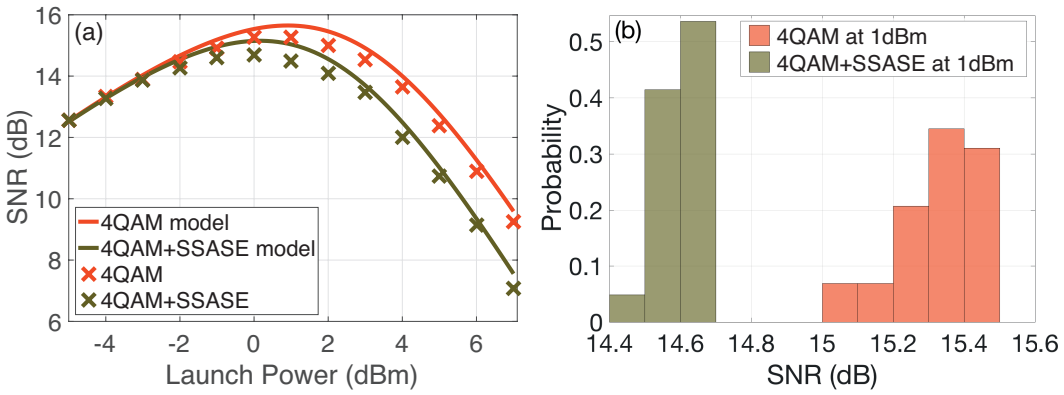

Figure 3.15: a) SNR as a function of launch power for just channel interferers and 1 channel with SS-ASE taken at 2028 km. Crosses are experimental points and solid lines are the model b) Histogram of SNR of the CUT over time for channel interferers and SS-ASE for 4QAM at a fixed launch power of 1 dBm.

From Fig. 3.15 (a), it can be seen that the predicted SNR of the model agrees with the experimental data to within 0.5 dB. It can also be seen that when the bandwidth was loaded with SS-ASE, the peak SNR is lower and hence the NLI is higher compared to that of channel interferers. To quantify the effects of the additional NLI from SS-ASE, the optimum experimental SNR for both schemes was found. The peak SNR was

estimated by fitting a third order polynomial to the data using a least square error (LSE) approach and taking the maximum of that polynomial.

For 4QAM channel interferers the maximum SNR was 15.19±0.10 dB and for SS-ASE 14.62±0.13 dB with corresponding optimum launch powers of -0.2 dBm and 0.8 dBm. The confidence interval of 50% is calculated from the errors between the data and the assumed cubic polynomial. The change in peak SNR between the two cases is 0.57±0.16 dB and was predicted to be 0.50 dB by the model. In order to be sure of this change in SNR the launch power was fixed at 1 dBm and multiple readings were taken for both interferer schemes over time and plotted in a histogram as shown in Fig. 3.15 (b). This is 0.2 dBm higher than optimum launch power for the 4QAM CUT with 4QAM interferers and 1.2 dB higher than optimum for SS-ASE. At this launch power the delta in SNR between the two bandwidth loading schemes is larger so is more reliable experimentally. 50 samples were taken for each scheme. From Fig. 3.15 (b) it can be seen that the penalty in SNR (difference in mean) is 0.72 dB with a standard deviation of σ=0.13 dB. The used model predicted a penalty of 0.61 dB. This agreement within error between experiment and model shows that the use of SS-ASE as a replacement for channel interferers gives a pessimistic evaluation of performance in the nonlinear regime.

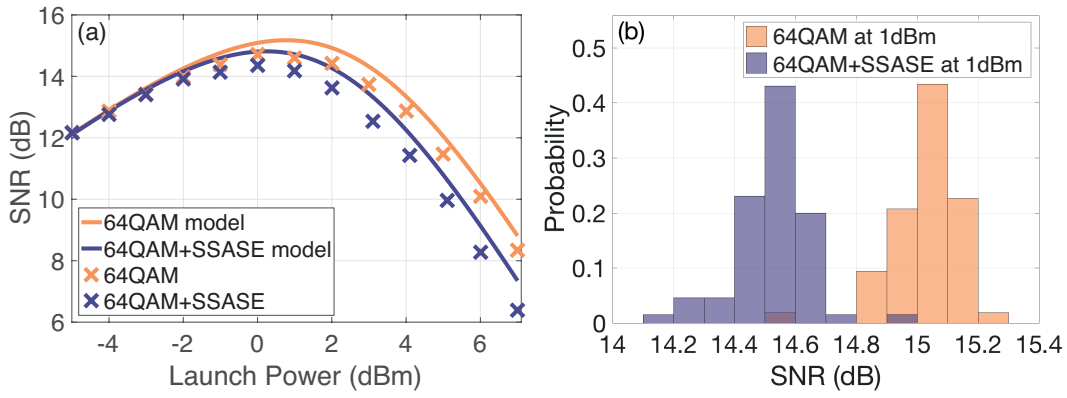

Figure 3.16: a) SNR as a function of launch power for just channel interferers and 1 channel with SS-ASE taken at 2028 km. b) Histogram of SNR of the CUT over time for channel interferers and SS-ASE for 64QAM at a fixed launch power of 1 dBm.

The results of the power sweep for 64QAM with both schemes of interfering channels are shown in Fig. 3.16. The difference in peak SNR from 64QAM to SS-ASE is 0.40 dB. The SNR of the CUT was again taken over time for both schemes at a fixed launch power of 1 dBm per channel. Again, 50 samples were taken for each scheme. The resulting offset in mean SNR was 0.49 dB with a standard deviation of σ=0.11 dB. The difference in SNR at optimum launch power and in the nonlinear regime is smaller than that of 4QAM and agrees with the predictions from the model of 0.37 dB at optimum and 0.44 dB at 1 dBm.

This corroborates with the fact that the modulation format of the interfering channel

affects the amount of nonlinear interference noise on the CUT [23, 37]. Here SS-ASE can be thought of as the same as a Gaussian modulation format. This format has an excess kurtosis of 0, which is greater than the values of -1 and -0.62 for 4QAM and 64QAM channels respectively.

3.3.6 Distance investigation

This subsection investigates the system performance in terms of achievable rate as a function of distance when replacing channel interferers with SS-ASE. The MI of the CUT was measured as a function of distance (100 km to 2500 km) and is shown in Fig. 3.17. A fixed launch power of 2 dBm per channel was chosen in order to more clearly show the difference in performance between interfering schemes. As can be seen at shorter distances the MI drops slowly and up to 300 km, the SS-ASE and channel interferers have the same performance. At shorter distances, the transceiver SNR_{TR} (which determines the highest MI in the system) is the predominant source of noise in the system. For longer distances, the effect of SNR_{TR} becomes less significant, and the system performance is dominated by accumulation of ASE and by NLI. For instance, at 2000 km the channel interferers outperformed the SS-ASE by 0.43 b/sym. It can also be observed, the difference between the model and experimental results increases as the distance increases. This is due to the WSS being reprogrammed for each number of recirculations to maintain spectral flatness. The additional NLI incurred from the SS-ASE can be seen to affect the performance significantly beyond 800 km. This is the regime in which NLI noise forms a significant contribution of the total noise compared to the transceiver noise. Hence, the launch power curves in Fig. 3.16 & 3.15, were taken at 2000 km to demonstrate the NLI away from the effect of transceiver noise limits.

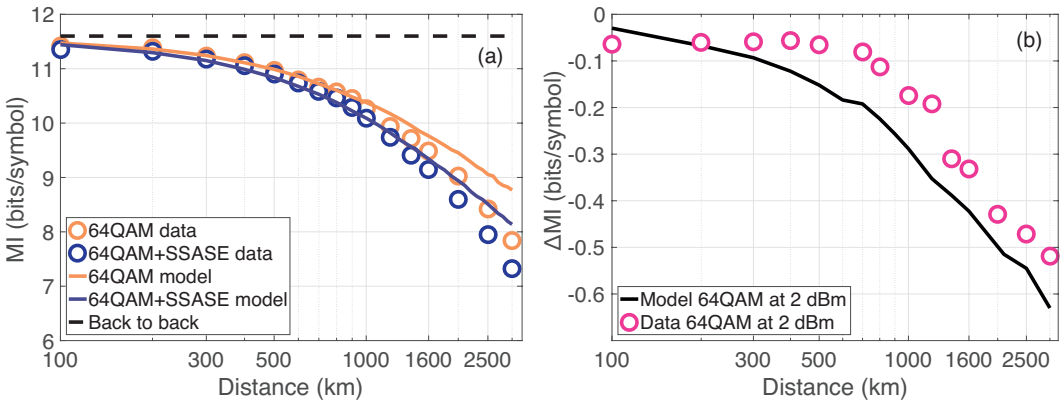

Figure 3.17: Mutual information (MI) measured as a function of distance for channel interferers and SS-ASE schemes. Markers are experimental points taken at a fixed launch power and lines are from the model. (a) channel interferers (orange) and SS-ASE (purple). (b) shows the difference in MI between channel interferers and SS-ASE as a function of distance

The change in MI from both interfering schemes as a function of distance is shown in Fig. 3.17 (b). The discontinuous nature that can be seen in the model results is due to errors in the Monte-Carlo integration used to calculate η in equation 3.7. Once the transceiver noise becomes small relative to the NLI, the difference in MI seen to increase. In the case of this experiment is beyond 700 km. The crossing of the theory and data is due to experimental inaccuracies as shown in Fig. 3.15 & 3.16, where the standard deviation of each point was of the order of 0.1 dB, by propagating the error accordingly the standard deviation in ΔMI is 0.07 bits/sym.

The measured offset from channel interferers and SS-ASE in SNR is 0.8 dB at 2000 km, corresponding to a change in MI of 0.4 bits/sym which is 5% of the achievable rate. The penalty after 800 km of transmission corresponds to a decrease in MI of 0.07 bits/sym, a change in capacity of 0.6%. The difference in SNR at optimum launch power is smaller than that shown at 2 dBm, so the measured ΔMI in Fig. 3.17 (b) is larger than would be expected at optimum launch power. This means when evaluating SNR at short distances with optimum launch power, close to where transceiver noise is dominant, using SS-ASE as an interfering channel is a very reliable estimate of performance as the penalty is less than 0.6%. The difference in SNR and MI between channel interferers and SS-ASE, is noted to always be negative, so the SS-ASE will always give a pessimistic prediction of the impact of NLI on system performance.

3.3.7 Bandwidth investigation

In order to investigate the implications of using SS-ASE as a replacement of channel interferers beyond the experimental transmission bandwidth of this work, we extended the study of system performance for bandwidths up to 4.5 THz using the theoretical model. The system under consideration has a fixed transmission distance of 2000 km and 40 GBd modulated channels carrying dual polarisation 64QAM. Fig. 3.18 shows the difference in SNR at optimum signal launch power between the use of channel interferers, and SS-ASE as a function of total transmission bandwidth. Each line represents a different number of channel interferers (adjacent to the CUT) out of the total transmission bandwidth. It can be seen that as the total transmission bandwidth increases, a larger penalty in SNR is observed when SS-ASE is used instead of channel interferers. This is due to the logarithmic growth of the nonlinear distortions as a function of bandwidth, as seen in [95, 115]. It is noted that when a single modulated channel is propagated with SS-ASE to fill the full C-band, a penalty of 0.8 dB is observed. However, if seven modulated channels are propagated together with SS-ASE this penalty is reduced to 0.6 dB. The use of a higher number of channel interferers before employing SS-ASE decreases the penalty from nonlinear distortions. This is because the higher NLI generating SS-ASE is spectrally further away from the CUT. This shows

that using SS-ASE to load the fibre will provide a useful estimate of performance. In the worst case for this system of a fully loaded C-band, the replacement of all channel interferers with SS-ASE only gives a penalty of 0.8 dB.

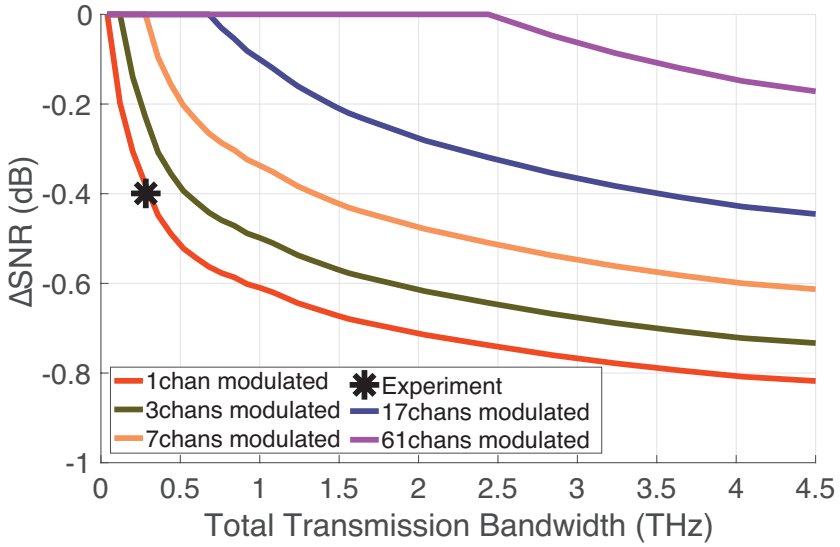

Figure 3.18: Difference in peak SNR between channel interferers and SS-ASE as a function of bandwidth for different number of channel interferers at optimum launch power. For a transceiver with a maximum SNR of 20.1 dB at 2000 km. The marker is the experimental work conducted.

Fig. 3.19 shows another perspective on the difference in SNR between the use of channel interferers and SS-ASE. The delta is shown as a function of the number of emulated channels. This means each of the curves now starts from the origin, when there are no emulated channels. From this plot it can be seen that the more emulated channels are used, the larger the SNR penalty. This shows that the significance of the nature of additional interfering channels drops when further away from the CUT. This is due to the frequency dependance of the NLI. For 1 modulated channel, half of the penalty from adding 60 channels worth of SS-ASE occurs after adding just 6. It is also noted that as more SS-ASE is used the performance continues to drop but does so even slower. These lines asymptotically tend towards being parallel and hence do not converge.

3.4 1 Tb/s superchannel transmission

This section describes work performed in collaboration with Mitsubishi electric research laboratory (MERL). This experiment was a practical implementation of using SS-ASE as a tool to demonstrate performance in the order of Tb/s in a fully spectrally occupied system. Other research has led to several demonstrations of 1 Tb/s optical communications systems utilising a single receiver [76, 85, 105, 108, 111],

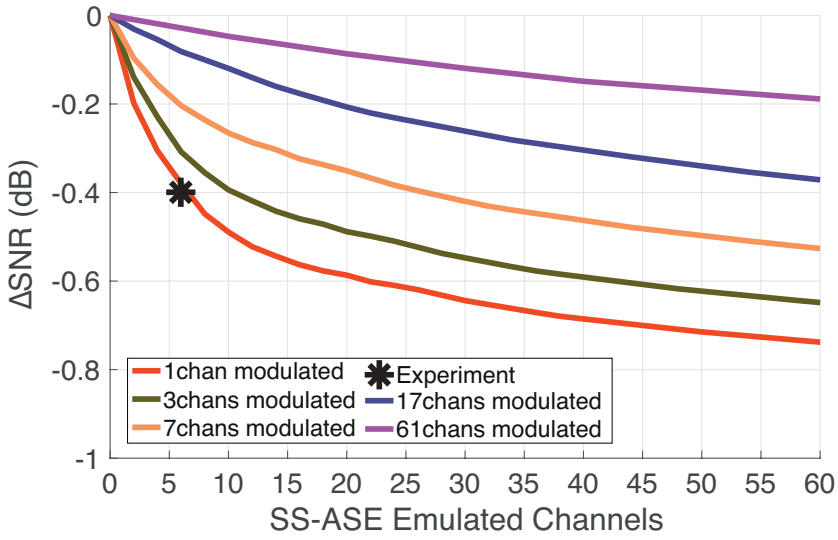

Figure 3.19: Difference in peak SNR between channel interferers and the number of 40 GBd SS-ASE channels for different number of channel interferers at optimum launch power. For a transceiver with a maximum SNR of 20.1 dB at 2000 km. The marker is the experimental work conducted.

typically those demonstrations have relied upon transmitter structures which would prove highly challenging for implementation in commercial products. These transmitter structures have variously used optical frequency combs [76, 85, 111], nonlinear optical processing [108] or custom high-frequency signal converters in InP (Indium Phosphide) [105]. Previous demonstrations of 1Tb/s transceivers have also relied on carrier phase estimation (CPE) algorithms that have high complexity [85, 105, 111], or cannot be implemented in parallel [76].

3.4.1 Experimental setup

This section describes a transceiver which has both optical and electrical transmitter hardware suitable for implementation in commercial systems. A pair of LiNbO3 I/Q modulators were used, similar to those now commercially available in a single package for dual carrier systems, along with a pair of nominal 100 kHz linewidth lasers to generate the optical subcarriers. Conventional DACs in complementary metal oxide semiconductor (CMOS) were used. Two 60 GBd subchannels of dual-polarisation (DP-64QAM) were spaced at 62 GHz, optically multiplexed, and detected with the same receiver as the previous section. This completely utilised the receiver bandwidth. Reduced complexity pilot-aided CPE enabled accurate tracking of carrier phase with only 1.43% pilot symbols. Transmission was demonstrated over 400 km of Corning Vascade EX2000 fibre using 100 km spans.

A schematic of the dual-carrier 60 GBd DP-64QAM transmitter setup is shown in Fig. 3.20. This is the same setup as used in subsection 3.3.2 but here, SS-ASE is

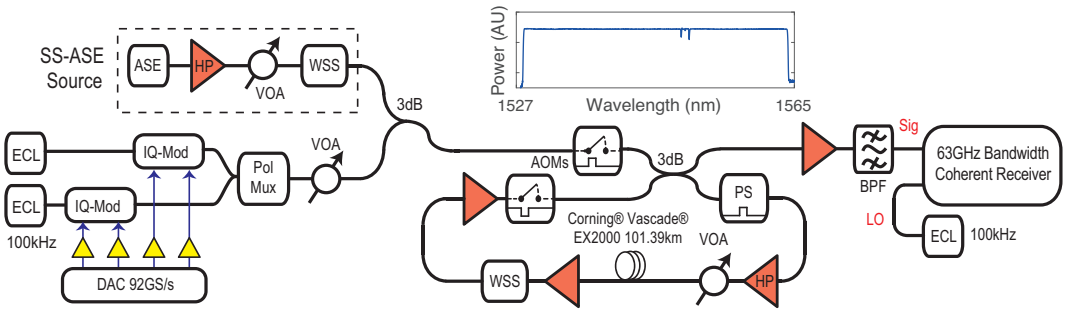

Figure 3.20: Experimental setup used in this work. Inset: spectrum for spectrally shaped ASE.

used to fill the C-band. A digital RRC filter with 0.1% roll-off was used to spectrally shape 64-QAM signals, and linear pre-distortion from section 2.5.1 was applied to compensate for the frequency response of the transmitter components. The modulator has a 3 dB bandwidth of 25 GHz and the roll-off was reasonably slow and it was possible to achieve an SNR ceiling of approximately 16.5 dB with linear pre-distortion (see section 2.5). The signals were transmitted by four synchronised 92 GS/s DACs. The RF signals were then amplified by 30 GHz bandwidth modulator drivers. Two ECL with 100 kHz nominal linewidth and 62 GHz spacing were used as carriers for two independent I/Q modulators. The combined attenuation of the DAC, RF drivers and modulators was approximately 7.3 dB at 30 GHz. The wavelength channels were combined, and polarisation multiplexing emulated with an interferometer with 14.1 ns delay between arms. SS-ASE noise was used as an ultra-broadband source to emulate fully-loaded C-band transmission as investigated in section 3.3.2. The SS-ASE source had a bandwidth of 4.5 THz and a notch centred at 1550 nm with a bandwidth of 140 GHz was carved out to accommodate the channel of interest (see inset Fig. 3.20). A 9 GHz guard-band on each side of the 122 GHz dual-carrier signal was used to minimise linear crosstalk induced penalties [28].

For transmission, a recirculating loop was used, with a loop-synchronous PS, and a single span of 101.39 km of Vascade EX2000 fibre with a total loss of 16.2 dB. This fibre has both extremely low loss, and a silica core with large effective area. The span was followed by an EDFA with 18 dBm output power and 5 dB noise figure to overcome fibre attenuation. A WSS was used as a dynamic gain flattening filter to compensate gain tilt from the optical amplifiers, followed by another EDFA in order to overcome loop component losses. A third ECL with 16 dBm output power and 100 kHz nominal linewidth was used as local oscillator in the optical receiver. Detection was carried out by balanced photodetectors with 70 GHz electrical bandwidth and without trans-impedance amplifiers. Finally, the received signals were captured by a real-time digital oscilloscope with an analogue electrical bandwidth of 63 GHz at 160 GSa/s.

3.4.2 Receiver digital signal processing

The DSP chain for this subsection is unique for this work and was completed in its entitreity by MERL colleagues. It is included here for completeness.

The receiver DSP was of a similar structure to that described in previous work [85], albeit with significantly lower CPE complexity. After normalisation, the signal underwent frequency domain equalisation of chromatic dispersion. Coarse adaptive equalisation was performed, and a 4^{th} power algorithm was used to calculate the subchannel intradyne frequency offsets. The signal was then digitally down-converted and low pass filtered with a matched RRC filter to separate each of the constituent subchannels. The receiver was first operated in training mode, to ensure accurate initial convergence of the adaptive equalisers, and to enable calculation of the set of centroids and SNR of each polarisation subchannel.

Training mode: A pair of trained dual-polarisation radius-directed equalisers (DP-RDE) were used to demultiplex the training sequence polarisation and compensate for filtering effects. The least mean squares (LMS) update algorithm was used, with 151 taps in each of the four constituent FIR filters. Following this, carrier phase was corrected with a trained, feed-forward phase estimator. The training signal with corrected phase was then used to calculate the set of symbol centroids, and SNR for each of the polarisation subchannels.

Pilot-aided mode: After initial training, the receiver was switched to pilot-aided operation. A single dual-polarisation pilot occurred every 71 symbols, corresponding to a pilot overhead of 1.43%. A pair of pilot-aided DP-RDEs with LMS updating were used to equalise the signals, with the taps initialised by the training sequence. Pilot-aided carrier phase estimation was then performed on each polarisation subchannel independently. Firstly, the field of seven pilots were averaged, in order to reduce the effect of additive noise on the pilot phase estimation. The averaged pilot sequence was then unwrapped, and interpolated as a piecewise linear function to provide an initial phase estimate. This phase estimate was then used to initialise a reduced complexity Expectation-Maximisation (EM) algorithm [93], considering only four nearest neighbour symbol likelihoods. The EM algorithm employed the symbol constellation centroids and SNRs calculated during the training period. After two iterations of the EM algorithm, the phase was averaged by a 255 tap averaging filter, and applied to the equalised symbols. Bit-wise log-likelihood ratio (LLR)s were then calculated, again according to the symbol constellation centroids and SNRs calculated during the training period.

Forward Error Correction Coding: An inner check-concentrated, triple-variable-degree LDPC code was used, with rate 0.71 and word length of 52,800 bits. The bit LLRs were deinterleaved across all bit positions, polarisations and wavelength

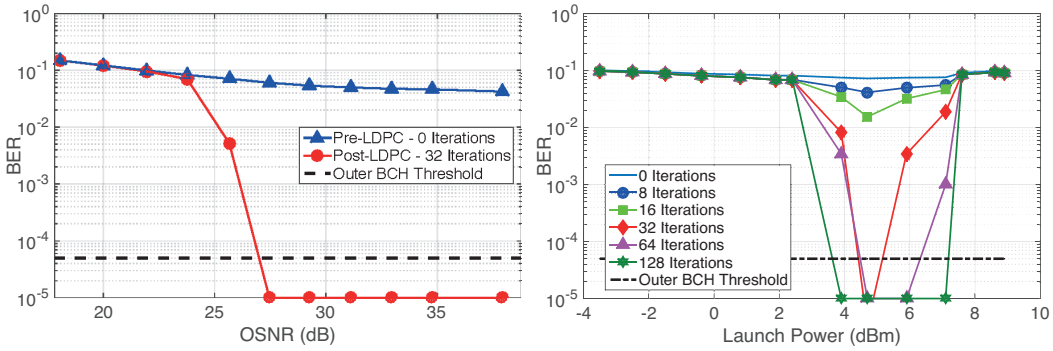

Figure 3.21: Experimental results: (a) BER averaged over both subchannels in back-to-back configuration before and after LDPC decoding. (b) BER performance after transmission over 400 km of Vascade EX2000 fibre with full C-band ASE loading. Note that measurements exhibiting no bit errors after LDPC decoding over 3×10^6 bits per measurement are rounded up to a BER of 10^{-5}

subchannels to ensure optimal performance. The decoder used the sum-product algorithm, with flooding decoder scheduling. The use of an outer hard-decision Bose-Chaudhuri-Hocquenghem (BCH) code with rate 0.9922 was assumed, which decodes an input BER of 5×10^{-5} to an output BER of 10^{-15} or better [85]. We therefore assume that a post LDPC BER of 5×10^{-5} can be decoded to a BER of 10^{-15} or better after the BCH decoder, which was not implemented.

3.4.3 Experimental demonstration

BER performance before and after LDPC decoding was characterised with an ASE noise loading setup in back-to-back configuration, then with transmission over 400 km of Vascade EX2000 fibre with full C-band SS-ASE loading. The results of the back-to-back characterisation are shown in Fig. 3.21 (a). We show total average BER before and after 32 iterations of the LDPC decoder. Note that the OSNR required for operation at a BER of 10^{-15} or better is approximately 27 dB. A measurement taken with an OSNR of 25.7 dB has a pre-LDPC decoding BER of 7×10^{-2},which is improved to a BER of 5×10^{-3} after 32 iterations of the LDPC decoder. The next measurement had an OSNR of 27.5 dB, and no errors after 32 iterations over the approximately 3×10^6 bits detected in a single capture. The results after transmission over 400 km are shown in Fig. 3.21 (b). We show BER before decoding, and then after 8, 16, 32, 64 and 128 iterations of the LDPC decoder. We note that while a single measurement was below the outer code threshold after 32 decoder iterations, increasing the number of iterations increased the launch power margin. The system had approximately 4 dB of launch power margin after 128 decoder iterations, with post-LDPC BER better than 5×10^{-5} , achievable between approximately 3 dBm and 7 dBm launch power.

3.5 Summary

The use of SS-ASE loading in the design and evaluation of wideband (up to a full C-band) optical fibre transmission systems was investigated in detail for the first time. It was shown that SS-ASE generates additional nonlinear interference noise, compared to that of conventional channel based interferers. The described model in section 3.3.3 treats SS-ASE as Gaussian modulation, which gives an accurate method to predict performance. The NLI from SS-ASE is larger than that from 64QAM interferers, and even larger than 4QAM interferers. The increase in NLI noise reduces the SNR and hence SS-ASE always gives an underestimate. There is good agreement between the model and experimental results which highlight that the conservative or pessimistic estimate of SS-ASE as an interferer scheme, is the same as the underestimate that comes from using the GN model. The reduction of MI was calculated to understand the effect of SS-ASE in systems that use coded modulation. It was shown that the change in MI at the optimum launch power for this scheme was 0.6% of the achievable rate at 800 km and 5% at 2000 km and the measurements confirmed that using SS-ASE as a method of loading a fibre results in greater NLI. The greater the number of channel interferers used before SS-ASE is employed, the smaller the penalty. For the studied experimental configuration using SS-ASE to load 4.5 THz of bandwidth with one modulated channel only gives a reduction of 0.8 dB in SNR. If a total of 17 modulated channels (representing 15% of the total 4.5 THz) are used, the SNR is reduced by only 0.42 dB, making SS-ASE an invaluable tool for the design and verification of fully loaded, wideband transmission systems.

A simplified 1 Tb/s transceiver was demonstrated in a fully loaded C-band system using SS-ASE, by utilising a dual-carrier transmitter and a single coherent optical receiver. The transmitter was implemented with commercially available components, including a CMOS DAC, a pair of lithium niobate ($LiNbO_3$) modulators and a pair of free running lasers. Digital pre-distortion was used at the transmitter to extend the bandwidth of the modulator, RF drivers and DAC. At the receiver, training sequences were used to ensure accurate equaliser convergence, and provide signal and noise statistics for both CPE and LDPC decoder. Low complexity, pilot-aided CPE was used with a 1.43% pilot insertion ratio, exploiting the statistics of the signal and channel. A concatenated LDPC and BCH FEC scheme was proposed, with the LDPC implemented in offline post- processing. Combined, these schemes enabled the first transmission of a dual-carrier 1 Tb/s signal using components similar to those immediately available for commercial implementation.

The use of SS-ASE to load an optical transmission system enables vendors and researchers to use this technique to set a lower bound and give a performance margin in order to improve reliability. Research both within UCL and outside is now being con-

ducted using this technique. Published papers that use this technique include: 7.3 THz Transmission in Journal of Lightwave Technology at UCL in [115], paper presented in the previous section [86] published at European conference on optical communication (ECOC), followed up in the Journal of Lightwave Technology [63], Facebook Optical Fibre Communications Conference (OFC) C-band transmission post-deadline paper [148], a paper by TESubcom at OFC looking at the validity of using odd-even channel decorrelation schemes [12] and a post-deadline paper at OFC by Nokia Bell Labs used SS-ASE to show transmission over 100 nm amplifier [106].

4

Mitigation of Nonlinear Interactions

NONLINEAR interactions stemming from the Kerr effect mean that the achievable information rates of optical communications systems are affected by the signal power. The nonlinear interaction and associated phase shift can manifest as constructive and destructive interference, this is capitalised upon in certain applications outside of telecoms such as parametric amplification and frequency broadening [134]. Characterising these interactions is important, in order to understand what limits transmission rates. The origin is well understood but its implications in the context of telecommunications are still under investigation.

Mitigation of nonlinearity can only be performed once the physics of signal propagation through an optical fibre is understood and the effects are fully characterised. The nonlinear interference is inherently deterministic but is very complicated to describe accurately and hence in the GN and EGN model is treated as noise [15, 96, 97]. If nonlinear interference is treated as stochastic noise then, by definition, it cannot be compensated. By understanding the statistics of the NLI it can be shown that it is not truly random, and hence, it is not noise and so, can be compensated. In this chapter a method of characterising the amount and nature of nonlinear interference is demonstrated in theory and performed upon experimental traces.

High-speed, WDM systems are often limited by nonlinear interactions between different WDM channels. Interactions arising from channels outside the bandwidth of each individual WDM receiver, appear random and are registered as noise. From here on this noise will be referred to as nonlinear interference (NLI).

Extensive efforts have been invested into the characterisation of NLI statistics, to explore the extent to which it is really random, and to devise possible methods for its mitigation. An important finding was that the cross-phase modulation (XPM) component of NLI (the predominant component in most practical scenarios of high channel count systems operating at a symbol rate higher than 10 GBd in each channel) can be modelled very accurately as an ISI process with random and time varying ISI coefficients [25, 45, 126]. Hence, the characterisation of NLI can be translated into the characterisation of the corresponding ISI coefficients. Devising reliable experimental approaches for doing that is imperative for assessing the prospects of NLI mitigation techniques [48, 127, 146, 151].

Almost all existing research to date has considered only the zeroth-order ISI coefficient, whose contribution to NLI is as phase and polarisation rotation noise (PPRN) [35, 94, 125]. Yet, in most cases of interest, it is also important to account for higher order ISI terms, whose accumulated effect may exceed the PPRN contribution. One of the obstacles to doing so is the difficulty in evaluating the higher order ISI terms experimentally. When one performs a transmission experiment the contribution of all ISI orders is intertwined, and they must be separated in order to be measured properly. The zeroth-order ISI term produces distinctively distorted, 'kidney-shaped', clouds in the received constellation, which makes its identification relatively simple. In contrast, the effect of higher order ISI terms is not geometrically obvious, and can be easily confused with additive white noise.

4.1 Characterisation of nonlinear interference (NLI)

A method for measuring any-order ISI coefficients and evaluating their correlation properties is presented. We demonstrate the accuracy of the method in several settings by comparing experimental results to numerical simulations. Our findings confirm the importance of the high-order ISI contributions to NLI. Knowledge of the correlation properties of the ISI coefficients can be exploited for designing novel methods for NLI mitigation. For example, in ref. [48] a detailed model of the correlations of NLI was used to obtain a maximum likelihood equaliser, which improved the bit error rate of the simulated transmission system.

Consider a WDM system, in which a CUT propagates in the fibre along with many interfering channels (IC)s. At the receiver, the signal is filtered, sampled, and dispersion compensated. It has been shown that under these conditions the nonlinear interference noise is accurately represented by the time-varying ISI model detailed in [45, 46]. According to this model, the relation between the received and transmitted

signal samples is

$$\underline{s}_n = \underline{a}_n + i\sum_l \mathbf{R}_l^{(n)} \underline{a}_{n-l} + \underline{w}_n, \tag{4.1}$$

where the underlined variables represent two element column vectors and the boldface variables $\mathbf{R}_l^{(n)}$ are 2×2 ISI matrices. The elements of $\underline{s}_n$ are the n-th samples of the received signal in the two polarisations, the elements of $\underline{a}_n$ are the two polarisation symbols launched in the n-th time-slot, and the elements of $\underline{w}_n$ are statistically independent complex circular Gaussian random variables that account for the contribution of ASE noise. The nonlinear interference from the ICs is represented by the ISI matrices $\mathbf{R}_l^{(n)}$, whose elements are determined by the data transmitted in the ICs [45]. The subscript index l is the ISI order, and the superscript n accounts for the slow (on the scale of a symbol duration) dependence of the ISI matrix on time. The effect of nonlinear phase noise, whose measurement in experiments was addressed in [94], is entirely captured by the the trace of the zeroth-order ISI matrix $\mathbf{R}_0^{(n)}$.

We now describe the procedure that allows extraction of the second-order statistics of the ISI matrices $\mathbf{R}_l^{(n)}$ experimentally. For simplicity, the starting point is the operation in the scalar case, i.e. when $\underline{s}_n, \underline{a}_n, \mathbf{R}_l^{(n)}$, and $\underline{w}_n$ are treated as scalars. The more general results that correspond to the polarisation multiplexed case follow.

The scalar version of Eq. (4.1) assumes the form,

$$\begin{aligned} s_n &= a_n\left(1+iR_0^{(n)}\right) + i\textstyle\sum_{l\neq 0} R_l^{(n)} a_{n-l} + w_n \\ &\simeq a_n e^{iR_0^{(n)}} + i\textstyle\sum_{l\neq 0} R_l^{(n)} a_{n-l} + w_n, \end{aligned}$$

where the transition from the first to the second line is valid within the first-order perturbation analysis that underpins the entire theoretical framework of NLI analysis [26]. The fact that $R_0^{(n)}$ is real-valued [24] indicates that its only effect is to produce phase noise, whose statistics can be readily extracted from the received constellation diagram [94]. All other ISI terms in (4.2) are uncorrelated with a_n, and therefore, in a constellation diagram, they appear as circular white noise, which is indistinguishable from the contribution of ASE. In what follows we demonstrate a technique that allows measurement of the second-order statistics of $R_l^{(n)}$ for all values of l. We stress that our goal is to assess the second-order statistics of the ISI terms experimentally, and not to measure their instantaneous values.

In a transmission experiment setup one measures the noisy samples, s_n. For the purpose of estimating the statistics of $R_l^{(n)}$, we assume that the data symbols transmitted on the CUT are known. We also assume that the transmitted constellation is symmetric (so that the mean of a_n is 0) and that it does not include the origin (i.e. all $a_n \neq 0$). These last two assumptions are not necessary, but they significantly simplify the derivation.

Under these conditions, we define the quantity,

$$\tilde{R}_l^{(n)} = \frac{s_n - a_n}{i a_{n-l}} = R_l^{(n)} + V_l^{(n)}, \tag{4.2}$$

which serves as an estimate for $R_l^{(n)}$. The term $V_l^{(n)}$ represents the estimation error, and it is given by,

$$V_l^{(n)} = \frac{1}{a_{n-l}} \left[\sum_{l' \neq l} R_{l'}^{(n)} a_{n-l'} - i w_n \right]. \tag{4.3}$$

As the data symbol a_{n-l} is independent of any of the elements in the brackets, it follows that $V_l^{(n)}$ is a white process. The ACF of $\tilde{R}_l^{(n)}$ may therefore be expressed as,

$$\begin{aligned} f_{\tilde{R}_l}(\Delta n) &= \lim_{N \to \infty} \frac{1}{N} \sum_{n=1}^{N} \tilde{R}_l^{(n)} \tilde{R}_l^{*(n+\Delta n)} \\ &= f_{R_l}(\Delta n) + \mathrm{Var}\left[V_l^{(n)} \right] \delta(\Delta n), \end{aligned}$$

where $\delta(\Delta n)$ is the Kronecker symbol. The measured ACF is therefore identical to that of R_l, with the exception of the point $\Delta n = 0$, which corresponds to the variance. The cross-correlation function between different ISI elements can also be measured using the same method.

The existence of the delta-correlated term was observed in the past by several researchers who attempted to measure the correlation properties of NLI-induced phase noise [94], and it hinders the direct measurement of the ISI coefficients' variance. This obstacle is easily circumvented by making use of the fact that the ISI matrices $R_l^{(n)}$ are characterised by a moving average model and therefore their ACF $f_{R_l}(\Delta n)$ is smooth. Hence, the value at $\Delta n = 0$ may be obtained from the rest of the ACF ($\Delta n > 0$) via interpolation.

The generalisation to the dual-polarisation case is fairly straightforward. This time we use the estimate,

$$\tilde{\mathbf{R}}_l^{(n)} = -i(\underline{s}_n - \underline{a}_n)\underline{b}_{n-l}^T = \mathbf{R}_l^{(n)} + \mathbf{V}_l^{(n)} \tag{4.4}$$

where $\underline{b}_n$ is defined as

$$\underline{b}_n = \begin{pmatrix} a_{x,n}^{-1} \\ a_{y,n}^{-1} \end{pmatrix}, \tag{4.5}$$

with $a_{x,n}$ and $a_{y,n}$ denoting the two polarisation elements of $\underline{a}_n$, and the estimation noise matrix $\mathbf{V}_l^{(n)}$ is given by,

$$\mathbf{V}_l^{(n)} = \sum_{l' \neq l} \mathbf{R}_{l'}^{(n)} \underline{a}_{n-l'} b_n^T + \mathbf{R}_l^{(n)} \begin{pmatrix} 0 & \frac{a_{x,n}}{a_{y,n}} \\ \frac{a_{y,n}}{a_{x,n}} & 0 \end{pmatrix} - i \underline{w}_n \underline{b}_n^T. \tag{4.6}$$

Similarly to the scalar case, all elements of $\mathbf{V}_l^{(n)}$ are white processes, and therefore the ACF of the i,j-th element of $\tilde{\mathbf{R}}_l^{(n)}$ is given by,

$$\begin{aligned} f_{\tilde{R}_{l,ij}}(\Delta n) &= \lim_{N\to\infty} \frac{1}{N} \sum_{n=1}^{N} \tilde{R}_{l,ij}^{(n)} \tilde{R}_{l,ij}^{*(n+\Delta n)} \\ &= f_{R_{l,ij}}(\Delta n) + \mathrm{Var}\left[V_{l,ij}^{(n)}\right] \delta(\Delta n), \end{aligned}$$

where $i,j \in [x,y]$.

4.2 Experimental setup and results

In the experiments the drive signals were generated from sequences of 2^{16} random bits mapped to 64 QAM symbols and nonlinearly pre-emphasised using a Volterra filter to compensate for transmitter nonlinearity [7], as described in Section 2.5.2. The symbol rate was set to 40 GBaud and a RRC filter with 0.001 rolloff was applied. The signals were uploaded to a 92 GSa/s DAC, linearly amplified and applied to 2 separate IQ modulators that were used to independently modulate odd and even WDM channels, which were decorrelated with a 15 ns delay and polarisation multiplexed. The channel spacing was set to 42.5 GHz and the number of WDM channels was changed between 1 and 15. The nominal linewidth was 1.1 kHz for the central channel and 100 kHz for the other channels. In all cases, the central channel was used as the CUT.

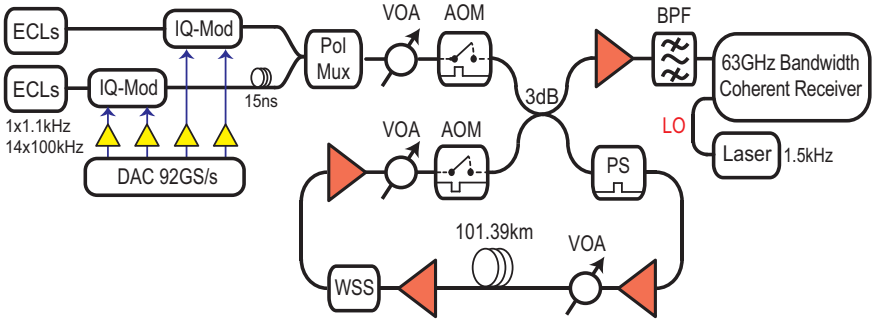

Figure 4.1: Experimental setup

For transmission, a recirculating loop was used as shown in Fig. 4.1, with a loop-synchronous polarisation scrambler and a 101.39 km span of fibre with a total loss of 16.2 dB, with a dispersion of 20.2 ps/(nm·km) and γ of 1.2 $(\mathrm{W{\cdot}km})^{-1}$. Two EDFAs (5 dB noise figure) separated by a WSS (serving as a programmable gain flattening filter) were also present inside the loop. The number of times that the signal circulated through the loop was controlled to determine the transmission distance. A single span enabled fine control over transmission distance. The coherent receiver used an ECL with 12 dBm output power and 1.5 kHz nominal linewidth, and balanced photodiode

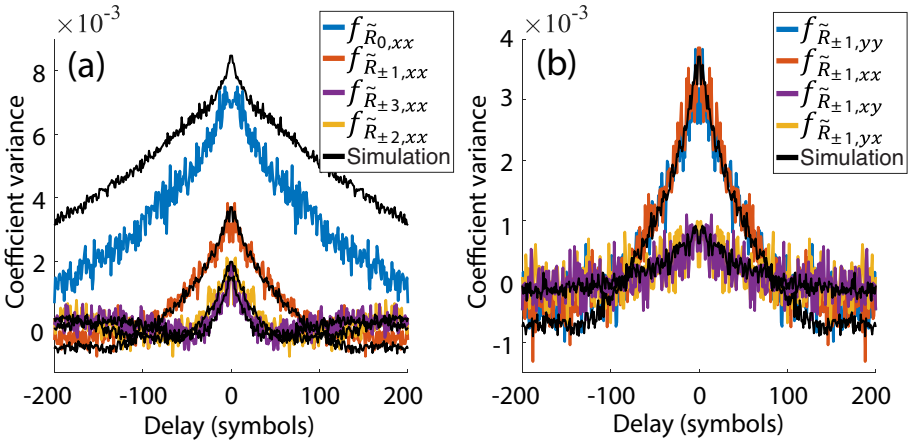

Figure 4.2: Measured auto-correlation functions for various ISI coefficients. (a) Shows the ACFs for the diagonal ISI elements, $R_{l,xx}$, for ISI orders $l = 0, \pm 1, \pm 2, \pm 3$. (b) shows the ACFs of the four elements of the ISI matrices $\mathbf{R}_{\pm 1}$. Coloured curves correspond to experimental results, while black curves to split-step simulations. In all cases, the delta-correlated term $\mathrm{Var}\left[V_{l,ij}^{(n)}\right]\delta(\Delta n)$ was artificially removed, as to produce a clear figure.

detectors. The received signals were sampled by a real-time digital oscilloscope with an analogue electrical bandwidth of 63 GHz at 160 GSa/s.

The offline digital processing of the traces followed the process described in Appendix B. The constant modulus algorithm (CMA) was preconverged 61 taps for the LMS radially directed equaliser (RDE), with the carrier phase estimator using 256 taps. The experimental results are supplemented by split-step simulations which were performed using the same link parameters specified above. In contrast to the experimental setup, the simulations do not include the effects of ASE, laser phase noise, and the receiver's DSP. Thus, they are used to ascertain that the observed correlations are indeed due to NLI and not any receiver issues. The number of symbols used in each simulation was 2^{13}, and 50 independent runs were performed for each configuration, as to obtain smooth results.

Fig. 4.2 shows several examples of the ISI coefficients' auto-correlation functions, for the case of a 20×100 km link, carrying 7 WDM channels with 2.5 dBm launch power per channel. Fig. 4.2 (a) shows the ACFs of the xx diagonal elements of seven ISI matrices, corresponding to $l = 0, \pm 1, \pm 2, \pm 3$ for the experimental measurements and all the simulations. Due to the presence of ASE noise, the ACFs of higher-order ISI coefficients could not be adequately resolved in the resolution of the figure. Note that elements that correspond to the same $|l|$ (e.g. $R_{1,xx}$ and $R_{-1,xx}$) have the same auto-correlation properties, although the values of the coefficients themselves at any given moment are different. It can be seen that all of the coefficients are characterised by correlation times of the order of tens of symbols. Fig. 4.2 (b) shows the four elements of the ± 1 ISI matrices, $\mathbf{R}_{\pm 1}$. As can be expected from symmetry, the ACFs of the two diagonal terms are identical, as are the ACFs of the two off-diagonal terms. In addi-

tion, the diagonal elements are considerably stronger than the off-diagonal elements, although the ratio between them depends on the transmission parameters (e.g. the variance of the diagonal elements depends on the modulation format, whereas that of the off-diagonal elements does not [45]). In all cases except $l = 0$, the agreement between the measured and simulated results is excellent. The discrepancy in the case of $l = 0$ is likely to be due to the laser phase noise and the phase recovery algorithm that was used in the case of the experimental data. Attempts to include the same algorithm in the simulation failed to produce consistent results as the DSP reacts differently to each realisation of noise.

The actual ACFs from the noisy measurements by fitting the positive side of the measured ACFs ($\Delta n > 0$) to a 5^{th} order polynomial function. The variance was estimated to be the fitted function's value at $\Delta n = 0$, whereas we define the correlation time as the point where the correlation drops to e^{-1} of its peak. Fig. 4.3 shows the dependence of the ISI coefficients' variance and correlation time on the launch-power, the length of the system, and the number of interfering WDM channels. As expected from the results presented in [45], the variance of the ISI coefficients is proportional to the square of the launch power, but the correlation time remains independent of power. It can be seen that both the variance and correlation time of all coefficients increase with the link's length, as shown in Figs. 4.3 (c) and 4.3 (d). The growth in variance is simply due to the accumulation of larger nonlinearity, whereas the growth in the correlation time is attributed to the larger overall walk-off between the channels. The gradual growth of the variance with the number of WDM channels in Fig. 4.3 (f) is consistent with the fact that the total NLI increases when more ICs are added into the system. As expected, the growth of NLI is seen to be more pronounced in the behavior of $\mathbf{R}_0^{(n)}$, which accounts for PPRN. This is caused by the fact that the added WDM channels are spectrally farther from the CUT, in which case their nonlinear interaction with it is characterised by a larger fraction of complete collisions [27]. Yet, the weak dependence of the correlation time on the number of channels seen in Fig. 4.3 (e), is somewhat surprising in view of the increasingly fast walk-off that characterises the interaction with each additional IC that is added into the system. Notice that while in cases where $l \neq 0$ the experimental results are generally in good agreement with the simulations, the case of $l = 0$ is characterised by various irregularities. Most obvious of which is the non-physical variations of the correlation time of $R_{0,xx}$ with the launch power in Fig. 4.3 (a) and with the number of WDM channels in Fig. 4.3 (e). As noted earlier, this phenomenon is likely due to the effects of laser phase noise and to the stability of the phase-recovery algorithm, which seems to produce different results at different operating points. Attempts to reproduce this behavior in simulations were unsuccessful.

In Fig. 4.4 we demonstrate the use of the proposed technique for evaluating the

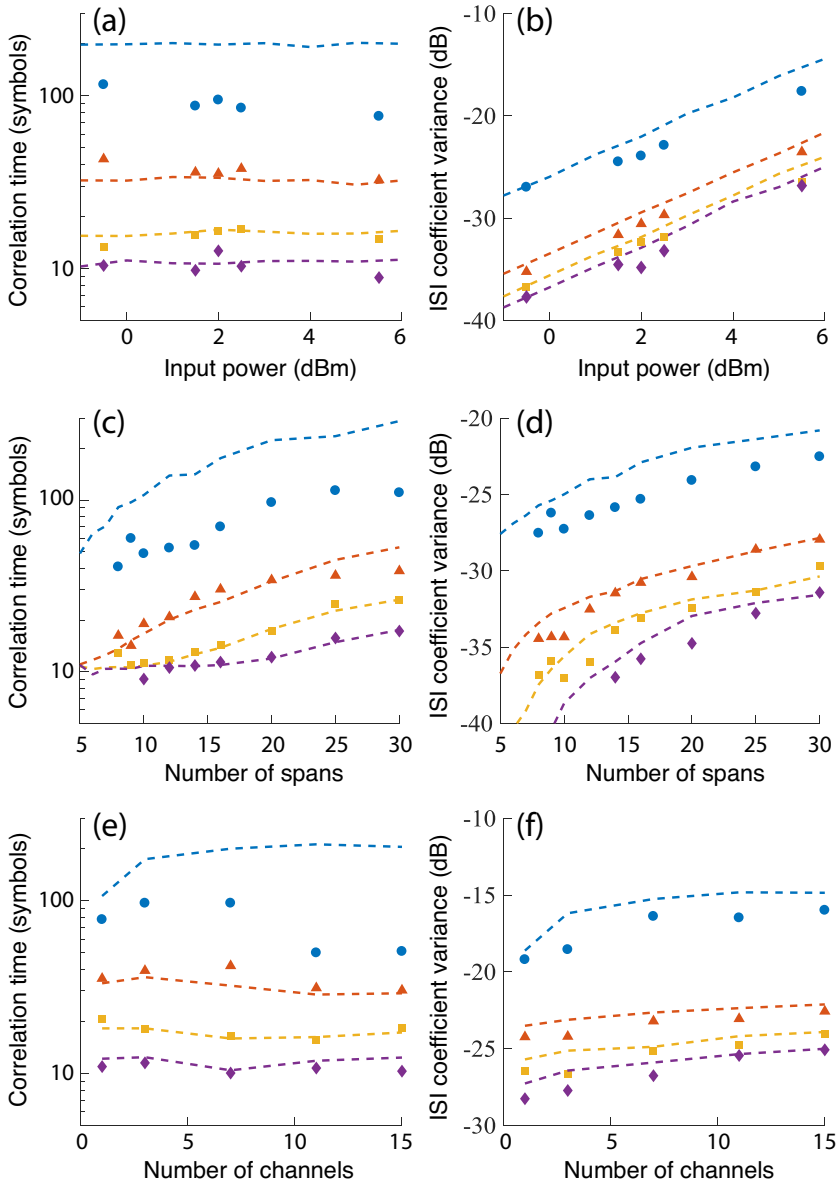

Figure 4.3: Correlation time (left column) and variance (right column) as a function of power (a,b), system length (c,d), and number of WDM channels (e,f). In all cases the CUT is at the centre. The figures show $R_{0,xx}$ (blue-dots), $R_{1,xx}$ (red triangles), $R_{2,xx}$ (yellow rectangles), and $R_{3,xx}$ (purple diamonds). Simulations are shown by dashed curves. The number of WDM channels in panels a–d is 7 (3 on each side of the CUT). The power in c–d was 2dBm, and that of e–f was 5.5 dBm. The number of 100 km spans in panels a,b,e, and f, was 20.

cross-correlations between different ISI orders. The correlations between the $l = \pm 1$ ISI orders are considered in Fig. 4.4 (a), whereas Fig. 4.4 (b) focuses on the correlation between ISI orders $l = 0$ and $l = 1$. All curves were obtained only for the xx elements of the involved matrices and normalised to the square root of the product of the corresponding variances, such that the value at zero delay yields Pearson's correlation coefficient. Notice that the cross-correlation functions of the real parts of $R^{(n)}_{xx,\pm 1}$ and of the imaginary parts of $R^{(n)}_{xx,1}$ in Fig. 4.4 (a) peak very close to -1, and 1, respectively.

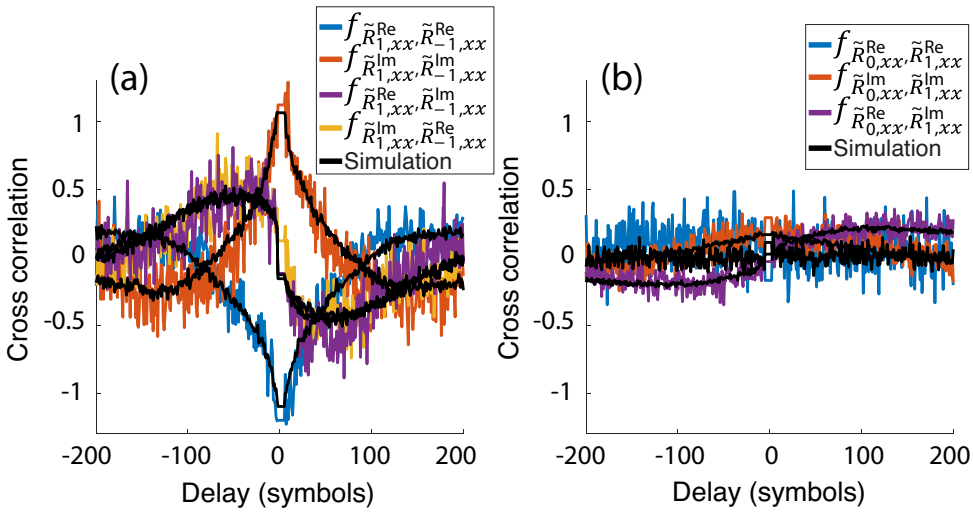

Figure 4.4: Normalised cross-correlation functions of the xx elements of the $l_{1,2} = \pm 1$ ISI matrices (a) and the $l_1 = 0$ and $l_2 = 1$ ISI matrices (b). The functions are plotted separately for combinations of the real and imaginary parts. The coefficients' real and imaginary parts are denoted by $R^{\mathrm{Re}}_{l,xx}$ and $R^{\mathrm{Im}}_{l,xx}$, respectively.

This indicates that $R^{(n)}_{xx,1}$ and $R^{(n)}_{xx,-1}$ are almost exactly the complex conjugates of one another. The fact that the peak absolute value of the experimental curves in Fig. 4.4 (a) is slightly larger than 1 is due to measurement noise. A much weaker correlation characterises the relation between ISI orders $l = 0$ and $l = 1$ shown in Fig. 4.4 (b). In general, the strong correlations exist between coefficients corresponding to ISI orders of opposite sign (such as ± 1, or ± 2 etc.). This correlation is strongest for the $l = \pm 1$ coefficients and reduces gradually as $|l|$ increases. The correlation between all other pairs of coefficients is significantly smaller. This interesting behaviour arises from the particular structure of the ISI matrices (see Eq. (8) in [26], and Eq. (7) in [24]). The nonlinear interaction coefficients of opposite sign pulses are very similar, leading to this result.

The attention of this thesis now focuses on the effectiveness of the nonlinear mitigation technique, DBP. Experiments using straight line and recirculating loop setups are conducted and compared as described in Section 3.1. DBP is then implemented for a transmission system utilising multicore fibre.

4.3 Nonlinearity mitigation in a recirculating loop

The transmission system used in the previous section for investigating NLI correlations, is also used to investigate the use of digital back propagation in a recirculating loop or a straight line. The differences in the recirculating loop for this experiment are as follows, the CUT and LO were from an ECL with 100 kHz linewidth and the transmission distance (11 spans, 1114 km) is chosen to be the furthest that can be directly compared.

Four different cases are investigated. A total of seven channels was sent in all cases. The modulation formats of the channels were changed from 4QAM and 64QAM and the interfering channels changed to SS-ASE just as in Section 3.3.4. The launch power was varied from -5 to 7 dBm per channel and single channel DBP with optimised fibre dispersion parameter D, nonlinear parameter γ and split-step size, was performed for all launch powers and the SNR of the CUT was measured. The results are shown in Fig. 4.5.

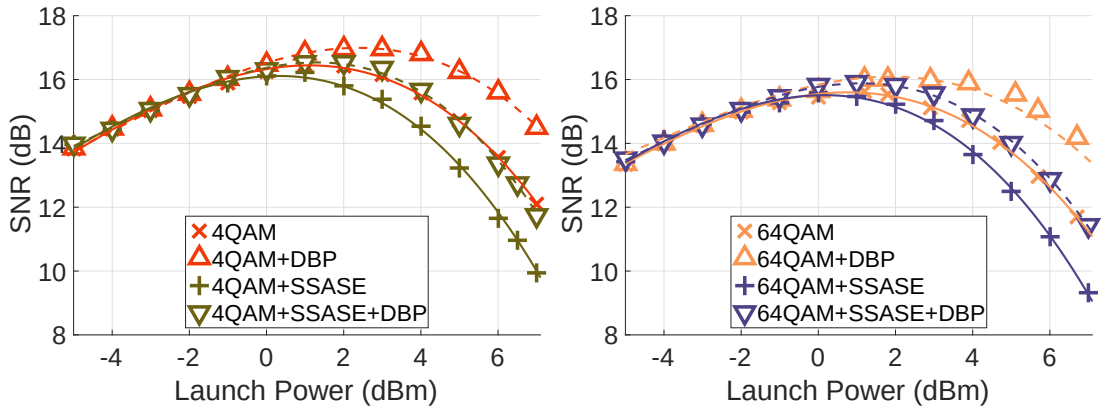

Figure 4.5: Experimental results showing SNR as a function of launch power for 7 channels after 11 spans 1114 km containing (a) 4QAM or (b) 64QAM. Plus markers showing the performance for all modulated channels, upward pointing triangles showing the performance with DBP, crosses showing the performance when using SS-ASE, downward pointing triangles showing the performance with SS-ASE and DBP. Lines showing the third order polynomial fitted to the data for calculating the peak SNR at optimum launch power

Due to the amount of noise from the transceiver it can be seen that the difference at optimum launch power is smaller than that measured at 2028 km in Section 4.5. At this distance of 1114 km, without DBP, the difference at optimum launch power is 0.29 dB and 0.09 dB for 4QAM and 64QAM respectively. After DBP the difference between modulated channel interferers and SS-ASE becomes 0.45 dB and 0.21 dB for 4QAM and 64QAM respectively. The gain in SNR from using DBP on 4QAM modulated channels and 4QAM with SS-ASE is 0.54 dB and 0.43 dB respectively. Likewise, for 64QAM the gain in SNR from DBP for modulated channel interferers and SS-ASE is 0.49 dB and 0.37 dB respectively. For both modulation formats the use of SS-ASE results in a worse performance of DBP. Due to increased NLI, DBP can mitigate more noise but the amount of noise that cannot be mitigated is increased by a larger amount. That is, the performance of SS-ASE with DBP is not as good as channels interferers with DBP.

To see this effect more clearly the effect of NLI mitigation is investigated as a function of distance for 64QAM at a fixed launch power of 1 dBm, the optimum launch power for the case of DBP. The SNR and DBP gain for the CUT is shown in Fig. 4.6. Here, it can be seen that at distances below 600 km the SNR is limited by the back-to-

back transceiver noise. As the distance was increased past this point the difference in the two loading schemes can be seen.

Due to the use of a fixed launch power the benefit of DBP in the case of SS-ASE is increased. This is not in contradiction with the previous results where the SS-ASE reduced the DBP gain, but the gain was calculated at the optimum launch power. If DBP gain was measured at optimum launch power for both 64QAM with channel interferers and SS-ASE the opposite trend would be seen where SS-ASE performs worse than modulated channels.

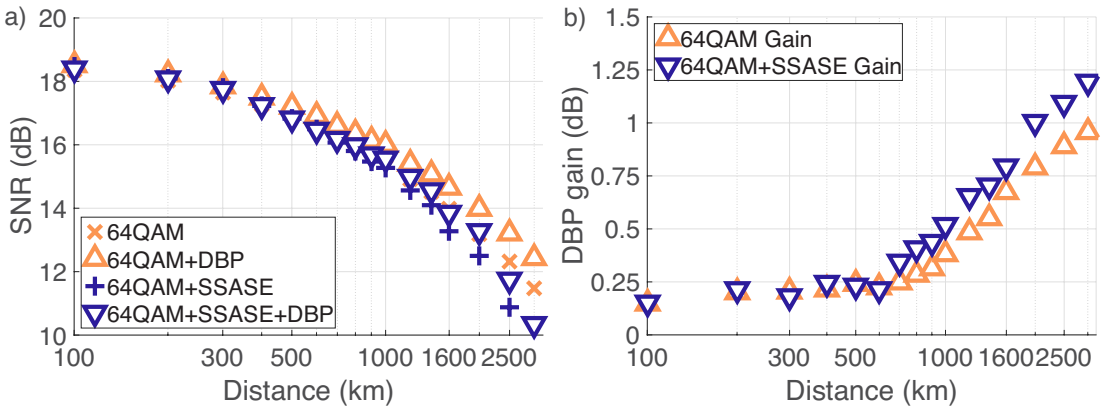

Figure 4.6: SNR (a) and gain from DBP (b) measured as a function of distance for 7 channels containing 64QAM at a fixed launch power of 1 dBm. Plus markers showing the performance for all modulated channels, upward pointing triangles showing the performance with DBP, crosses showing the performance when using SS-ASE, downward pointing triangles showing the performance with SS-ASE and DBP.

4.4 Straight line transmission link

This section describes one of the two experiments conducted at NICT. Here, nonlinearity mitigation is performed on a fully loaded C-band after straight line link transmission. Fig. 4.7 shows the system setup for the straight line link. The interfering channels consist of 56 odd and 56 even ECLs modulated with 25 GBd 16QAM Nyquist pulse shaped with a roll off of 0.1. The CUT was centred at 1551.17 nm with 2 channels on either side. These are modulated in an odd-even pattern with 24.5 GBd Nyquist pulse shaped signals with a roll off of 0.01. The 5 test channels are combined with the interfering channels with a WSS. This is then amplified ready for launch into the fibre transmission link.

The straight line link consists of 22 reels of fibre and 11 EDFAs preceding each span. Each fibre span is made of two reels, each 50.6 km long and the dispersion parameters of each span are given in table 4.1. The output of the final span was amplified, then bandpass filtered on the CUT with a width of 30 GHz before being detected with

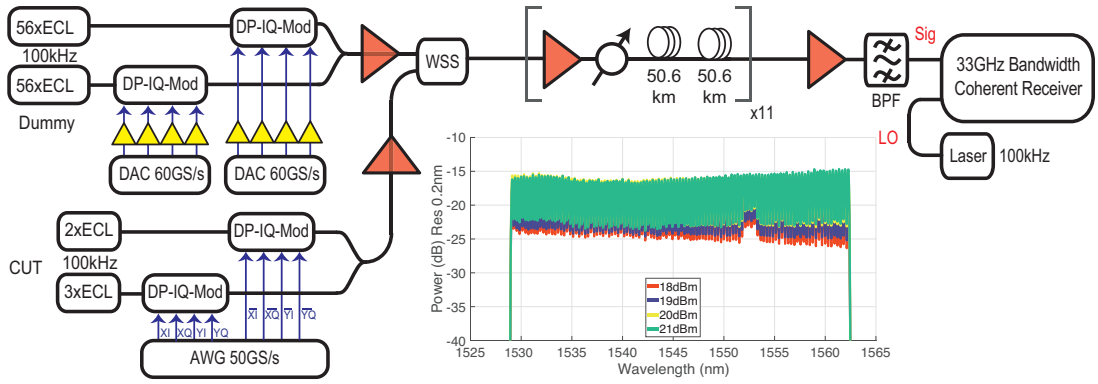

Figure 4.7: Setup showing straight line transmission system, inset showing received spectrum with resolution of 0.2 nm for different total launch powers. All spools are 50.6 km long leading to 101.2 km spans, where the dispersion for each spool is found in Table 4.1

Table 4.1: Table describing the dispersion map of the straight line link, showing each spool number in transmission order and its corresponding dispersion

Spool No.	Dispersion (ps/(nm.km))	Spool No.	Dispersion (ps/(nm·km))
1	16.4	12	16.3
2	16.3	13	16.4
3	16.3	14	16.2
4	16.5	15	16.2
5	16.4	16	16.1
6	16.4	17	16.0
7	16.3	18	16.2
8	16.3	19	16.3
9	16.2	20	16.3
10	16.2	21	16.3
11	16.0	22	16.3

a polarisation diverse coherent receiver. In order to maintain the spectral flatness each EDFA was set to have a fixed gain of 22 dB. This gain corresponds to the flattest spectral response of the EDFA. The EDFA gain is greater than the loss of the fibre span and hence, the following VOA was used to set the launch power and not change the subsequent EDFA's gain. The inset of Fig. 4.7 shows the received optical spectrum after 1100 km of transmission for total launch powers of 18, 19, 20 and 21 dBm corresponding to a launch power per channel of -2.5, -1.5, -0.5 and +0.5 dBm respectively. As can be seen, the previous technique of using a fixed gain mitigates the gain tilt but does not completely remove it as the EDFA is still sensitive to total input power.

The received CUT was sampled on an oscilloscope operating at 80 GS/s with an analogue bandwidth of 33 GHz. These measurements were processed offline with dispersion compensation, RRC filtering, LMS-RDE using 32 taps preconverged with CMA, frequency offset removal, carrier phase recovery and then the symbols were converted into bits as described in Appendix B. The received bits were then aligned with the transmitted ones, bit error rate (BER), SNR and MI were calculated.

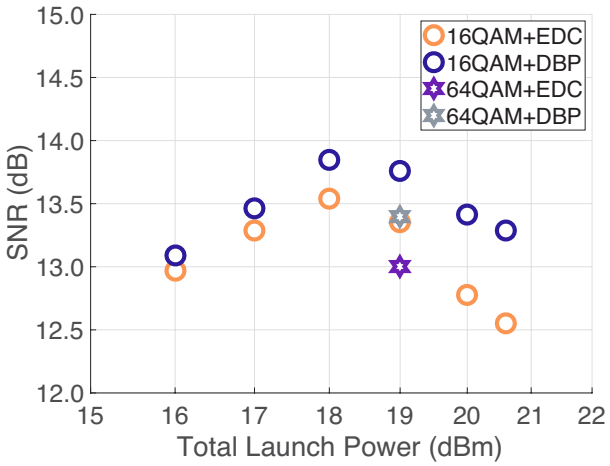

Figure 4.8: SNR measured as a function of total launch power for C-band transmission over a straight link with and without DBP. Circular markers show SNR for 16QAM and stars are for 64QAM.

The total launch power was swept from 16 to 20.5 dBm and the SNR is shown in Fig. 4.8. This range was limited such that the tilt across the entire received spectrum was less than 3 dB. It can be seen that the optimum launch power was measured to be 18 dBm or equivalently -2.5 dBm per channel. As the launch power was reduced by 1 dB the SNR dropped by 0.25 dB. This is smaller than the expected 1 dB because of the large bandwidth the CUT power is effected by the residual gain tilt. The signal power of the CUT changes by 0.5 dB, closer to the calculated change in SNR. The SNR of the 64QAM channels is seen to be lower than that of the 16QAM, this is due to the transceiver noise limit being higher for 64QAM and the modulation format dependence of NLI.

DBP was performed on the traces and is also shown in Fig. 4.8. For DBP to work optimally the nonlinear phase rotation and dispersion need to be known accurately. In [76], it was found that a change in dispersion of 0.05 ps/(nm·km) can change resultant SNR by 0.5 dB. The power profile and dispersion map have to be accounted for and is shown in table 4.1.

The algorithm was run both with and without knowledge of the dispersion map. In the 'no knowledge' case the total dispersion of the link is assumed to occur uniformly such that each span has the mean dispersion of all the spools. The difference between having no knowledge and full knowledge was found to be 0.01 dB, not statistically important. From Fig. 6 in [75] it can be seen that the sensitivity to dispersion becomes important for full field DBP. It is not known if this sensitivity is a function of the amount of back propagated bandwidth or a function of how close the back propagated bandwidth is to full field.

The improvement in SNR at optimum launch power was measured to be 0.41 dB. This is slightly less than 0.54 dB gain measured in the recirculating loop experiment

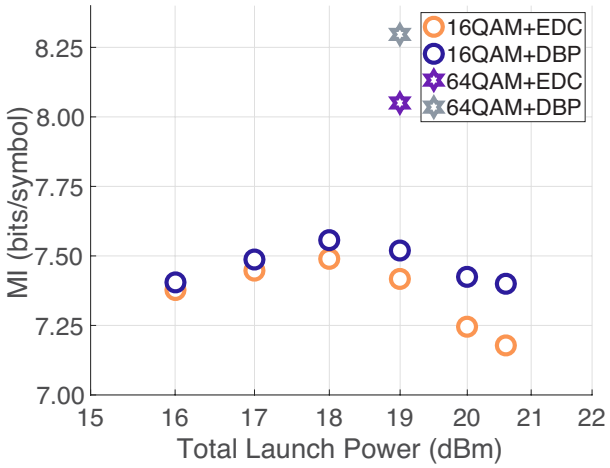

Figure 4.9: MI measured as a function of total launch power for C-band transmission over a straight link (1100 km) with and without DBP. Circular markers show SNR for 16QAM and stars are for 64QAM. For 64QAM transmission a total throughput of 22.01 and 22.77 Tb/s with and without DBP is achieved

in Section 4.3. The difference in DBP gain between the straight line and recirculating loop is quite small at 0.1 dB and even though the transmission distance is the same, other parameters are different. For the straight light and loop experiments, the transmission bandwidths were 4000 GHz and 400 GHz and the symbol rates were 25 GBd and 40 GBd respectively. In the straight line case, the dispersion map was taken into account but the launch power into each span was assumed to be constant. The measured gain could be improved if any knowledge of power variation was given to the DBP algorithm.

Fig. 4.9 shows the MI for CUT with and without DBP, calculated using Eq. 2.6 in Sec. 2.1.2. Additionally shown are 64QAM points (stars) which are 0.63 bits and 0.78 bits higher than 16QAM. This is experimental confirmation that when using MI as a figure of merit, the higher achievable rates come from using higher order modulation formats. The potential system throughput calculated by multiplying the number of carriers by their symbol rate and the MI for the carrier, allows comparison of effects on the entire C-band system. In terms of total throughput for this link, the use of16QAM together with DBP resulted in an increase of 190 Gb/s, whilst changing the modulation format to 64QAM & not performing DBP an increase of 1764 Gb/s was found. This demonstrates for a C-band system, there is a greater gain in throughput by choosing the appropriate modulation format rather than implementing nonlinearity compensation.

4.5 Intercore-crosstalk (IC-XT) on SNR

Spatial division multiplexing (SDM) is being widely investigated as a tool for increasing capacity of optical fibres, both in long-haul and short range links [144]. MCF tech-

nology is rapidly improving and provides a route to investigate potentially very high spectral efficiencies [132]. One of the limitations of SDM is crosstalk (XT) between adjacent spatial channels. The IC-XT stems from power coupling between cores during propagation and so builds up in a distributed manner. This is phenomenologically different compared to in band XT from other optical components like splices, amplifiers and filters [101]. How the nonlinear nature of the fibre and XT interact is an area of active research [72, 73].

IC-XT can be a dynamic process that has to be studied over hours or even days [107]. The theory behind IC-XT is linked to phase matching points along the fibre [71]. When this condition is met, power transfer can occur from one core to another. Factors affecting the number of phase matching points include, skew between cores, bending radius of the fibre on its storage reel, the fibre temperature, the fibre's axial twist and the spectral occupation [137]. The intercore skew or delay between each core is measured in ps and can affect total IC-XT [103]. Also in [103] it was shown that IC-XT power fluctuations are mainly induced by a correlation between different spectral components. Fluctuations can be relieved by either transmitting through fibres with large inter-core skew or using moderate to high symbol rates, that is for a skew symbol rate product >10. However, signals that contain a strong carrier, like OOK or PAM4, maintain a level of crosstalk power variation, even for large skew and symbol rates. Thus, intensity modulated systems likely require a performance margin even at high symbol rates and skew values. In contrast, the observation of low crosstalk variation for higher order modulation formats suggests that no such margin is required for systems using these formats.

In [73] it is shown that with high launch powers (>2 dBm) the variance and mean of IC-XT is reduced. This study only featured CW light sources, but it was shown that both the variance and means of the IC-XT reduced above 2 dBm. Hence it can be implied that moving to the high power regime would reduce IC-XT at the expense of SNR, but nonlinearity mitigation, such as DBP, might be enough to overcome the nonlinear loss of SNR to make the MCF more viable due to effectively lower IC-XT.

4.5.1 Modelling the impact of IC-XT

When only EDC is performed, the $\mathrm{SNR}_{\mathrm{EDC}}$ after long distance transmission is dominated by four separate, independent, noise components: ASE noise variance σ^2_{ASE}, transceiver noise variance σ^2_{TR}, nonlinear interference noise variance σ^2_{NLI} and IC-XT noise σ^2_{XT}. The noise variance after transmission can then be estimated as the following sum,

$$\sigma^2_{\mathrm{EDC}} = \sigma^2_{\mathrm{ASE}} + \sigma^2_{\mathrm{TR}} + \sigma^2_{\mathrm{NLI}} + \sigma^2_{\mathrm{XT}}. \tag{4.7}$$

The variance of each of these noise contributions have zero mean so the variance is equal to the noise power itself.

This results in the received $\mathrm{SNR}_{\mathrm{EDC}}$ being described as,

$$\frac{1}{\mathrm{SNR}_{\mathrm{EDC}}} = \frac{1}{\mathrm{SNR}_{\mathrm{ASE}}} + \frac{1}{\mathrm{SNR}_{\mathrm{TR}}} + \frac{1}{\mathrm{SNR}_{\mathrm{NLI}}} + \frac{P_{\mathrm{XT}}}{P_{\mathrm{s}}}, \tag{4.8}$$

where $\mathrm{SNR}_{\mathrm{ASE}}$ is the SNR as a result of cumulative noise power from the EDFAs in the link P_{ASE}, $\mathrm{SNR}_{\mathrm{NLI}}$ is the SNR due to NLI, P_{XT} the time averaged crosstalk power, P_s the signal power, where $\mathrm{SNR}_{\mathrm{TR}}$ is the back-to-back SNR that is set by the transceiver noise. This gives a theory of what the resultant SNR of the CUT would be with the assumption of linear noise.

Building upon the work in [38, 128] where using the GN model results in an equation for SNR when only EDC is performed, we add to this work by including a term to account for the IC-XT as reported previously [53]. Noise from IC-XT is distributed in nature but here it is assumed to be a lumped source of white gaussian noise. Just like P_{ASE} is added at the end of the span in the EDFA case, P_{ASE} from XT is added at the end of each span,

$$\mathrm{SNR}_{EDC} = \frac{P_s}{N^{(1+\varepsilon)}\eta P_s^3 + \kappa P_s + N(P_{\mathrm{ASE}} + P_{\mathrm{XT}})}, \tag{4.9}$$

with the number of spans N, the coherence factor ε, the NLI coefficient for one span η and $\kappa P_s = \sigma^2_{\mathrm{TR}}$ the transceiver SNR limit. This means that $\mathrm{SNR}_{\mathrm{TR}} = 1/\kappa$ allowing the experimental feature of transceiver noise to be captured. The factor κ_R incorporates another experimental issue, the balance of noise from the transmitter and receiver. This is set to $\kappa_R = 1$ for all noise at the receiver and $\kappa_R = 0$ for all noise at the transmitter. The split of noise becomes relevant in the case of NLI mitigation [128].

The nature of IC-XT as a distributed noise source is ignored here, as in [128] where the distributed noise from Raman amplification is treated as a lumped. Here the same assumption is made so the same accumulation coefficient ξ_1 for P_{ASE} and P_{XT} is used. In the EDC case additional IC-XT acts in the same way as increasing transceiver noise. It sets a limit to the maximum achievable SNR. In the DBP case it beats in the same way as P_{ASE} as it is added every span rather than at the transceiver so mixes with the signal during propagation. By corollary, the SNR after DBP can be calculated as in [38]. For simplicity, the SNR only when full field DBP is performed is shown, and is given by,

$$\mathrm{SNR}_{\mathrm{DBP}} = \frac{P_s}{\kappa P_s + N P_{\mathrm{ASE}} + 3\eta(\xi_1\left(P_{\mathrm{ASE}} + P_{\mathrm{XT}}\right) + \xi_2 \kappa_R P_s)P_s^2}, \tag{4.10}$$

where ASE accumulation factor is $\xi_1 = \sum_{k=1}^{N-1} k^{(1+\varepsilon)}$ and transceiver noise accumula-

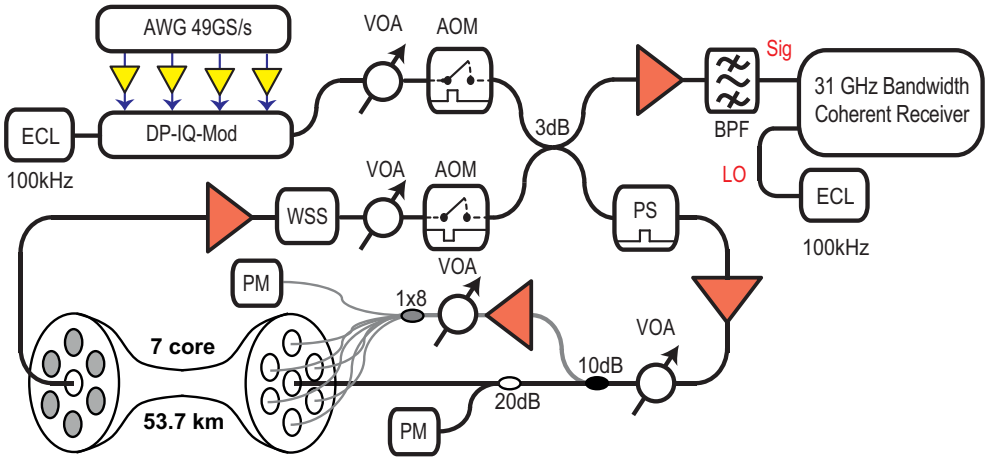

Figure 4.10: Experimental setup showing transmitter configuration, recirculating loop using multicore fibre and receiver. A tap before the central core is used for applying power to interfering cores so that the cores have recirculated light like the core under test.

tion factor is $\xi_2 = N^{(1+\varepsilon)}$. ξ_1 represents the residual beating between signal and ASE noise from the optical amplifiers that offset the span loss. ξ_2 represents the residual uncompensated beating between signal and transmitter noise and the residual beating between signal and receiver noise. Both of these beating accumulation contributions build up during the propagation in the physical link and are then either reduced or enhanced at the receiver side. The pre-factor 3 before η denotes the degenerate signal-noise mixing.

4.5.2 Experimental investigation of IC-XT

The setup used to investigate nonlinear mitigation in MCF is shown in Fig. 4.10. Here a 24.5 GBd signal is generated offline and Nyquist pulse shaped with a roll off of 0.01, this is modulated on to an ECL at $\lambda = 1550.16$ nm with a nominal linewidth of 100 kHz. This signal is sent into a recirculating loop containing a 53.7 km span of 7-core MCF. The fibre had a core diameter of 8.2 μm, a core pitch of 41 μm and a diameter of 160 μm. A loop synchronous polarisation scrambler is used to limit the effects of polarisation dependent loss and a WSS is used as a bandpass filter. IC-XT was emulated by using interfering channels generated from the loop output after each recirculation. The interfering channels were amplified and decorrelated with fibre patch cords before being re-injected into the adjacent fibre cores. Generating the interfering channels by taking a tap from the loop input ensured that the interfering channels had experienced transmission impairment and similar to that of the CUT, closely emulating a real MCF link.

Fig. 4.11 shows the SNR as a function of launch power for different IC-XT levels. At 2148 km the total accumulated IC-XT for the maximum and minimum values of XT/100 km -23.5 and -42.2 dB/100km correspond to -7.48 and -26.18 dB respectively.

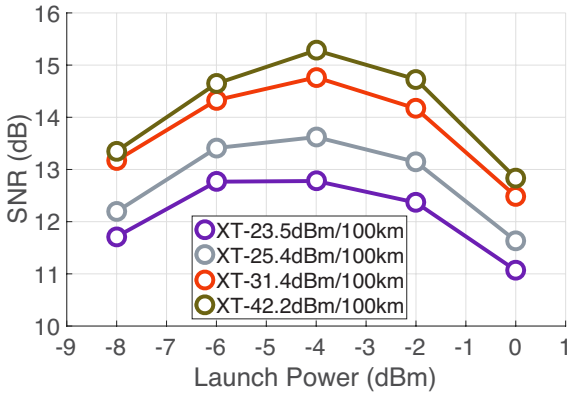

Figure 4.11: SNR shown as a function of launch power for a single 16QAM channel at a distance of 2148 km (40 recirculations) for different IC-XT levels

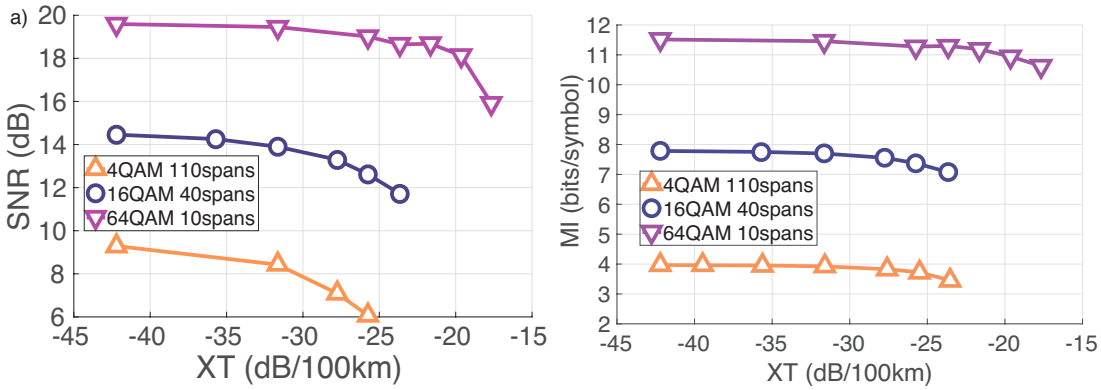

Figure 4.12: SNR and MI for 4QAM, 16QAM and 64QAM shown as a function of IC-XT at optimum launch power of -4 dBm for 10, 40 and 110 spans respectively

As can be seen, the higher the values of IC-XT reduce the SNR in all parts of the curve. The optimum launch power was found to be -4 dBm for all IC-XT levels. Changing from minimum to maximum IC-XT results in a drop in SNR of 2.7 dB at optimum launch power.

The SNR was then measured at optimum launch power for PDM-4QAM, PDM-16QAM and PDM-64QAM at 110, 40 and 10 spans respectively and is shown in Fig. 4.12. The addition of XT again reduces the SNR in what seems like a very significant way for all tested modulation formats. The lower order modulation formats have their SNR reduce quicker as a function of XT/100 km due to the greater transmission distances and associated accumulated XT.

In order to understand this in the context of system throughput, the effect of XT on achievable information rate (AIR) is shown in Fig. 4.12. The back-to-back MI achieved for PDM-4QAM, PDM-16QAM and PDM-64QAM was 4, 8 and 11.98 bits/s/Hz respectively. At these distances (110, 40 and 10 spans) a XT level of -32.2 dB/100 km (corresponding to the same launch power in all cores [102]), the achievable rate drops by 1.4% for PDM-4QAM, 1% for PDM-16QAM and 0.2% for PDM-64QAM. If a

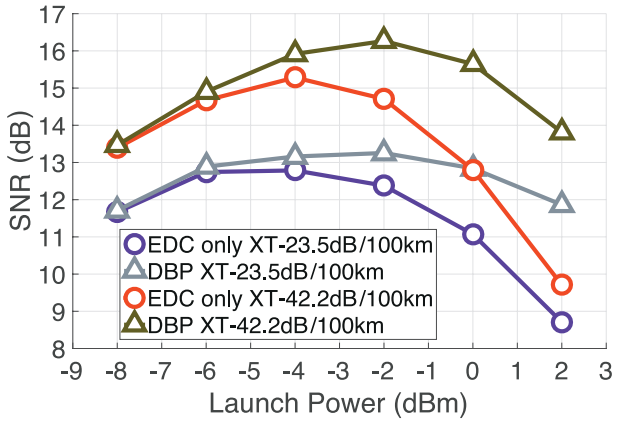

Figure 4.13: SNR shown as a function of launch power for a single 16QAM channel at a distance of 1880 km (35 recirculations) for the maximum and minimum IC-XT levels, with and without single channel DBP.

loss of 7% in achievable rate is permitted XT can be increased to -26, -25.2 and -19 dB/100 km, for 4QAM, 16QAM and 64QAM respectively. When maximum reach is not a limiting factor in link design, additional XT can be allowed, leading to finer core pitch, which would accommodate more cores in a fixed fibre diameter. This results in more spatial channels to multiplex over giving higher throughput. For PDM-4QAM after a long haul distance of 5,907 km, a XT of -26.6 dB/100 km drops the achievable rate by 0.31 bits, a loss of only 7.8%. For PDM-16QAM at a distance of 2148 km, the rate drops by 0.42 bits (5.4%) and for PDM-64QAM it drops by 0.17 bits (only 1.5%) after 537 km. The increasing loss of AIR with lower modulation formats is a result of the total accumulated XT being higher.

4.5.3 Nonlinearity mitigation in the presence of IC-XT

The effectiveness of the NLI mitigation technique DBP has been evaluated in the presence of additional noise from IC-XT. Fig. 4.13 shows the SNR of the CUT as a function of launch power for 2 different IC-XTs (-23.5 and -42.2 dB/span), with and without DBP. The maximum achievable SNR at the optimum launch power of -4 dBm is reduced by 2.7 dB when increasing the IC-XT from -23.5 dB/100 km to -42.2 dB/100 km. When DBP was applied, the optimum launch power was increased to -2 dBm. The corresponding SNR gains with respect to the EDC case were 0.47 dB and 0.99 dB for IC-XT values of -23.5 dB/100 km and -42.2 dB/100 km, respectively. This shows that DBP is still effective in removing NLI on MCF transmission in the presence of IC-XT. However, the achievable DBP gain was clearly reduced with the increase of IC-XT.

To show this effect clearly in Fig. 4.14 SNR is plotted as a function of IC-XT for a distance of 1880 km (35 spans) for a constant launch power of -2 dBm. As can be seen increased levels of IC-XT lead to a reduction in SNR. The theory lines shown are Eqs. 4.8, 4.9 & 4.10 where $\mathrm{SNR}_{\mathrm{EDC}}$ is plotted, the P_{XT} term is calculated as the total

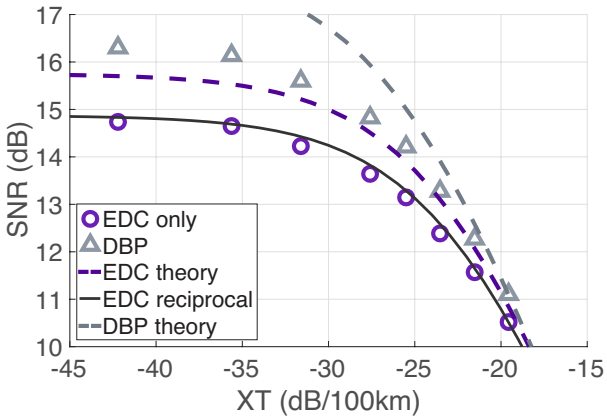

Figure 4.14: SNR shown as a function of IC-XT at 1880 km with and without DBP at a constant launch power of -2 dBm. Dashed lines showing the analytical SNR for the given IC-XT. Solid line showing the additive noise from IC-XT on a fixed SNR at minimum IC-XT

cumulative IC-XT and all the other noise terms are kept constant. A reduction of 1 dB in SNR corresponds to an IC-XT level of -27.6 dB/100 km, which is less than the case of equal launch power in all cores. In the case of DBP it is seen that there is gain for all investigated levels of IC-XT and the gain progressively decreases with increasing IC-XT. It can be noted that this graph looks very similar to Fig. 6(b), where SNR is limited by another noise source that is not IC-XT causing the plateau at low IC-XTs. The amount of gain DBP provides, is known to be a function of the amount of signal-noise mixing [104]. As this is a stochastic component that cannot be mitigated, it is expected to decrease steadily with increasing IC-XT. The noise sources that contribute to signal-noise mixing are P_{XT}, ASE noise power or the ultimately limiting transceiver noise [38]. For larger IC-XT values there is more noise power present, that increases the amount of mixing noise power and, hence, reduces the achievable gain. At high IC-XTs the curve tends to being linear as IC-XT becomes the dominant noise source with a smooth transition as both noise sources are contributing factors.

The DBP theory curve in Fig. 4.14 is seen to not agree with the experiment for IC-XT less than -25 dB/100 km. This was discovered to be due to a faulty AOM used in the experiment. When given the signal to continuously block transmission of light, the AOM outside of the recirculating loop was discovered to start turning transparent after 30 spans. This in turn would let light enter the loop at the same wavelength as the recirculating signal, leading to an apparent increase in IC-XT with distance. This causes all of the experimental points where the dominating noise source is not IC-XT to be lower than expected. The EDC reciprocal line in Fig. 4.14 was calculated by incorporating the light that leaked into the loop into the P_{ASE} for the minimum IC-XT level, then adding the IC-XT as was measured. This shows good agreement but is not rigorous enough to be used to corroborate Eqs. 4.9 & 4.10.

Fig. 4.15 shows the SNR improvement after DBP has been applied for different

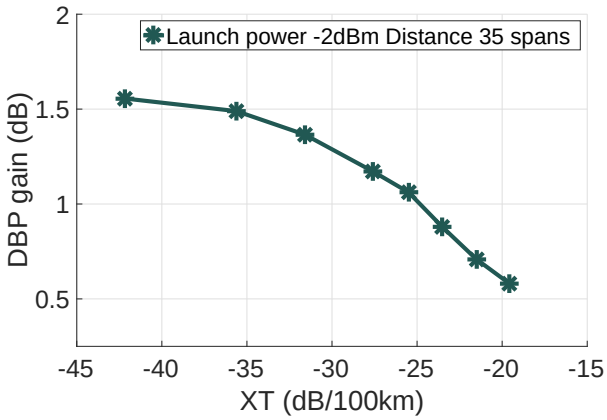

Figure 4.15: Measured SNR gain from DBP shown as a function of IC-XT at 1880 km at optimum launch power of -2 dBm

IC-XT levels at a constant launch power of -2 dBm. Here the effectiveness of DBP can be clearly seen to drop with increasing IC-XT. The step from minimum IC-XT of -42 dB/100 km to -35.66 dB/100 km the DBP gain drops by only 0.1 dB, a rate of 0.01 dB per dB. It is noted that with an IC-XT of -31.6 dB/100 km the case for equal power into all cores [102], DBP gain drops from 1.56 dB to 1.35 dB a reduction of only 13.5%. For IC-XT higher than this the DBP gain drops more significantly at a rate of 0.077 dB per dB. It is noted that in the case of full field DBP, transceiver noise plays a significant part of the potential gain [38]. With higher levels of IC-XT, more signal-XT mixing occurs and DBP cannot mitigate these mixing terms due to the noise's stochastic nature as well as deterministic SCI.

The measured back-to-back SNR of the system was 24.5 dB and with the transmission distance shown here of 1876 km, the received SNR is 15 dB. At this distance the effect of transceiver noise on DBP is reduced but as shown in [38], this is still significant as it is less than 16 dB away from the maximum back-to-back SNR. Hence, longer transmission distances are required until the received SNR reaches 8.5 dB, where the DBP gain would be limited by P_{ASE} and P_{XT}.

It is expected that the trends seen here will not extend to broadband transmission, where the captured and back propagated bandwidths are smaller than that transmitted. In this case, the assumptions made in Eq. 4.10 are no longer valid. When the transmission bandwidth is larger than the back propagated bandwidth more uncompensatable NLI is generated by the receiver, since it is not captured. This reduces the maximum potential DBP gain and would affect the overall conclusions of this work in a full C-band transmission.

Fig. 4.16 shows DBP gain as a function of different distances. As can be seen longer transmission distances correspond to higher DBP gain, but distances beyond 50 spans start to show a reduction in gain as the ASE signal mixing becomes larger. This shows some of the limiting cases of DBP gain: at low IC-XT as the SNR is still within

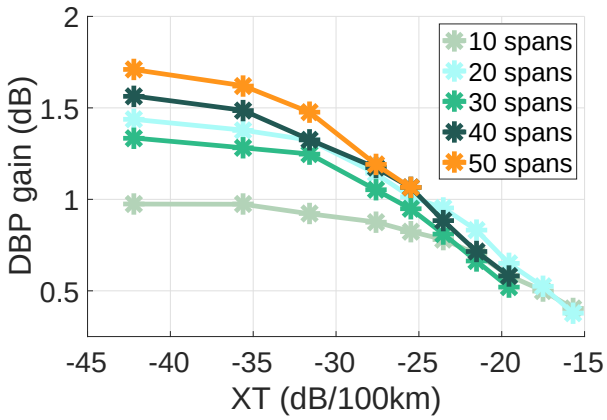

Figure 4.16: Measured gain in SNR from DBP shown as a function of IC-XT at fixed launch power of -2 dBm, for different distances

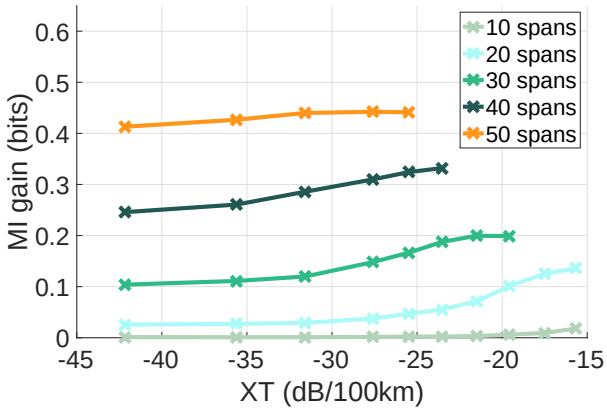

Figure 4.17: Measured MI gain for 16QAM shown as a function of IC-XT at fixed launch power of -2 dBm, for different distances

the effects of the transceiver limit. The balance of noise sources can be seen to shift from transceiver noise to crosstalk as IC-XT is increased. For high IC-XTs (>25dB) it can be seen that the noise dominates and so DBP gain is set by the IC-XT. From [38] when received SNR is less than 2/3 of the transceiver limit (2/3·24 dB = 16 dB) DBP gain is reduced by less than 0.1 dB. The corresponding threshold for IC-XT noise dominance after 10, 30 and 50 spans is -26, -30.7 and -33 dB/100km respectively.

The impact of this gain on achievable rate is shown in Fig. 4.17 where gain MI is plotted as a function of XT. MI gain with increasing XT is seen to not decrease monotonically. This figure seems to conflict with Fig. 4.15 but this is not the case. The absolute SNR with higher XT is lower. This is the region in which MI is no longer limited by the number of bits per symbol, so the gain from DBP over comes the loss in SNR. This happens until the slope of bits/SNR stops changing, then the loss of SNR is more significant than the DBP gain and MI starts to drop again.

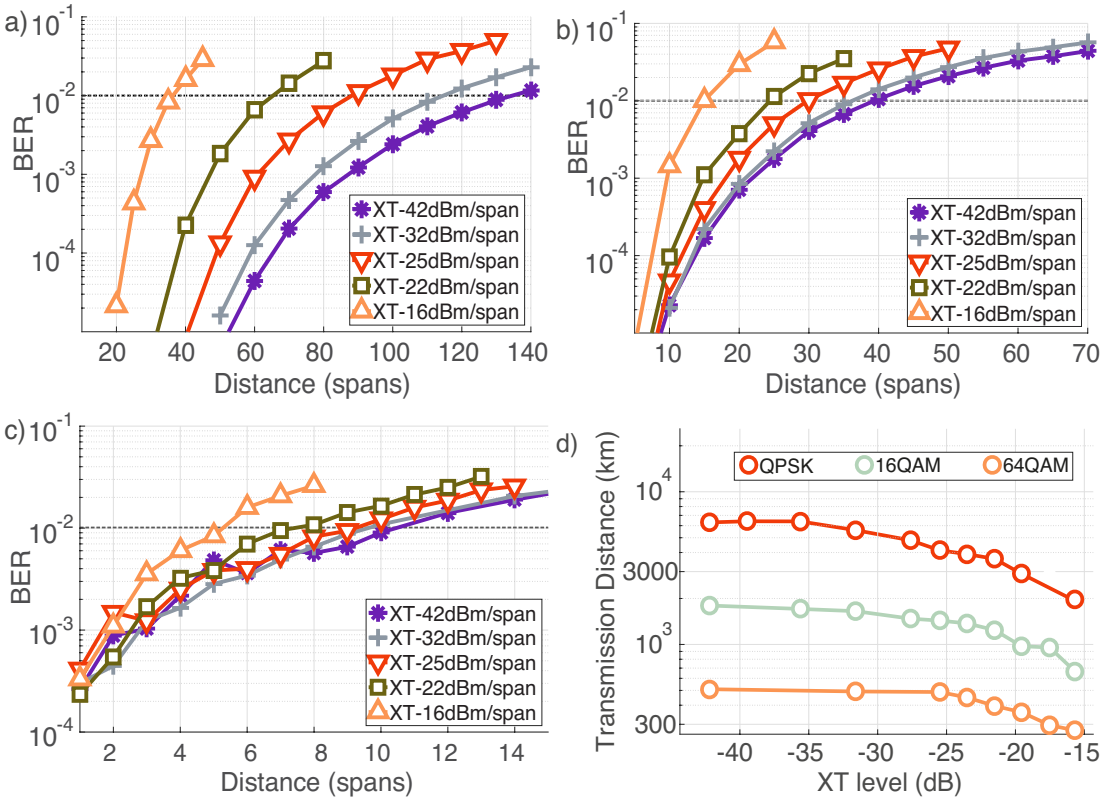

Figure 4.18: Plot of BER against distance for (a) 4QAM, (b) 16QAM and (c) 64QAM with 5 different levels of crosstalk and (d) transmission distance for a BER threshold of 0.01 as a function of IC-XT

4.5.4 Impact of crosstalk on square QAM formats

The modulation format dependence of NLI is well understood [17, 37, 82, 129] but is not thoroughly investigated in the presence of IC-XT. The modulation format 4QAM or QPSK is statistically the most different to Gaussian and has the largest difference in performance of those investigated here. 16QAM is a large step up from QPSK and 64QAM is effectively the same as 16QAM in terms of NLI generation [129]. Higher order QAM still has an offset to a Gaussian modulation format but in terms of NLI the differences are negligible. The same setup (Fig. 4.10) was used to investigate the dependence of IC-XT on transmission distances for different modulation formats (4QAM, 16QAM and 64QAM).

The back-to-back achievable SNRs for 4QAM, 16QAM and 64QAM were measured to be 23.7, 24.1 and 23.9 dB respectively. The difference between modulation formats here is small so the change in transceiver noise is not a source of modulation format dependence. With the transmission distance shown here of 1876 km, the effect of transceiver noise on DBP is reduced but is still significant. For transceiver noise to contribute less than 0.1 dB the SNR needs to be 8 dB [38]. In the longer transmission case the gain is mostly limited by the noise generated in transmission such as P_{ASE} and P_{XT}.

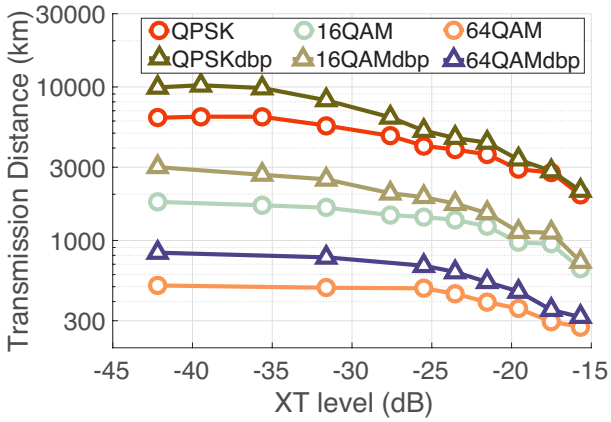

Figure 4.19: Achievable transmission distance at a BER threshold of 1.5×10^{-2} as a function of crosstalk power per span for 4QAM, 16QAM and 64QAM with and without DBP

Figs. 4.18 (a), (b) & (c) show the BER as a function of distance for QPSK, 16QAM and 64QAM modulation formats, respectively, as a function of distance for 5 different IC-XT levels with a fixed input power of -2 dBm. It can be seen that the BER gets worse as the distance increases for all modulation formats. This is due to the build up of P_{ASE} and P_{XT}. For a fixed BER of 0.01 and the minimum IC-XT level of -42 dB, the distance QPSK 16QAM and 64QAM reach were 117, 33 and 9 spans. The distance 64QAM reaches for a given BER is lower than that of 16QAM, which in turn is lower than that of QPSK. This is due to the different OSNR requirements for each modulation format as the symbols are spaced closer together. For the highest IC-XT level of -16 dB, the achievable transmission distance drops to 37, 12 and 4 spans. For higher levels of IC-XT it can be seen that the achievable distances are reduced by more than 50% for all modulation formats.

By taking a BER threshold level of 0.01 as shown on the graph as horizontal lines, the performance of each modulation format can be compared. The intersection of the threshold with the transmission lines for each IC-XT sets a maximum achievable distance for each modulation format. It is now possible to plot achievable distance as a function of IC-XT for all 3 modulation formats and this is shown in Fig. 4.18d). From this graph it can be seen that all modulation formats' transmission distance is limited by additional IC-XT. This is to be expected from Eq. 4.9 as the IC-XT limits the maximum SNR for any distance. It can be seen that IC-XT starts to affect the achievable transmission distance for 4QAM before 16QAM and both of those before 64QAM. It is noted that the way this threshold is set, the modulation format dependent NLI is still a factor in SNR and the achievable BER. So it would be expected to see modulation format dependence on the transmission distances as seen in Fig. 4.18 (d).

The impact of DBP on transmission distance was also investigated by applying the same BER threshold of 0.01 as before and is shown in Fig. 4.19. Here the gain in SNR can be seen to translate to an improvement in transmission distance for all IC-XT

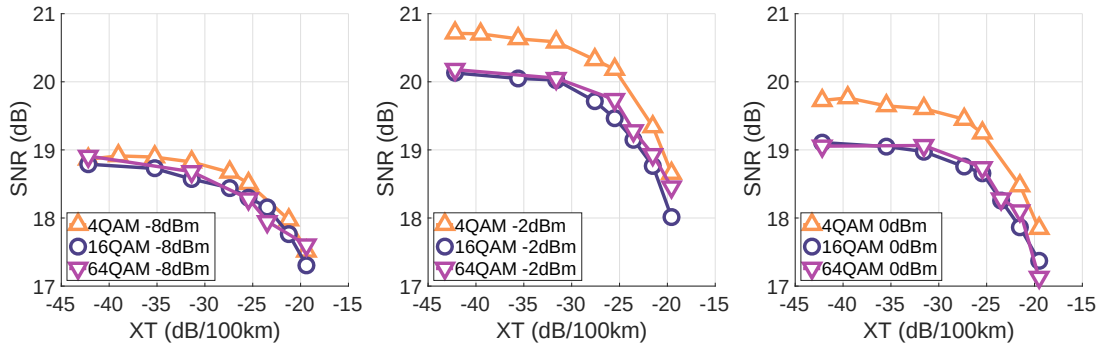

Figure 4.20: SNR as a function of IC-XT for 4QAM, 16QAM and 64QAM at distance of 10 spans 563 km. (a) showing a launch power of -8 dBm and (b) at -2 dBm and (c) 0 dBm.

levels. The gain for 4QAM in distance is larger than that of 16QAM and 64QAM because the modulation format has a higher tolerance to noise. This DBP gain is seen to reduce with IC-XT as the combination of shorter transmission distance and more signal-XT beating, as in the previous section.

The effect of modulation format dependance of NLI can be seen more clearly by looking at the SNR at a fixed transmission distance as a function of modulation format and IC-XT. This is shown in Fig. 4.20 for a launch power -8 dBm, -2 dBm and 0 dBm (a), (b) and (c) respectively at a distance of 10 spans.

At -8 dBm the SNR for 4QAM is 0.2 dB higher than 16QAM and 64QAM, at -2 dBm 0.5 dB higher and at 0 dBm 0.6 dB higher. Here it can be seen that the modulation format dependence of NLI is still present even at -8 dBm, 4 dB below the optimum launch power. As the IC-XT is increased the SNRs of all modulation formats converge as the IC-XT becomes the dominant noise source. This is most apparent in (a) where the NLI is least significant. This suggests that the effect of IC-XT on SNR is modulation format independent.

4.6 Summary

We proposed a method of measuring the statistical properties of NLI, as described by the time-varying ISI model. Estimating the variance of these coefficients is crucial for assessing the potential gains of nonlinearity mitigation by means of equalisation, whereas the correlation times are needed to determine the required tracking speed. Furthermore, such correlation measurements can be used to improve NLI mitigation, as shown in [48]. It was shown that although the largest contribution to NLI comes from the zeroth-order ISI (PPRN), the accumulated contribution of higher-order ISI terms is significant. The proposed method allows the experimental evaluation of the autocorrelation functions of the elements of the ISI matrices, as well as the cross-correlations between elements of different ISI orders.

Nonlinear mitigation was applied on a straight line link. The sensitivity of the DBP algorithm to accurate dispersion maps was investigated. In the case of full C-band transmission, sensitivity was not found due to the small single channel back propagated bandwidth.

By looking at the effect of IC-XT in terms of achievable information rate, the impact on throughput was determined. It is found that achievable rates are not strongly affected by XT. For 4QAM, an intercore-crosstalk of -26.6 dB/100km leads to a transmission rate loss of less than 8% at 5,700 km.

For the first time, we have shown that the use of DBP for NLI mitigation provides performance gain when used in a single-mode MCF transmission scenario. The results for long distance MCF transmission experiments show that the use nonlinear compensation techniques is feasible in the presence of IC-XT. Reducing the amount of IC-XT can give a performance improvement from two factors: the OSNR is greater and SNR improves from better nonlinear compensation. The gain in SNR is seen to drop with increasing IC XT. For the case of equal launch power into all cores the DBP gain is seen to drop by just 13.5%. With lower IC-XT values DBP becomes limited by transceiver noise.

The modulation format dependance of IC-XT was also investigated. The results imply the independence of IC-XT from modulation format, for RRC pulse shaped QAM signals at a symbol rate of 24.5 GBd. Further confirmation would require taking data points at lower launch power. This would enable the removal of the NLI power and the modulation format dependence on SNR and, hence, extract just the effect of additional XT and any modulation format effect.

5

Conclusions and further work

THE NEXT GENERATION of optical networks demand information rates to be increased more than ever before. This requires maximising the amount of information a system can transfer within experimental limits. In this work, techniques to assess system performance in the presence of fibre nonlinearity were experimentally studied.

The three main issues were targeted to continue increasing fibre throughput, they were: 1) Transmission systems must utilise large bandwidths. Large bandwidth emulation was investigated with the use of spectrally shaped-amplified spontaneous emission (SS-ASE) noise and was experimentally verified. 2) Subsequent investigations demonstrated that if nonlinear interference (NLI) is treated as deterministic rather than noise, there is potential to mitigate NLI. Again this was experimentally verified. 3) When using multicore fibre the signal is affected by intercore-crosstalk (IC-XT) but NLI is still present and still limits throughput. It was experimentally shown that the nonlinearity compensation technique digital backpropagation (DBP) is still effective at compensation.

Overall conclusions for all the research carried out are presented in the next section.

5.1 Summary of Research

Due to its simplicity, SS-ASE was investigated as an alternative to the use of independently modulated channels for loading bandwidth for the experimental evaluation of

optical transmission systems. Experimental and theoretical results were presented in chapter 3. The results generated with this technique showed that SS-ASE will always provide a lower bound on the system performance for any bandwidth. It was found that the discrepancy between modulated channels and SS-ASE is reduced for smaller SS-ASE bandwidths, higher order modulation formats and fewer emulated channels. This technique was then used to demonstrate the feasibility of a 1 Tb/s transceiver in a fully loaded C-band transmission system and to load the C and L-bands (up to 7.3 THz) to validate the Gaussian noise (GN) model and up to 9 THz to study Raman scattering, [115]. This technique is also being utilised in experiments outside of UCL [13, 109] to demonstrate potential capacity of transmission systems over broad bandwidths. The results showed that this technique is useful for emulating modulated channels.

A straight line link was used to investigate NLI in broadband transmission. A straight line link is the step between a laboratory recirculating loop and an installed fibre link. This allows control of the parameters of each span but sacrifices the flexibility and smaller equipment requirements of a loop. Using a straight line meant, it was possible to investigate how DBP is affected by a dispersion map in broadband transmission. It was found that in this case, where the backpropagated bandwidth is far smaller than that was transmitted, sensitivity to a dispersion map was not present. As single channel DBP is used as a NLI mitigation technique in transmission links that require cost conscious implementation, the effects of a dispersion map on single channel DBP is unlikely to be the limiting factor in the amount of NLI mitigation. Hence, for broadband transmission systems employing single channel DBP, it is unlikely that a dispersion map accurate to 0.1 ps is required for best NLI mitigation.

NLI was modelled as an inter-symbol interference (ISI) model and then experimentally verified. The zeroth order ISI correlations, which are characterised as phase noise, did not match between experiment and theory. This is due to the interplay between laser phase noise and phase recovery algorithm, which act on this order; the digital signal processing (DSP) output being dependent upon each manifestation of noise and hence changes for each waveform. Any non-zero order correlation showed agreement between theory and experiment. A growth in ISI coefficient variance is due to the accumulation of larger nonlinearity. Growth in the ISI correlation time was attributed to the larger overall walk-off. The discovery that the higher orders of ISI remain correlated over notable time durations, suggests that their equalisation may be feasible. The summed variance of 1^{st}, 2^{nd} and 3^{rd} orders is larger than the zeroth order variance, suggesting that the benefit of properly optimised equalisation should be notable [48].

Experiments into spatial division multiplexing (SDM) were conducted in the form of single-mode multicore fibre. A novel technique to emulate different levels of crosstalk in a MCF recirculating loop was implemented. Filling the interfering cores with signals that also had been recirculated meant that the IC-XT experienced by the channel

under test (CUT) closely mimicked that of a real transmission. This enabled an experimental investigation of crosstalk modulation format independence and, for the first time, the impact of crosstalk on DBP to be studied. In the theory presented, crosstalk is assumed to take the form of noise added in a lumped manner just as noise from distributed Raman amplification or EDFA ASE noise, but limited SNR like transceiver noise. That is, noise is added after each span as a function of signal power, which limits the maximum achievable SNR. The effect of IC-XT on modulation formats was investigated and it was demonstrated that the IC-XT noise power was not dependent on the modulation format of the channels in the interfering cores agreeing with that shown in [103]. The impact of IC-XT on DBP was also studied, building upon the transceiver noise work in [38]. The origin of IC-XT is power leakage from core to core hence, IC-XT noise adds a limit to SNR as a function of transmitted distance. In the case of digital backpropagation, IC-XT noise reduces the potential gain in the same way as ASE noise from amplification. The accumulated IC-XT was found to impose a limit on the amount of NLI mitigation that DBP is able to produce. For the system studied if IC-XT was below -35.7 dB/100 km, DBP gain is reduced by only 0.1dB.

5.2 Future Work

5.2.1 Odd-even channel correlation

As described earlier in this thesis, SS-ASE can be used to emulate modulated channels in transmission. The experimental investigation was limited to just one bandwidth of 240 GHz. The theory compared SS-ASE to independent modulated channels but the conducted experiment was limited to comparing SS-ASE to odd-even modulated channels. It has been theoretically shown in [23] and experimentally in [13] that using odd-even channels can over estimate the amount of NLI. Dar [23] showed NLI correlation when using odd-even modulation scheme, can lead to anomalously large NLI mitigation gains. Cai [13] showed the difference between odd-even correlated channels and 'decorrelated' SS-ASE over broad bandwidths. But using SS-ASE doesn't show the complete picture as SS-ASE already has inherent discrepancy in terms of NILN generation compared to channels. A large bandwidth comparison between SS-ASE, channels, and odd-even correlation on NLI is needed. Transmission of 90 channels is required to demonstrate the difference between each case.

5.2.2 SS-ASE in multicore fibres

SS-ASE was investigated as an alternative to transmission of a large number of modulated channels in single core fibres. The next logical step is to use SS-ASE for loading

of multicore fibres (MCF)s to emulate XT from adjacent cores. Here, the two cases to compare would be: the CUT propagating with modulated channels in the interfering cores and propagating with SS-ASE with identical bandwidth to the modulated channels. XT is known to fluctuate over time when using CW sources or modulation formats with a carrier and is most stable when using ASE [103]. This means SS-ASE needs to be investigated in the context of emulating different modulation formats such as on-off keying (OOK), pulse amplitude modulation (PAM) and quadrature amplitude modulation (QAM).

5.2.3 DBP in the presence of a dispersion map

When performing NLI mitigation using full field DBP the launch power and dispersion parameters need to be accurately represented in the algorithm for maximum mitigation. In a straight line link or in installed fibre links, a known dispersion map should help provide maximum gain. The experiment conducted in this thesis did not show such sensitivity due to the large transmission bandwidth and small back propagated bandwidth. For this experiment to show this phenomena a smaller transmission bandwidth is required such that dependence can be seen. It should be investigated if DBP's sensitivity to dispersion is a function of the amount of back propagated bandwidth or a function of the how close the back propagated bandwidth is to that transmitted. Dispersion managed systems have periodic sections of fibre with opposite dispersion in order to optically undo accumulated dispersion. Understanding the impact of this type of dispersion is important for systems that have installed dispersion compensating fibre such as Deutsche Telecom [112], as updating installed fibre is an expensive endeavour.

References

[1] G. P. Agrawal, "Signal Propagation in Fibers," in *Lightwave Technology Telecommunication Systems*, 2005. 38, 40

[2] E. Agrell, A. Alvarado, and F. R. Kschischang, "Implications of information theory in optical fibre communications," *Philosphical Transactions A*, 2015. 24, 32, 34

[3] A. Alvarado, T. Fehenberger, B. Chen, and F. M. J. Willems, "Achievable information rates for fiber optics: Applications and computations," *Journal of Lightwave Technology*, vol. 36, no. 2, pp. 424–439, Jan 2018. 34, 35

[4] A. Alvarado, E. Agrell, D. Lavery, R. Maher, and P. Bayvel, "Replacing the soft-decision FEC limit paradigm in the design of optical communication systems," *Journal of Lightwave Technology*, vol. 34, no. 2, pp. 707–721, 2016. 35

[5] P. Bayvel, R. Maher, T. Xu, G. Liga, N. A. Shevchenko, D. Lavery, A. Alvarado, and R. I. Killey, "Maximizing the optical network capacity," *Philosophical Transactions of the Royal Society A: Mathematical, Physical and Engineering Sciences*, vol. 374, no. 2062, p. 20140440, 2016. 10, 18, 20, 21

[6] S. Beppu, K. Kasai, M. Yoshida, and M. Nakazawa, "2048 QAM (66 Gbit/s) Single-Carrier Coherent Optical Transmission over 150 km with a Potential SE of 15.3 bit/s/Hz," *Optics express*, vol. 23, no. 4, pp. 6–8, 2014. [Online]. Available: http://www.opticsinfobase.org/abstract.cfm?uri=OFC-2014-W1A.6 10, 21

[7] P. W. Berenguer, T. Rahman, A. Napoli, M. Nölle, and C. Schubert, "Nonlinear Digital Pre-Distortion of Transmitter Components," *Journal of Lightwave Technology*, vol. 34, no. 8, pp. 1739–1745, 2016. 45, 47, 68, 85

[8] N. S. Bergano, J. Aspell, C. R. Davidson, P. R. Trischitta, B. M. Nyman, and F. W. Kerfoot, "Bit error rate measurements of 14000 km 5 Gbit/s fibre-amplifier transmission system using circulating loop," *IET Electronic Letters*, vol. 27, no. 21, pp. 1889–1890, Oct. 1991. 52

[9] N. S. Bergano and C. R. Davidson, "Circulating loop transmission experiments for the study of long-haul transmission systems using erbium-doped fiber amplifiers," *IEEE/OSA Journal of Lightwave Technology*, vol. 13, no. 5, pp. 879–888, May 1995. 52

[10] F. Buchali, F. Steiner, G. Böcherer, L. Schmalen, P. Schulte, and W. Idler, "Rate Adaptation and Reach Increase by Probabilistically Shaped 64-QAM: An Experimental Demonstration," *Journal of Lightwave Technology*, vol. 34, no. 7, pp. 1599—-1609, 2016. 22, 23

[11] J. Cai, H. G. Batshon, M. V. Mazurczyk, O. V. Sinkin, D. Wang, M. Paskov, W. Patterson, C. R. Davidson, M. Bolshtyansky, and D. G. Foursa, "51.5 Tb/s Capacity over 17,107 km in C+L Bandwidth Using Single Mode Fibers and Nonlinearity Compensation," *Optical Fiber Communication Conference (OFC)*, pp. 12–14, 2017. 22, 24

[12] J. Cai, H. G. Batshon, M. V. Mazurczyk, O. V. Sinkin, D. Wang, M. Paskov, W. Patterson, T. E. Subcom, and I. W. West, "70 . 4 Tb / s Capacity over 7 , 600 km in C + L Band Using Coded Modulation with Hybrid Constellation Shaping and Nonlinearity Compensation," *Journal of Lightwave Technology*, vol. 36, no. 1, pp. 114–121, 2018. 22, 24, 80

[13] J. Cai, Y. Hu, A. Turukhin, M. V. Mazurczyk, M. Paskov, H. G. Batshon, C. R. Davidson, M. Bolshtyansky, and D. G. Foursa, "On the Effects of Transmitter Induced Channel Correlation in Broadband WDM Transmission," *Optical Fiber Communication Conference (OFC)*, p. Th1C.1, 2018. 108, 109

[14] J. Cai, Y. Sun, H. Zhang, H. G. Batshon, M. V. Mazurczyk, O. V. Sinkin, D. G. Foursa, and A. Pilipetskii, "49 . 3 Tb / s Transmission Over 9100 km Using C + L EDFA and 54 Tb / s Transmission Over 9150 km Using Hybrid-Raman EDFA," *Journal of Lightwave Technology*, vol. 33, no. 13, pp. 2724–2734, 2015. 10, 21

[15] A. Carena, G. Bosco, V. Curri, Y. Jiang, P. Poggiolini, and F. Forghieri, "EGN model of non-linear fiber propagation," *Optics Express*, vol. 22, no. 13, pp. 16 335–16 362, 2014. [Online]. Available: http://www.opticsexpress.org/abstract.cfm?URI=oe-22-13-16335 60, 61, 66, 67, 81

[16] A. Carena, G. Bosco, V. Curri, P. Poggiolini, M. Tapia Taiba, and F. Forghieri, "Statistical characterization of PM-QPSK signals after propagation in uncompensated fiber links," *European Conference on Optical Communication, ECOC*, vol. 1-2, no. 1, pp. 7–9, 2010. 62

[17] A. Carena, G. Bosco, V. Curri, P. Poggiolini, Y. Jiang, and F. Forghieri, "A Simple and Effective Closed-Form GN-Model Correction Formula Accounting for Signal Non-Gaussian Distribution," *Journal of Lightwave Technology*, vol. 33, no. 2, pp. 1–7, 2015. [Online]. Available: http://arxiv.org/abs/1402.3528 103

[18] A. V. Cartaxo, R. S. Luís, B. J. Puttnam, T. Hayashi, Y. Awaji, and N. Wada, "Dispersion Impact on the Crosstalk Amplitude Response of Homogeneous Multi-Core Fibers," *IEEE Photonics Technology Letters*, vol. 28, no. 17, pp. 1858–1861, 2016. 25

[19] S. Chandrasekhar, B. Li, J. Cho, X. Chen, E. C. Burrows, G. Raybon, and P. J. Winzer, "High-spectral-efficiency transmission of PDM 256-QAM with Parallel

Probabilistic Shaping at Record Rate-Reach Trade-offs," *European Conference on Optical Communications (ECOC)*, p. Th.3.C.1, 2016. 22, 23

[20] J. Cho, X. Chen, S. Chandrasekhar, G. Raybon, R. Dar, L. Schmalen, E. Burrows, and A. Adamiecki, "Trans-Atlantic Field Trial Using Probabilistically Shaped 64-QAM at High Spectral Efficiencies and Single-Carrier Real-Time 250-Gb / s 16-QAM," *Optical Fiber Communication Conference*, vol. 1, pp. 20–22, 2017. 22, 24, 26, 61

[21] A. Comms, "Market wired press report on aqua comms ltd now live cable," http://www.marketwired.com/press-release/aqua-comms-america-europe-connect-goes-live-2088094.htm, accessed: 2016-08-29. 23

[22] C. B. Czegledi, G. Liga, D. Lavery, M. Karlsson, E. Agrell, S. J. Savory, and P. Bayvel, "Digital backpropagation accounting for polarization-mode dispersion," *Optics Express*, vol. 25, no. 3, p. 1903, 2017. [Online]. Available: https://www.osapublishing.org/abstract.cfm?URI=oe-25-3-1903 133

[23] R. Dar, S. Chandrasekhar, A. H. Gnauck, B. Li, J. Cho, E. C. Burrows, P. J. Winzer, and B. Laboratories, "Impact of WDM Channel Correlations on Nonlinear Transmission," *European Conference and Exhibition on Optical Communication*, pp. 482–484, 2016. 72, 109

[24] R. Dar, M. Feder, A. Mecozzi, and M. Shtaif, "Properties of nonlinear noise in long, dispersion-uncompensated fiber links," *Opt. Express*, vol. 21, no. 22, pp. 25 685–25 699, 2013. 62, 83, 89

[25] ——, "Accumulation of nonlinear interference noise in fiber-optic systems," *Opt. Express*, vol. 22, no. 12, pp. 14 199–14 211, 2014. 60, 82

[26] ——, "Inter-channel nonlinear interference noise in WDM systems: modeling and mitigation," *Journal of Lightwave Technology*, vol. 33, no. 5, pp. 1044–1053, 2015. 83, 89

[27] ——, "Pulse collision picture of inter-channel nonlinear interference in fiber-optic communications," *Journal of Lightwave Technology*, vol. 34, no. 2, pp. 593–607, 2016. 87

[28] D. J. Elson, L. Galdino, R. Maher, R. I. Killey, B. C. Thomsen, and P. Bayvel, "High spectral density transmission emulation using amplified spontaneous emission noise," *Optics Letters*, vol. 41, no. 1, p. 68, January 2016. [Online]. Available: https://www.osapublishing.org/abstract.cfm?URI=ol-41-1-68 24, 28, 30, 61, 76

[29] D. J. Elson, G. Saavedra, K. Shi, D. Semrau, L. Galdino, R. Killey, B. C. Thomsen, and P. Bayvel, "Investigation of bandwidth loading in optical fibre transmission using amplified spontaneous emission noise," *Opt. Express*, vol. 25, no. 16, pp. 19 529–19 537, 2017. 24, 28, 29, 69

[30] D. J. Elson, B. J. Puttnam, G. Rademacher, R. S. Luis, E. Sillekens, L. Galdino, and D. Lavery, "Impact of Intercore Crosstalk on Achievable Information Rates," *IEEE Photonics Summer Topical*, pp. 2–3, 2018. 28, 29

[31] ——, "Nonlinearity Mitigation in the Presence of Intercore-Crosstalk," *European conference on optical communications (ECOC)*, pp. 2–3, 2018. 28, 29

[32] R.-J. Essiambre, G. Kramer, P. J. Winzer, G. J. Foschini, and B. Goebel, "Capacity limits of optical fiber networks," *Journal of Lightwave Technology*, vol. 28, no. 4, pp. 662–701, 2010. 18

[33] I. Fatadin, S. J. Savory, and D. Ives, "Compensation of quadrature imbalance in an optical coherent OQPSK receiver in presence of frequency offset," *IEEE Photonics Technology Letters*, vol. 20, no. 20, pp. 1733–1735, 2008. 136

[34] FCC, "2014 u.s. international circuit capacity data," https://www.fcc.gov/reports-research/reports/international-circuit-capacity-reports/international-circuit-capacity/, accessed: 2018-08-22. 4

[35] T. Fehenberger, M. Mazur, T. A. Eriksson, M. Karlsson, and N. Hanik, "Experimental analysis of correlations in the nonlinear phase noise in optical fiber systems," in *ECOC 2016; 42nd European Conference on Optical Communication; Proceedings of*. VDE, 2016, pp. 1–3. 82

[36] C. R. S. Fludger, T. Duthel, D. van den Borne, C. Schulien, E.-D. Schmidt, T. Wuth, J. Geyer, E. De Man, K. Giok-Djan, and H. de Waardt, "Coherent equalization and POLMUX-RZ-DQPSK for robust 100-GE transmission," *IEEE/OSA Journal of Lightwave Technology*, vol. 26, no. 1, pp. 64–72, Jan. 2008. 136

[37] L. Galdino, G. Liga, G. Saavedra, D. Ives, R. Maher, A. Alvarado, S. Savory, and R. Killey, "Experimental Demonstration of Modulation-Dependent Nonlinear Interference in Optical Fibre Communication," *ECOC 2016*, no. 1, pp. 2–4, 2016. 67, 72, 103

[38] L. Galdino, G. Saavedra, D. Semrau, D. J. Elson, M. Tan, A. Iqbal, P. Harper, R. I. Killey, and P. Bayvel, "Digital Back-Propagation Performance in Wideband Optical Fibre Transmission Systems," *European Conference on Optical Communication, ECOC*, no. 1, pp. 2–4, 2017. 30, 61, 96, 100, 101, 102, 103, 109

[39] L. Galdino, D. Semrau, D. Lavery, G. Saavedra, C. B. Czegledi, E. Agrell, R. I. Killey, and P. Bayvel, "On the limits of digital back-propagation in the presence of transceiver noise," *Optics Express*, vol. 25, no. 4, p. 4564, 2017. [Online]. Available: https://www.osapublishing.org/abstract.cfm?URI=oe-25-4-4564 54, 67

[40] L. Galdino, L. Domanic, Z. Liu, K. Balakier, E. Sillekens, D. Elson, G. Saavedra, R. Killey, and P. Bayvel, "The Trade-Off between Tranceiver Capacity and Symbol Rate," *Optical Fiber Communication Conference (OFC)*, vol. W1B.4, pp. 1–42, 2018. 29

[41] L. Galdino, A. Edwards, M. Ionescu, J. James, W. Pelouch, E. Sillekens, D. Semrau, D. Lavery, R. I. Killey, S. Barnes, P. Bayvel, and S. Desbruslais, "120 Tbit/s Transmission over Single Mode Fibre using Continuous 91 nm

Hybrid Raman-EDFA Amplification," *Arxiv*, vol. arXiv:1804, pp. 5–7, 2018. [Online]. Available: http://arxiv.org/abs/1804.01845 28

[42] O. Geller, R. Dar, M. Feder, and M. Shtaif, "A shaping algorithm for mitigating inter-channel nonlinear phase-noise in nonlinear fiber systems," *Journal of Lightwave Technology*, vol. 34, no. 16, pp. 3884–3889, 2016. 18

[43] C. R. Giles and E. Desurvire, "Modeling erbium-doped fiber amplifiers," *IEEE/OSA Journal of Lightwave Technology*, vol. 9, no. 2, pp. 271 –283, Feb. 1991. 39

[44] D. Godard, "Self-recovering equalization and carrier tracking in two-dimensional data communication systems." *IEEE Trans. Commun.*, no. 28, pp. 1867–1875, 1980. 134

[45] O. Golani, R. Dar, M. Feder, A. Mecozzi, and M. Shtaif, "Modeling the bit-error-rate performance of nonlinear fiber-optic systems," *Journal of Lightwave Technology*, vol. 34, no. 15, pp. 3482–3489, 2016. 82, 83, 87

[46] O. Golani, M. Feder, A. Mecozzi, and M. Shtaif, "Correlations and phase noise in NLIN- modelling and system implications," in *Optical Fiber Communication Conference*. Optical Society of America, 2016, p. W3I.2. 82

[47] O. Golani, D. Elson, D. Lavery, L. Galdino, R. I. Killey, P. Bayvel, and M. Shtaif, "Experimental characterization of the time correlation properties of nonlinear interference noise," *European Conference on Optical Communication, ECOC*, no. 1, pp. 1–3, 2017. 28, 30

[48] O. Golani, M. Feder, and M. Shtaif, "Kalman-MLSE equalization of nonlinear noise," in *Optical Fiber Communication Conference*. Optical Society of America, 2017, pp. W2A–46. 19, 82, 105, 108

[49] O. Golani, D. J. Elson, D. Lavery, L. Galdino, R. Killey, P. Bayvel, and M. Shtaif, "Experimental characterization of nonlinear interference noise as a process of inter-symbol interference," *Optics Letters*, pp. 1–5, 2018. 28, 29

[50] C. Hager, A. G. i Amat, A. Alvarado, and E. Agrell, "Design of apsk constellations for coherent optical channels with nonlinear phase noise," *IEEE Transactions on Communications*, vol. 61, no. 8, pp. 3362–3373, August 2013. 23

[51] R. Hartley, "Transmission of information," *Bell System Technical Journal*, July 1928. 32

[52] T. Hayashi, T. Taru, O. Shimakawa, T. Sasaki, and E. Sasaoka, "Characterization of crosstalk in ultra-low-crosstalk multi-core fiber," *Journal of Lightwave Technology*, vol. 30, no. 4, pp. 583–589, 2012. 25

[53] ——, "Uncoupled multi-core fiber enhancing signal-to-noise ratio." *Optics express*, vol. 20, no. 26, pp. B94–103, 2012. [Online]. Available: http://www.ncbi.nlm.nih.gov/pubmed/23262918 25, 96

[54] E. Ip, "Nonlinear compensation using backpropagation for polarization-multiplexed transmission," *IEEE/OSA Journal of Lightwave Technology*, vol. 27, no. 6, pp. 939–951, Mar. 2010. 133

[55] E. Ip and J. M. Kahn, "Compensation of dispersion and nonlinear impairments using digital backpropagation," *Journal of Lightwave Technology*, vol. 26, no. 20, pp. 3416–3425, 2008. 18

[56] K. Kao and G. Hockham, "Dielectric-fibre surface waveguides for optical frequencies," *Proceedings of the Institution of Electrical Engineers*, vol. 113, no. 7, p. 1151, 1966. [Online]. Available: http://digital-library.theiet.org/content/journals/10.1049/piee.1966.0189 16

[57] L. G. Kazovsky, L. Curtis, W. C. Young, and N. K. Cheung, "All-fiber 90° optical hybrid for coherent communications," *Applied Optics*, vol. 26, no. 3, pp. 437–439, Feb 1987. [Online]. Available: http://ao.osa.org/abstract.cfm?URI=ao-26-3-437 41

[58] D. P. Keck, F. P. Kapron, and R. D. Maurer, "Radiation Losses in Glass Optical Waveguides," *Applied Physics Letters*, vol. 17, no. 423, 1970. 16

[59] G. Khanna, B. Spinnler, S. Calabr, and E. D. Man, "A Memory Polynomial Based Digital Pre-Distorter for High Power Transmitter Components," *Optical Fiber Communication Conference*, vol. M2C.4, no. 2, pp. 5–7, 2017. 45, 68

[60] R. Killey, P. Watts, M. Glick, and P. Bayvel, "Electronic precompensation techniques to combat dispersion and nonlinearities in optical transmission," *European Conference on Optical Communications*, vol. 6, 2005. 37

[61] T. Kobayashi and A. Sano, "120-Gb/s PDM 64-QAM transmission over 1,280 km using multi-staged nonlinear compensation in digital coherent receiver," *Fiber Optics Communications*, pp. 5–7, 2011. [Online]. Available: http://www.opticsinfobase.org/abstract.cfm?uri=OFC-2011-OThF6 10, 21

[62] T. Koike-akino, C. Cao, Y. Wang, S. C. Draper, D. S. Millar, K. Parsons, K. Kojima, M. Pajovic, L. Galdino, D. J. Elson, D. Lavery, and P. Bayvel, "Irregular Polar Coding for Multi-Level Modulation in Complexity-Constrained Lightwave Systems," *European Conference on Optical Communication, ECOC*, pp. 4–6, 2017. 28, 30

[63] T. Koike-Akino, C. Cao, Y. Wang, S. C. Draper, D. S. Millar, K. Kojima, K. Parsons, L. Galdino, D. J. Elson, D. Lavery, and P. Bayvel, "Irregular polar coding for complexity-constrained lightwave systems," *Journal of Lightwave Technology*, vol. 36, no. 11, pp. 2248–2258, 2018. 28, 29, 80

[64] Y. Koizumi, K. Toyoda, M. Yoshida, and M. Nakazawa, "1024 QAM (60 Gbit/s) single-carrier coherent optical transmission over 150 km." *Optics express*, vol. 20, no. 11, pp. 12 508–14, may 2012. [Online]. Available: http://www.ncbi.nlm.nih.gov/pubmed/22714238 17

[65] M. J. Korenberg and I. W. Hunter, "The identification of nonlinear biological systems: Volterra kernel approaches," *Annals of Biomedical Engineering*, vol. 24, no. 2, pp. 250–268, 1996. 47

[66] D. Lavery, D. Ives, G. Liga, A. Alvarado, S. J. Savory, and P. Bayvel, "The benefit of split nonlinearity compensation for single channel optical fiber communications," *IEEE Photonics Technology Letters*, vol. 28, no. 17, pp. 1803–1806, 2016. 26, 45

[67] G. Lazzarin, S. Pupolin, and A. Sarti, "Nonlinearity Compensation in Digital Rasio Systems," *IEEE Transactions on Communications*, vol. 42, no. 2-4, 2, pp. 988–999, Feb-Apr 1994. 45

[68] Level-3, "Level 3 investor press release, telegeography," http://investors.level3.com/investor-relations/press-releases/press-release-details/2000/Level-3-Activates-New-Undersea-Cable-Connecting-North-American-and-European-Broadband-Networks/default.aspx, accessed: 2016-08-21. 22

[69] G. Liga, T. Xu, A. Alvarado, R. I. Killey, and P. Bayvel, "On the performance of multichannel digital backpropagation in high-capacity long-haul optical transmission," *Optics Express*, vol. 22, no. 24, pp. 30 053–30 062, 2014. [Online]. Available: http://www.opticsinfobase.org/abstract.cfm?URI=oe-22-24-30053 131

[70] Z. Liu, L. Galdino, J. R. Hayes, D. Lavery, B. Karanov, D. J. Elson, K. Shi, B. C. Thomsen, M. N. Petrovich, D. J. Richardson, F. Poletti, R. Slavík, and P. Bayvel, "Record High Capacity (6 . 8 Tbit / s) WDM Coherent Transmission in Hollow-Core Antiresonant Fiber," *Optical Fiber Communication Conference (OFC)*, pp. 28–30, 2017. 30

[71] R. S. Luis, B. J. Puttnam, A. V. Cartaxo, W. Klaus, J. M. Mendinueta, Y. Awaji, N. Wada, T. Nakanishi, T. Hayashi, and T. Sasaki, "Time and Modulation Frequency Dependence of Crosstalk in Homogeneous Multi-Core Fibers," *Journal of Lightwave Technology*, vol. 34, no. 2, pp. 441–447, 2016. 25, 95

[72] A. Macho, M. Morant, and R. Llorente, "Unified Model of Linear and Nonlinear Crosstalk in Multi-Core Fiber," *Journal of Lightwave Technology*, vol. 34, no. 13, pp. 3035–3046, 2016. 95

[73] ——, "Experimental evaluation of nonlinear crosstalk in multi-core fiber," *Optics Express*, vol. 23, no. 14, p. 18712, 2015. [Online]. Available: https://www.osapublishing.org/abstract.cfm?URI=oe-23-14-18712 26, 95

[74] R. Maher, M. Sato, T. Xu, L. Galdino, S. Kilmurray, S. Savory, B. Thomsen, R. I. Killey, and P. Bayvel, "Digital Pulse Shaping to Mitigate Linear Crosstalk in Nyquist-Spaced 16QAM WDM Transmission Systems," *Opto-Electronics and Communications Conference (Oecc)*, pp. 76–78, 2014. 45

[75] R. Maher, T. Xu, L. Galdino, M. Sato, A. Alvarado, K. Shi, S. J. Savory, B. C. Thomsen, R. I. Killey, and P. Bayvel, "Spectrally Shaped DP-16QAM Super-Channel Transmission with Multi-Channel Digital Back-Propagation." *Scientific reports*, vol. 5, p. 8214, 2015. [Online]. Available: http://www.nature.com/srep/2015/150203/srep08214/full/srep08214.html 26, 43, 61, 93, 131, 133

[76] R. Maher, L. Galdino, D. J. Elson, D. Lavery, A. Alvarado, and P. Bayvel, "Algorithms and Reach Enhancement for Ultra High Bandwidth Transceivers," *Optical Fiber Communication Conference*, vol. 2, p. Th3A.1, 2016. [Online]. Available: https://www.osapublishing.org/abstract.cfm?URI=OFC-2016-Th3A.1 30, 36, 42, 61, 74, 75, 93

[77] S. Makovejs, C. C. Roberts, F. Palacios, H. B. Matthews, D. a. Lewis, T. Dana, P. G. Diehl, J. J. Johnson, J. D. Patterson, C. R. Towery, and S. Y. Ten, "Record-Low (0.1460 dB/km) Attenuation Ultra-Large Aeff Optical Fiber for Submarine Applications," *Optical Fiber Communication Conference (OFC) Postdeadline papers*, p. Th5A.2, 2015. 16

[78] D. Marcuse, C. R. Menyuk, and P. K. Wai, "Application of the Manakov-PMD equation to studies of signal propagation in optical fibers with randomly varying birefringence," *Journal of Lightwave Technology*, vol. 15, no. 9, pp. 1735–1745, 1997. 133

[79] M. Mazurczyk, D. G. Foursa, H. G. Batshon, H. Zhang, J.-x. Cai, O. Sinkin, A. Pilipetskii, G. Mohs, Bergano, and N. S, "44.1 Tb / s Transmission over 9,100 km Using Coded Modulation Based on 16QAM Signals at 4.9 bits/s/Hz Spectral Efficiency," *European Conference and Exhibition on Optical Communication (ECOC) Postdeadline Papers*, vol. Th.3.C.2, 2012. 17

[80] M. E. Mccarthy, N. M. Suibhne, S. T. Le, P. Harper, and A. D. Ellis, "High Spectral Efficiency Transmission Emulation for Non-Linear Transmission Performance Estimation for High Order Modulation Formats," in *ECOC Proceedings*, 2014, p. P .5.7. 61

[81] R. J. Mears, L. Reekie, I. M. Jauncey, and D. N. Payne, "Low-noise erbium-doped fibre amplifier operating at 1.54?m," *Electronics Letters*, vol. 23, no. 19, pp. 1026–1028, September 1987. 17

[82] A. Mecozzi and R. J. Essiambre, "Nonlinear shannon limit in pseudolinear coherent systems," *Journal of Lightwave Technology*, vol. 30, no. 12, pp. 2011–2024, 2012. 61, 103

[83] A. Mecozzi and R.-J. Essiambre, "Nonlinear shannon limit in pseudolinear coherent systems," *Journal of Lightwave Technology*, vol. 30, no. 12, pp. 2011–2024, 2012. 18

[84] Microsoft, "Microsoft, facebook and telxius complete the highest-capacity subsea cable to cross the atlantic," https://news.microsoft.com/features/microsoft-facebook-telxius-complete-highest-capacity-subsea-cable-cross-atlantic/, accessed: 2018-07-31. 16

[85] D. S. Millar, R. Maher, A. Alvarado, M. Paskov, K. Kojima, and K. Parsons, "Transceiver-Limited High Spectral Efficiency Nyquist-WDM Systems," in *Optical Fiber Communication Conference (OFC)*, 2015, pp. 10–12. 74, 75, 77, 78

[86] D. S. Millar, L. Galdino, R. Maher, M. Pajovic, T. Koike-akino, G. Saavedra, D. J. Elson, K. Shi, M. S. Erkılınç, E. Sillekens, R. I. Killey, B. C. Thomsen, K. Kojima, K. Parsons, and P. Bayvel, "A Simplified Dual-Carrier DP-64QAM 1 Tb / s Transceiver," *Optical Fiber Communication Conference*, pp. 39–41, 2017. 28, 30, 61, 80

[87] T. Miya, Y. Terunuma, T. Hosaka, and T. Miyashita, "Ultimate low-loss single-mode fibre at 1.55 μm," *Electronics Letters*, vol. 15, no. 4, pp. 106–108, 1979. 16

[88] M. Nakazawa, S. Okamoto, T. Omiya, K. Kasai, and M. Yoshida, "256 QAM (64 Gbit/s) Coherent Optical Transmission over 160 km with an Optical Bandwidth of 5.4 GHz," *Optical Fiber Communication Conference (OFC)*, p. OMJ5, 2010. [Online]. Available: http://www.opticsinfobase.org/abstract.cfm?URI=OFC-2010-OMJ5 17

[89] A. Nespola, M. Huchard, G. Bosco, A. Carena, Y. Jiang, P. Poggiolini, and F. Forghieri, "Experimental validation of the EGN-model in uncompensated optical links," in *Optical Fiber Communication Conference*. Optical Society of America, 2015, pp. Th4D–2. 62

[90] R. D. Nowak, "Penalized Least Squares Estimation of Volterra Filters and Higher order Statistics," *IEEE Transactions on Signal Processing*, vol. 46, no. 2, pp. 419–428, 1998. 47

[91] S. L. I. Olsson, J. Cho, S. Chandrasekhar, X. Chen, E. Burrows, and P. J. Winzer, "Record-High 17.3-bit/s/Hz Spectral Efficiency Transmission over 50 km Using Probabilistically Shaped PDM 4096-QAM," *Optical Fiber Communication Conference*, p. Th4c.5, 2018. 17, 22, 23

[92] T. Omiya, M. Yoshida, and M. Nakazawa, "400 Gbit/s 256 QAM-OFDM transmission over 720 km with a 14 bit/s/Hz spectral efficiency by using high-resolution FDE." *Optics express*, vol. 21, no. 3, pp. 2632–41, Feb 2013. [Online]. Available: http://www.ncbi.nlm.nih.gov/pubmed/23481719 10, 21, 22, 23

[93] M. Pajovic and et al., "Multi-pilot aided carrier phase estimation for single carrier coherent systems," in *Signal Processing in Photonic Communications (SPPCom)*, 2015, p. SpT4D.4. 77

[94] P. Poggiolini and Y. Jiang, "Recent advances in the modeling of the impact of nonlinear fiber propagation effects on uncompensated coherent transmission systems," *Journal of Lightwave Technology*, vol. 35, no. 3, pp. 458–480, 2017. 82, 83, 84

[95] P. Poggiolini, "The GN model of non-linear propagation in uncompensated coherent optical systems," *Journal of Lightwave Technology*, vol. 30, no. 24, pp. 3857–3879, 2012. 61, 66, 73

[96] P. Poggiolini, A. Carena, V. Curri, G. Bosco, and F. Forghieri, "Analytical modeling of nonlinear propagation in uncompensated optical transmission links," *Photonics Technology Letters*, vol. 23, no. 11, pp. 742–744, 2011. 81

[97] P. Poggiolini, G. Bosco, A. Carena, V. Curri, Y. Jiang, and F. Forghieri, "The GN-model of fiber non-linear propagation and its applications," *Journal of Lightwave Technology*, vol. 32, no. 4, pp. 694–721, 2014. 81

[98] J. E. Prilepsky, S. A. Derevyanko, and S. K. Turitsyn, "Nonlinear spectral management: Linearization of the lossless fiber channel," *Opt. Express*, vol. 21, no. 20, pp. 24 344–24 367, 2013. 18

[99] J. G. Proakis and M. Salehi, *Digital Communications*, 5th ed. McGraw-Hill, 2008. 44

[100] B. J. Puttnam, R. S. Luís, W. Klaus, J. Sakaguchi, J. D. Mendinueta, Y. Awaji, N. Wada, Y. Tamura, T. Hayashi, M. Hirano, and J. Marciante, "2.15 Pb / s Transmission Using a 22 Core Homogeneous Single- Mode Multi-Core Fiber and Wideband Optical Comb," *European Conference on Optical Communication, ECOC*, no. 1, p. PDP 3.1, 2015. 19, 26

[101] B. J. Puttnam, G. Rademacher, R. S. Luís, W. Klaus, Y. Awaji, and N. Wada, "Inter-core crosstalk spectrum and penalty measurements in 7-core fiber," in *European Conference on Optical Communication*, 2017, pp. 1–3. 95

[102] B. J. Puttnam, R. S. Luís, W. Klaus, J. M. Mendinueta, Y. Awaji, N. Wada, and T. A. Eriksson, "Impact of inter-core crosstalk on the transmission distance of QAM formats in multi-core fibers," *IEEE Photonics Journal*, vol. 8, no. 2, 2016. 10, 25, 26, 98, 101

[103] G. Rademacher, R. S. Luís, B. J. Puttnam, Y. Awaji, and N. Wada, "Crosstalk dynamics in multi-core fibers," *Optics Express*, vol. 25, no. 10, p. 12020, 2017. [Online]. Available: https://www.osapublishing.org/abstract.cfm?URI=oe-25-10-12020 25, 95, 109, 110

[104] D. Rafique, M. Mussolin, M. Forzati, J. Mårtensson, M. N. Chugtai, and A. D. Ellis, "Compensation of intra-channel nonlinear fibre impairments using simplified digital back-propagation algorithm," *Opt. Express*, vol. 19, no. 10, pp. 9453–9460, 2011. 100

[105] G. Raybon, J. Cho, A. Adamiecki, P. Winzer, A. Konczykowska, F. Jorge, J.-y. Dupuy, M. Riet, B. Duval, K. Kim, S. Randel, D. Pilori, B. Guan, N. Fontaine, E. C. Burrows, and C. Hill, "Single Carrier High Symbol Rate Transmitter for Data Rates up to 1 . 0 Tb / s," *Optical Fiber Communication Conference*, pp. 4–6, 2016. 74, 75

[106] J. Renaudier, A. C. Meseguer, A. Ghazisaeidi, P. Tran, R. R. Muller, and R. Brenot, "First 100-nm Continuous-Band WDM Transmission System with 115Tb / s Transport over 100km Using Novel Ultra-Wideband Semiconductor Optical Amplifiers," *European Conference on Optical Communication*, no. 1, pp. 2–4, 2017. 80

[107] D. J. Richardson, J. M. Fini, and L. E. Nelson, "Space-division multiplexing in optical fibres," *Nature Photonics*, vol. 7, no. 5, pp. 354–362, 2013. [Online]. Available: http://dx.doi.org/10.1038/nphoton.2013.94 19, 95

[108] T. Richter, C. Schmidt-Langhorst, S. Watanabe, J. K. Fischer, and C. Schubert, "Distributed 1-Tb/s all-optical aggregation capacity in 125-GHz optical bandwidth by frequency conversion in fiber," in *European Conference and Exhibition on Optical Communication*, 2015, p. PDP2.5. 74, 75

[109] T. Richter, J. Pan, and S. Tibuleac, "Comparison of WDM Bandwidth Loading Using Individual Transponders, Shaped, and Flat ASE Noise," *Optical Fiber Communication Conference*, p. W1B.2, 2018. 108

[110] D. Rife and R. Boorstyn, "Single tone parameter estimation from discrete-time observations," *IEEE Transactions on information theory*, vol. 20, no. 5, pp. 591–598, 1974. 135

[111] R. Rios-Müller, J. Renaudier, P. Brindel, H. Mardoyan, P. Jennevé, L. Schmalen, and G. Charlet, "1-Terabit/s Net Data-Rate Transceiver Based on Single-Carrier Nyquist-Shaped 124 GBaud PDM-32QAM," *Optical Fiber Communication Conference Post Deadline Papers*, no. 1, p. Th5B.1, 2015. [Online]. Available: https://www.osapublishing.org/abstract.cfm?uri=OFC-2015-Th5B.1 74, 75

[112] M. Rocks, A. Ehrhardt, A. Gladisch, N. Hanik, and G. Lehr, "WDM application in the network of Deutsche Telekom AG," *Integrated Optoelectronic Devices*, no. January, 1999. 110

[113] G. Saavedra, M. Tan, D. J. Elson, L. Galdino, D. Semrau, A. Iqbal, I. D. Phillips, P. Harper, N. M. Suibhne, A. D. Ellis, D. Lavery, B. C. Thomsen, R. I. Killey, and P. Bayvel, "Experimental Investigation of Nonlinear Signal Distortions in Ultra-Wideband Transmission Systems," *Optical Fiber Communication Conference (OFC)*, no. 1, pp. 8–10, 2017. 28, 30

[114] G. Saavedra, D. Semrau, M. Tan, A. Iqbal, D. J. Elson, L. Galdino, P. Harper, R. I. Killey, and P. Bayvel, "Inter-channel Stimulated Raman Scattering and its Impact in Wideband Transmission Systems," *Optical Fiber Communication Conference (OFC)*, vol. Th1C.3, pp. 10–12, 2018. 29, 59

[115] G. Saavedra, M. Tan, D. J. Elson, L. Galdino, D. Semrau, A. Iqbal, I. D. Phillips, P. Harper, A. Ellis, B. C. Thomsen, R. I. Killey, and P. Bayvel, "Experimental Analysis of Nonlinear Impairments in Fibre Optic Transmission Systems up to 7 . 3 THz," *Journal of Lightwave Technology*, vol. 35, no. 21, pp. 4809–4816, 2017. 11, 28, 29, 59, 60, 61, 73, 80, 108

[116] I. Sackey, F. D. Ros, J. K. Fischer, T. Richter, M. Jazayerifar, C. Peucheret, K. Petermann, and C. Schubert, "Kerr Nonlinearity Mitigation: Mid-Link Spectral Inversion Versus Digital Backpropagation in 5 x 28-GBaud PDM 16-QAM Signal Transmission," *Journal of Lightwave Technology*, vol. 33, no. 9, pp. 1821–1827, 2015. 26

[117] B. E. A. Saleh and M. C. Teich, "Fundamentals of Photonics," in *Fundamentals of Photonics*, vol. Second Edition, 2007. 38

[118] M. Salsi, C. Koebele, P. Tran, H. Mardoyan, E. Dutisseuil, J. Renaudier, M. Bigot-Astruc, L. Provost, S. Richard, P. Sillard, S. Bigo, and G. Charlet, "Transmission of 96×100Gb/s with 23% super-FEC overhead over 11,680 km,

using optical spectral engineering," *2011 Optical Fiber Communication Conference and Exposition and the National Fiber Optic Engineers Conference*, p. OMR2, 2011. 10, 21

[119] A. Sano, T. Kobayashi, A. Matsuura, S. Yamamoto, S. Yamanaka, E. Yoshida, Y. Miyamoto, M. Matsui, M. Mizoguchi, and T. Mizuno, "100 $\times$ 120-Gb/s PDM 64-QAM transmission over 160 km using linewidth-tolerant pilotless digital coherent detection," *European Conference and Exhibition on Optical Communication*, no. 1, pp. 1–3, sep 2010. [Online]. Available: http://ieeexplore.ieee.org/lpdocs/epic03/wrapper.htm?arnumber=5621382 17

[120] A. Sano, H. Takara, T. Kobayashi, and Y. Miyamoto, "Crosstalk-managed high capacity long haul multicore fiber transmission with propagation-direction interleaving," *Journal of Lightwave Technology*, vol. 32, no. 16, pp. 2771–2779, 2014. 25

[121] G. M. Saridis, D. Alexandropoulos, G. Zervas, and D. Simeonidou, "Survey and evaluation of space division multiplexing: From technologies to optical networks," *IEEE Communications Surveys and Tutorials*, vol. 17, no. 4, pp. 2136–2156, 2015. 19

[122] Y. Sasaki, K. Takenaga, K. Aikawa, Y. Miyamoto, and T. Morioka, "Single-Mode 37-Core Fiber with a Cladding Diameter of 248 μ m," *Optical Fiber Communication Conference (OFC)*, p. Th1H.2, 2017. 26

[123] S. J. Savory, "Digital coherent optical receivers: Algorithms and subsystems," *IEEE Journal of Selected Topics in Quantum Electronics*, vol. 16, no. 5, pp. 1164–1179, Sep. 2010. 136

[124] ——, "Digital filters for coherent optical receivers," *OSA Optics Express*, vol. 16, no. 2, pp. 804–817, Jan. 2008. 17, 37, 132, 136

[125] C. Schmidt-Langhorst, R. Elschner, F. Frey, R. Emmerich, and C. Schubert, "Experimental analysis of nonlinear interference noise in heterogeneous flex-grid WDM transmission," in *European Conference on Optical Communication (ECOC), 2015*. IEEE, 2015, pp. 1–3. 18, 82

[126] M. Secondini and E. Forestieri, "Analytical fiber-optic channel model in the presence of cross-phase modulation," *Photonics Technology Letters*, vol. 24, no. 22, pp. 2016–2019, 2012. 82

[127] ——, "On XPM mitigation in WDM fiber-optic systems," *Photonics Technology Letters*, vol. 26, no. 22, pp. 2252–2255, 2014. 82

[128] D. Semrau, D. Lavery, L. Galdino, R. I. Killey, and P. Bayvel, "The Impact of Transceiver Noise on Digital Nonlinearity Compensation," *Journal of Lightwave Technology*, vol. 36, no. 3, pp. 695–702, 2018. 40, 96

[129] P. Serena and A. Bononi, "On the Accuracy of the Gaussian Nonlinear Model for Dispersion-unmanaged Coherent Links," *European Conference on Optical Communication*, p. Th.1.D.3, 2013. 67, 103

[130] C. E. Shannon, "Communication in the presence of noise," *Proceedings of the IRE*, vol. 37, no. 1, pp. 10–21, Jan 1949. 18, 32

[131] E. Sillekens, D. Semrau, G. Liga, N. A. Shevchenko, Z. Li, A. Alvarado, P. Bayvel, R. I. Killey, and D. Lavery, "A simple nonlinearity-tailored probabilistic shaping distribution for square qam," in *Optical Fiber Communication Conference*. Optical Society of America, 2018, p. M3C.4. [Online]. Available: http://www.osapublishing.org/abstract.cfm?URI=OFC-2018-M3C.4 23

[132] D. Soma, Y. Wakayama, S. Beppu, S. Sumita, T. Tsuritani, T. Hayashi, T. Nagashima, M. Suzuki, H. Takahashi, K. Igarashi, I. Morita, and M. Suzuki, "10.16 Peta-bit/s Dense SDM/WDM transmission over Low-DMD 6-Mode 19-Core Fibre across C+L Band," *European Conference on Optical Communication (ECOC)*, no. 1, p. Th.PDP.A.1, 2017. 26, 95, 134

[133] D. M. Spirit, M. J. O'Mahony, and B. Telecom., *High capacity optical transmission explained / edited by D.M. Spirit, M.J. O'Mahony*. J. Wiley Chichester ; New York, 1995. 39

[134] R. Stolen and J. Bjorkholm, "Parametric amplification and frequency conversion in optical fibers," *IEEE Journal of Quantum Electronics*, vol. 18, no. 7, pp. 1062–1072, July 1982. 81

[135] R. Stolen and A. Ashkin, "Optical kerr effect in glass waveguide," *Applied Physics Letters*, vol. 22, no. 6, pp. 294–296, 1973. [Online]. Available: https://doi.org/10.1063/1.165464 18

[136] S. Takasaka, K. Maeda, K. Kawasaki, K. Yoshioka, and R. Sugizaki, "Cladding Pump Recycling in 7-core EDFA," in *European Conference on Optical Communication (ECOC)*, vol. We1e.4, 2018. 19

[137] K. Takenaga, Y. Arakawa, S. Tanigawa, N. Guan, S. Matsuo, K. Saitoh, and M. Koshiba, "Reduction of crosstalk by trench-assisted multi-core fiber," *Optical Fiber Communication Conference (OFC)*, p. OWJ4, 2011. [Online]. Available: http://www.opticsinfobase.org/abstract.cfm?uri=OFC-2011-OWJ4 25, 95

[138] Y. Tamura, H. Sakuma, K. Morita, M. Suzuki, Y. Yamamoto, K. Shimada, Y. Honma, K. Sohma, T. Fujii, and T. Hasegawa, "The First 0.14-dB/km Loss Optical Fiber and its Impact on Submarine Transmission," *Journal of Lightwave Technology*, vol. 36, no. 1, pp. 44–49, 2018. 16

[139] TeleGeography, "Submarine cable map, telegeography," http://www.submarinecablemap.com/#/submarine-cable/yellow, accessed: 2016-06-21. 22

[140] ——, "From land to sea to cloud," https://www2.telegeography.com/global-bandwidth-forecast-service, accessed 2018-04-24. 16

[141] M. Terayama, S. Okamoto, K. Kasai, M. Yoshida, and M. Nakazawa, "4096 QAM (72 Gbit / s) Single-Carrier Coherent Optical Transmission with a Potential SE of 15.8 bit / s / Hz in All-Raman Amplified 160 km Fiber Link," *Optical Fiber Communication Conference (OFC)*, pp. 8–10, 2018. 22, 23

[142] J. R. Treichler, C. Johnson, and L. M. G., "Theory and Design of Adaptive Filters." *Prentice Hall.*, 2001. 135

[143] P. J. Winzer and R.-J. Essiambre, "Advanced optical modulation formats," *Proceedings of the IEEE*, vol. 94, no. 5, pp. 952–985, 2006. 17

[144] P. J. Winzer, D. T. Neilson, and A. R. Chraplyvy, "Fiber-optic transmission and networking: the previous 20 and the next 20 years [Invited]," *Optics Express*, vol. 26, no. 18, p. 24190, 2018. [Online]. Available: https://www.osapublishing.org/abstract.cfm?URI=oe-26-18-24190 17, 94

[145] F. Yaman, S. Zhang, Y.-k. Huang, Y. Zhang, M.-f. Huang, I. B. Djordjevic, E. Mateo, Y. Inada, T. Inoue, and T. Ogata, "30 . 6-Tb / s Full-Duplex Bidirectional Transoceanic Transmission over 75 $\times$ 90.9-km Fiber Spans," *Optical Fiber Communication Conference*, p. Th5B.5, 2014. 10, 21

[146] M. Yankov, F. Da Ros, E. P. Da Silva, T. Fehenberger, L. Barletta, D. Zibar, L. Oxenlöwe, M. Galili, and S. Forchhammer, "Nonlinear phase noise compensation in experimental WDM systems with 256QAM," *Journal of Lightwave Technology*, vol. 35, no. 8, pp. 1438 – 1443, 2017. 82

[147] M. P. Yankovn, F. D. Ros, P. Edson, S. Forchhammer, K. J. Larsen, L. K. Oxenløwe, M. Galili, and D. Zibar, "Constellation Shaping for WDM Systems Using 256QAM / 1024QAM With Probabilistic Optimization," *Journal of Lightwave Technology*, vol. 34, no. 22, pp. 5146–5156, 2016. 22, 24

[148] H. Zhang, H. Batshon, C. Davidson, D. Foursa, and A. Pilipetskii, "Multi-Dimensional Coded Modulation in Long-Haul Fiber Optic Transmission," *Journal of Lightwave Technology*, vol. 8724, no. c, pp. 1–1, 2015. [Online]. Available: http://ieeexplore.ieee.org/lpdocs/epic03/wrapper.htm?arnumber=7079387 61, 80

[149] S. Zhang, F. Yaman, Y.-k. Huang, J. D. Downie, D. Zou, W. A. Wood, R. Khrapko, S. Mishra, V. Nazarov, J. Hurley, I. B. Djordjevic, E. Mateo, and Y. Inada, "Capacity-Approaching Transmission over 6375 km at Spectral Efficiency of 8.3 bit/s/Hz," in *Optical Fiber Communication Conference*, vol. Th5C.2, 2016. 10, 21, 22

[150] X. Zhou, L. Nelson, and P. Magill, "High spectral efficiency 400 Gb/s transmission using PDM time-domain hybrid 32–64 QAM and training-assisted carrier recovery," *Journal of Lightwave Technology*, vol. 31, no. 7, pp. 999–1005, 2013. [Online]. Available: http://www.opticsinfobase.org/abstract.cfm?uri=jlt-31-7-999 10, 21

[151] D. Zibar, M. Piels, R. Jones, and C. G. Schäffer, "Machine learning techniques in optical communication," *Journal of Lightwave Technology*, vol. 34, no. 6, pp. 1442–1452, 2016. 82

A

Acronyms

AC	Alternating current
ACF	Auto-correlation function
ADC	Analogue to digital converter
AIR	Achievable information rate
ASE	Amplified spontaneous emission
AOM	Acousto-optical modulator
AWG	Arbitrary waveform generator
AWGN	Additive white Gaussian noise
BTB	Back-to-back
BCH	Bose-Chaudhuri-Hocquenghem
BER	Bit error rate
CD	Chromatic dispersion
CMA	Constant modulus algorithm
CMOS	Complementary metal oxide semiconductor

CPE Carrier phase estimation

CUT Channel under test

CW Continuous wave

DA Driver amplifier

DAC Digital to analogue converter

DBP Digital backpropagation

DC Direct current

DCF Dispersion compensating fibre

DPSK Differential phase shift keying

DSP Digital signal processing

DWDM Dense wavelength division multiplexing

ECOC European conference on optical communication

ECL External cavity laser

EDC Electronic dispersion compensation

EDFA Erbium doped fibre amplifier

EGN Enhanced Gaussian noise

FEC Forward error correction

FIR Finite impulse response

FOM Figure of merit

FPGA Field programmable gate array

FWM Four wave mixing

GN Gaussian noise

GSOP Gram-Schmidt orthogonalisation procedure

HD-FEC Hard decision-forward error correction

IC Interfering channel

IC-XT Intercore-crosstalk

IEEE Institute of Electrical and Electronics Engineers

IQ Inphase and quadrature

ISI Inter-symbol interference

LAN Local area network

LEAF Large effective area fibre

LDPC Low density parity check

LLR Log-likelihood ratio

LMS Least mean squares

LSE Least square error

LO Local oscillator

MCF Multicore fibre

MCI Multi channel interference

MERL Mitsubishi electric research laboratory

MI Mutual information

MIMO Multiple input-multiple output

MZM Mach-Zehnder modulator

NLI Nonlinear interference

NICT National Institute of Information and Communications Technology

NLSE Nonlinear Schrödinger equation

OFC Optical fiber communications conference

OFDM Orthogonal frequency division multiplexing

OOK On-off keying

OSA Optical spectrum analyser

OSNR Optical signal to noise ratio

PAM Pulse amplitude modulation

PAR Peak to average ratio

PBS Polarisation beam splitter

PDF Probability density function

PMD Polarisation mode dispersion

PRBS Pseudo-random binary sequence

PPRN Phase and polarisation rotation noise

PS Polarisation scrambler

PSD Power spectral density

QAM Quadrature amplitude modulation

QPSK Quadrature phase shift keying

QSM Quasi-single mode

RDE Radially directed equaliser

RF Radio frequency

RIN Relative intensity noise

RRC Root raised cosine

SCI Self channel interference

SDM Spatial division multiplexing

SD-FEC Soft decision-forward error correction

SMF Single-mode fibre

SNR Signal to noise ratio

SPM Self phase modulation

SS-ASE Spectrally shaped-amplified spontaneous emission

TIA Trans-impedance amplifier

VOA Variable optical attenuator

WDM Wavelength division multiplexed

WSS Wavelength selective switch

XCI Cross channel interference

XT Crosstalk

XPM Cross-phase modulation

B

Digital Signal Processing

It is noted there is no novelty about the DSP used in this thesis, but it is included here for completeness. Once the incoming optical signal has been detected and digitised by a phase and polarisation-diverse coherent receiver the signal can be processed. Using specific DSP algorithms the limitations imposed by experimental generation and transmission can be mitigated. The Fig. B.1 shows the chain of DSP used in the production of this thesis. The following sections describe each block in the order in which they are utilised in the chain.

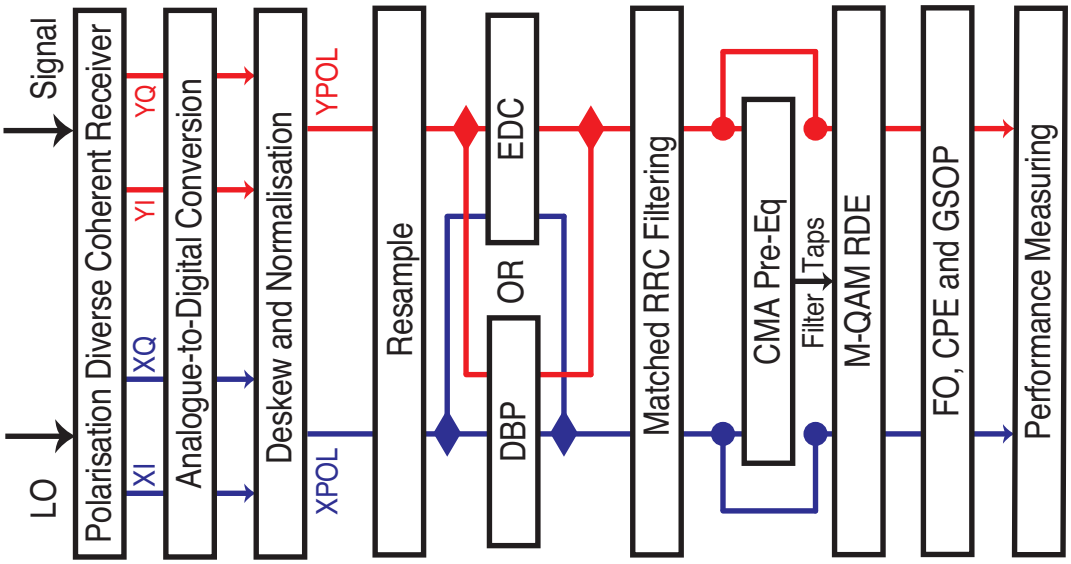

Figure B.1: Coherent receiver and subsequent DSP chain

B.1 Deskew and normalisation

Deskew and normalisation are separate imperfections and are dealt with independently by two blocks.

Deskew is performed on the data stream coming straight from the receiver. This compensates for any delay that might occur between each component of the signal. The four streams are the In-phase and Quadrature (I and Q) of the two polarisations (X and Y); XI, XQ, YI and YQ. One stream is chosen as the reference stream and the remaining streams have delays applied such that the samples all correspond to the same point in time. The delay between X and Y is important in DBP as the polarisations need to be aligned before starting the algorithm, as the samples should be an accurate representation of the electrical field. It is not as critical when only using electronic dispersion compensation (EDC) because the equaliser can compensate for this skew. The delay compensation that is applied, is of the order of 0.1 ps (smaller than the period of a symbol). The origin of the skew can be due to the optical path length, electrical path length, changes in temperature and/or the synchronisation jitter of the oscilloscopes' streams

Normalisation removes any direct current (DC) offset by subtracting the mean of each data stream and then normalises to unit power. GSOP is also applied at this stage. Please see Appendix B.8 for details of the algorithm. Applying this DSP block at this stage removes the non orthogonality of the 90° optical hybrid used in the coherent receiver, which is described in section 2.3.

B.2 Resampling

According to the Nyquist sampling theorem, when using EDC only 2 samples per symbol is required so the sampling rate of the incoming stream can be adjusted accordingly. Sampling rates higher than 2 samples per symbol for EDC are still possible but at the cost of increased computational complexity.

When using DBP instead of EDC, the sampling rate sets the amount of back propagated bandwidth. Discussion of the effect of varying back propagated bandwidth is discussed in detail in [69, 75]. The overall trend is, the closer the back propagated bandwidth is to that transmitted, the greater the amount of nonlinear interference mitigation, for sufficiently small polarisation mode dispersion (PMD) (<0.1 ps/$\sqrt{\text{km}}$).

B.3 Electronic dispersion compensation (EDC)

Chromatic dispersion is the effect of frequency dependent group velocity of the electric field whilst propagating along the optical fibre. This effect is constant and therefore can

be compensated by using one linear non adaptive filter [124]. A FIR is implemented as a convolution in the time domain, but in this work this is performed in the frequency domain as an overlap-add method. The application of a finite impulse response (FIR) can compensate any amount of dispersion if set up appropriately.

By separating out the linear and nonlinear effects of the channel the linear impairment can be removed. The linear part being chromatic dispersion and the nonlinear being the phase shift from the optical Kerr effect. The two effects are described in the nonlinear Schrödinger equation (NLSE) (Eq. 2.12). By setting α and γ to zero, chromatic dispersion only can be described, giving:

$$\frac{\partial A}{\partial z} = i\beta\frac{\partial^2 A}{\partial t^2} = i\frac{D\lambda^2}{4\pi c}\frac{\partial^2 A}{\partial t^2}. \tag{B.1}$$

This equation is linear and, hence, can be solved in the frequency domain. After Fourier transform A, becomes a function of frequency denoted G,

$$\frac{\partial G(z,\omega)}{\partial z} = -i\beta\omega^2 G(z,\omega) \tag{B.2}$$

where $G(z,\omega) = \exp(-i\beta\omega^2 z)$. Taking the inverse of this transfer function $1/G(z,\omega)$ will compensate the channel's static linear response, and Fourier transforming back into the time domain the impulse response $g(z,t)$ can be calculated.

$$g(z,t) = \sqrt{\frac{icT^2}{D\lambda^2 z}}\exp\left(-j\frac{\pi c}{D\lambda^2 z}t^2\right) \tag{B.3}$$

This is infinite in duration and non-causal but can be truncated in order to be implemented; the tap weights are given by [124],

$$a_k = \sqrt{\frac{icT^2}{D\lambda^2 z}}\exp\left(-i\frac{\pi cT^2}{D\lambda^2 z}k^2\right) - \left\lfloor\frac{N}{2}\right\rfloor < k < \left\lfloor\frac{N}{2}\right\rfloor \text{ and } N = 2\left\lfloor\frac{|D|\lambda^2 z}{2cT^2}\right\rfloor + 1 \tag{B.4}$$

where $T = \pi/\omega$ is the sampling period and $\lfloor\cdot\rfloor$ means to round towards minus infinity. N is an upper bound on the required number of taps. Dispersion compensation in practise is implemented in the frequency domain using the overlap and add method.

B.4 Digital backpropagation (DBP)

DBP is used to compensate for the nonlinearity of the optical fibre at the receiver. In chapter 2.12, it was shown that the NLSE can be used to model the optical channel. This method applies a random phase polarisation rotation at each step to emulate the change in polarisation from transmission. Digital backpropagation runs the equation

that describes the channel backwards after receiving the channel. To run the NLSE backwards each random phase rotation needs to be known. Since it is impossible to know the individual polarisation rotations, the propagation can be simplified by averaging all the random phase rotations [78]. The result of this operation is known as the Manakov equation and in this work DBP uses the coupled Manakov equation in reverse by inverting all of the propagation parameters [54]. This algorithm requires accurate knowledge of the fibre parameters and signal launch power [75]. The equations being solved are:

$$\frac{\partial A_x}{\partial z} = \frac{\alpha A_x}{2} + \frac{i\beta_2}{2}\frac{\partial^2 A_x}{\partial t^2} - i\gamma\frac{8}{9}(|A_x|^2 + |A_y|^2)A_x, \tag{B.5}$$

$$\frac{\partial A_y}{\partial z} = \frac{\alpha A_y}{2} + \frac{i\beta_2}{2}\frac{\partial^2 A_y}{\partial t^2} - i\gamma\frac{8}{9}(|A_x|^2 + |A_y|^2)A_y. \tag{B.6}$$

These are solved in its inverse form, by changing the sign of all the propagation parameters as follows,

$$\alpha \to -\alpha, \beta_2 \to -\beta_2, \gamma \to -\gamma. \tag{B.7}$$

As with solving the NLSE forwards for system modelling, these equations can be solved by using the split-step Fourier method. The number of steps taken per span has an impact on the effectiveness of this technique. Too few and it fails to compensate the linear section leading to worse performance than just using EDC [75]. Too many does not result in a reduction the signal to noise ratio (SNR) gain but does take longer to run.

The back propagated bandwidth is another factor in determining the effectiveness of DBP as the nonlinear interaction effectively broadens a signal. As long as the entire signal is captured the self phase modulation (SPM) can be undone. If the back propagating bandwidth is larger than the CUT, the frequencies of adjacent channels are captured and hence XPM can also be mitigated. If all of the transmitted signal is captured and back propagated it is termed full field DBP. In order for this technique to work the power profile and dispersion need to be known very accurately. In [75] where 70 GHz of bandwidth is back propagated, a change in dispersion (D) of ± 0.05 ps/(nm·km) leads to change of Q^2-factor of 0.5 dB.

As DBP attempts to undo the entire propagation, there is no need for chromatic dispersion compensation. As the signal propagates with stochastic noise from amplifiers along the channel the interaction between ASE and signal stops DBP from being a perfect compensation. The noise mixes with the signal after every span creating a noise term that cannot be mitigated. Another limit is PMD, this comes from using coupled Manakov equations, as these equations makes the assumption that all polarisation rotations even out over the course of transmission. The complete PMD profile needs to be known for it to be fully compensated [22].

B.5 Constant modulus algorithm (CMA) and radially directed equaliser (RDE)

An adaptive equaliser tries to estimate the Jones matrix of the channel and apply the inverse of it to the signal. Additionally, it emulates a matched filter and therefore compensates for linear distortions incurred by imperfect filtering, leading to an optimisation of the receiver sensitivity. An adaptive equaliser is also capable of compensating for residual chromatic dispersion and time dependent distortion of the signal. The equaliser attempts to invert the response of the channel such that a corrected signal can be extracted at the end. This removes some of the effects of channel imperfection, polarisation rotations and imperfect sampling incidence. The equaliser works by evaluating an error function whilst trying to restore something known about the original signal. Equalisers used in the work are presented in this thesis and are as follows: constant modulus algorithm (CMA) or Godard [44] algorithm and the RDE. To adapt the taps to the changing channel conditions, different update-algorithms are necessary depending on the properties of the modulation format. Radially directed equaliser is only needed when the modulation format has multiple amplitude levels. This algorithm uses pre converged taps from the CMA in order to reduce the number of passes required to produce a stable output.

Multiple-input-multiple-output (MIMO) systems are used in optical communications to combat multipath propagation effects such as PMD [132]. This structure, which in the literature is sometimes termed a butterfly structure, is implemented in this work and consists of four FIR filters ($\mathbf{h_{xx}}, \mathbf{h_{xy}}, \mathbf{h_{yx}}$ and $\mathbf{h_{yy}}$). The FIR filters are implemented in the time domain, where N is the number of filter taps and k the output sample.

$$X_{out} = \mathbf{h_{xx}}^T \mathbf{X_{in}} + \mathbf{h_{xy}}^T \mathbf{Y_{in}} = \sum_{n=0}^{N-1} h_{xx}(n) X_{in}(k-n) + h_{xy}(n) Y_{in}(k-n), \tag{B.8}$$

The tap updates, with learning parameter μ are given as follows,

$$\begin{aligned}
\mathbf{h_{xx}} &\leftarrow \mathbf{h_{xx}} + \mu E_x X_{out}(k) \mathbf{X_{in}}^* \\
\mathbf{h_{xy}} &\leftarrow \mathbf{h_{xy}} + \mu E_x X_{out}(k) \mathbf{Y_{in}}^* \\
\mathbf{h_{yx}} &\leftarrow \mathbf{h_{yx}} + \mu E_y Y_{out}(k) \mathbf{X_{in}}^* \\
\mathbf{h_{yy}} &\leftarrow \mathbf{h_{yy}} + \mu E_y Y_{out}(k) \mathbf{Y_{in}}^*
\end{aligned} \tag{B.9}$$

where the E_x and E_y are the error functions for the x and y polarisations. For the CMA

these are,

$$E_x(k) = 1 - |X_{out}(k)|^2 \tag{B.10}$$

$$E_y(k) = 1 - |Y_{out}(k)|^2, \tag{B.11}$$

where $E_x(k)$, $E_y(k)$ is the error in x and y polarisations for a sample k and $X_{out}(k)$ $Y_{out}(k)$ are the signal samples. This algorithm uses the known fact about the data, that the transmitted signal should have constant power, hence each symbol should lie upon a constant modulus.

Higher order modulation formats such as QAM have multiple levels so the power is no longer constant. This means that the CMA is insufficient, but it can be used for pre convergence [142] when equalising higher order QAM. A radially directed equaliser algorithm takes the information that there are multiple rings and fits the samples to those rings. This is done by updating the error functions to,

$$E_x(k) = X_{out}(k)(R_k - |X_{out}(k)|^2) \tag{B.12}$$

$$E_y(k) = Y_{out}(k)(R_k - |Y_{out}(k)|^2), \tag{B.13}$$

where R_k is the radius of the nearest constellation symbol for each output sample. The job of this equaliser is to minimise these error functions by updating taps of a filter in a decision directed manner with least mean squares (LMS) error.

B.6 Frequency offset removal

The LO laser is usually free running and in this thesis is always independent of the signal laser. Due to the independent lasers there can be a frequency offset (FO) and in this work the FO is compensated at the receiver using a Fourier method. The optical frequency of the transmit laser is kept within ± 0.2 GHz of the LO, this is termed intradyne detection. For FO removal, the received complex data is raised to the 4^{th} power then Fourier transformed into the frequency domain and the peak power is found. Raising to the fourth power completely removes the modulation format of a QPSK signal. For higher order M-QAM signals the symbols are mapped to points around the desired angle so can be considered noise. This method still achieves results with the higher noise from M-QAM [110].

The output of these operations correspond to the relative frequency of the local oscillator (LO) and transmit laser. Then by taking note of the sampling rate an appropriate FIR filter can be applied that changes the phase of all the samples such that they no longer have an offset. By doing this the offset is assumed to be constant over the waveform. Residual phase noise and offset is then dealt with by the following carrier phase estimation (CPE) block.

B.7 Carrier phase estimation

In experiments the phase noise coming from laser linewidth adds uncertainty to the carrier frequency; so when trying to decode symbols, mistakes can be made. The following carrier recovery or carrier phase estimation algorithm tracks this time varying phase component and attempt to remove it. Viterbi algorithm is a phase estimation technique for constant modulus formats. By raising the symbols to the M^{th} power the modulation is removed and then the phase can be estimated separately by taking the argument. Noise received M-PSK symbols in complex notation would take the form of

$$Z(k) = \exp\left(i\left[\frac{2\pi}{M}(m_k - 1) + \phi(k)\right]\right) + n(k), \tag{B.14}$$

where M is the number of possible phase values, m_k determines the symbol that was sent, $n(k)$ is an amplitude noise term and $\phi(k)$ a phase noise term varying per sample. It can be seen that by raising the symbols to the M^{th} power the resulting symbols, are a multiple of 2π. This operation removes the modulation so only the carrier phase is left. The phase of the carrier can then be estimated and tracked to know which symbol was sent [36, 123, 124].

The phase estimate for the kth symbol $\phi'(k)$ is estimated by adding its N predecessors and successors, to average the phase noise. Leading to an averaging window of size $2N+1$.

$$\phi'(k) = \frac{1}{M}\arg\left(\frac{1}{2N+1}\sum_{n=k-N}^{k+N}\mathbf{X}_{in}(n)^M\right). \tag{B.15}$$

Since this algorithm requires comparing the received symbols to expected symbols it is known as decision directed.

B.8 Gram-Schmidt orthogonalisation procedure

Gram-Schmidt orthogonalisation procedure (GSOP) is performed as described in [33]. This compensates for non orthogonality of the I and Q components of the signal. The origin of this non orthogonality can come from incorrect phase biasing of the transmitter Mach-Zehnder modulator (MZM) or the optical hybrid in the coherent receiver not being exactly 90° depending on where it is used.

Given two nonorthogonal components of the received signal, denoted by $r_I(k)$ and $r_Q(k)$, the GSOP results in a new pair of orthonormal signals, denoted by $I^o(k)$ and $Q^o(k)$, as

$$I^o(k) = \frac{r_I(k)}{\sqrt{P_I}} \tag{B.16}$$

$$Q'(k) = r_Q(k) - \frac{\rho r_I(k)}{P_I} \tag{B.17}$$

$$Q^o(k) = \frac{Q'(k)}{\sqrt{P_Q}}, \tag{B.18}$$

where $\rho = \mathbb{E}[r_I(k)r_Q(k)]$ is the correlation coefficient, $P_I = \mathbb{E}[r_I(k)]$, $P_Q = \mathbb{E}[Q'^2(k)]$ and $\mathbb{E}[\cdot]$ denotes the ensemble average operator.

B.9 Performance measurement

After the complete DSP chain has run decisions need to be made in order to recover the transmitted sequence. Performance measuring involved choosing which symbol was sent and then mapping each symbol back into bits. As the transmitted bit sequence is known the received sequence and transmitted sequence can be compared via an auto correlation. The point at which the sequences overlap the most is then chosen, then each sequence is aligned and a binary exclusive OR (XOR) operation is performed. The sum of the XOR vector is now calculated to give the bit error rate. In addition, after sequence alignment, the SNR can calculated on the symbol level. MI is calculated as described and discussed in section 2.1.2.

After sequence alignment the calculation of the other metrics used in this thesis (bit error rate (BER), Q^2-factor, mutual information (MI) and SNR) can be performed. By assuming a binary modulation format with Gaussian noise the Q^2-factor in decibels can be estimated from BER (x) using the following equation,

$$Q^2\text{-factor} = 20\log_{10}\left(\frac{1}{2}\text{erfc}\left(\frac{x}{\sqrt{2}}\right)\right), \tag{B.19}$$

where $\text{erfc}(\cdot)$ is the complementary error function defined as,

$$\text{erfc}(x) = 1 - \text{erf}(x) = 1 - \frac{2}{\sqrt{\pi}}\int_0^x e^{-t^2}dt. \tag{B.20}$$

where $\text{erf}(x)$ is the error function.

Q^2-factor is originally derived from the overlap of the probability density function (PDF)s corresponding to output noise distributions at binary one and zero levels. In order for a BER to be considered statistically significant at least 100 errors need to be counted.